A Mission Concept Study for the Solar and Space Physics Decadal Survey

Final Report

Submitted in response to:
NNH21ZDA001N-HMCS
Heliophysics Mission Concept Studies

PILOT

Plasma Imaging LOcal and Tomographic experiment

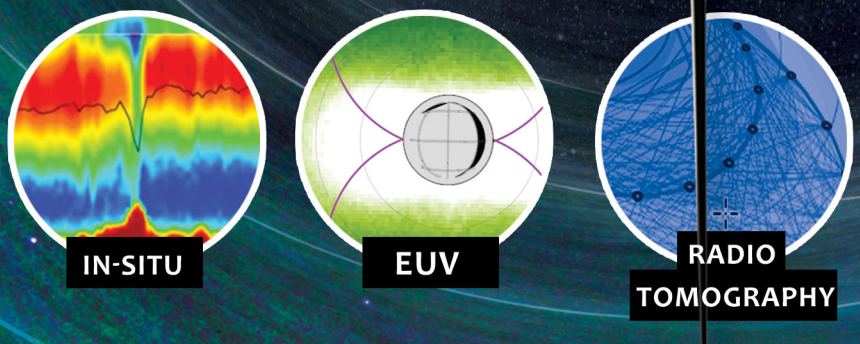

Principal Investigator

David Malaspina
David.Malaspina@lasp.colorado.edu
University of Colorado, LASP

Design Study Leads

Constance Spittler
Constance.Spittler@lasp.colorado.edu

Jason Link
Jason.Link@lasp.colorado.edu

Bryce Unruh
Bryce.Unruh@lasp.colorado.edu

University of Colorado, LASP

PILOT

Plasma Imaging LOcal and Tomographic experiment

Following the Mass to Understand the Flow of Cold Plasma in Earth's Inner Magnetosphere

The Plasma Imaging Local and Tomographic experiment (PILOT) mission provides the transformational multi-scale observations required to answer fundamental open questions about mass and energy flow dynamics in Earth's magnetosphere. PILOT uses a constellation of small spacecraft to capture cold plasma mass dynamics and its impact on magnetospheric systems over an unprecedented range of spatial and temporal scales.

PILOT Science Goal & Objectives

Science Goal	Science Objectives
Determine the primary pathways of mass and energy flow through the coupled systems of the terrestrial magnetosphere	Ob1: Identify and quantify the key processes that govern mass and energy exchange between the ionosphere and magnetosphere.
	Ob2: Discover the pathways and processes governing cold plasma mass transport through and out of the inner magnetosphere.
	Ob3: Determine how, where, and when cold plasma acts most efficiently to regulate coupling between magnetospheric regions and between plasma populations.

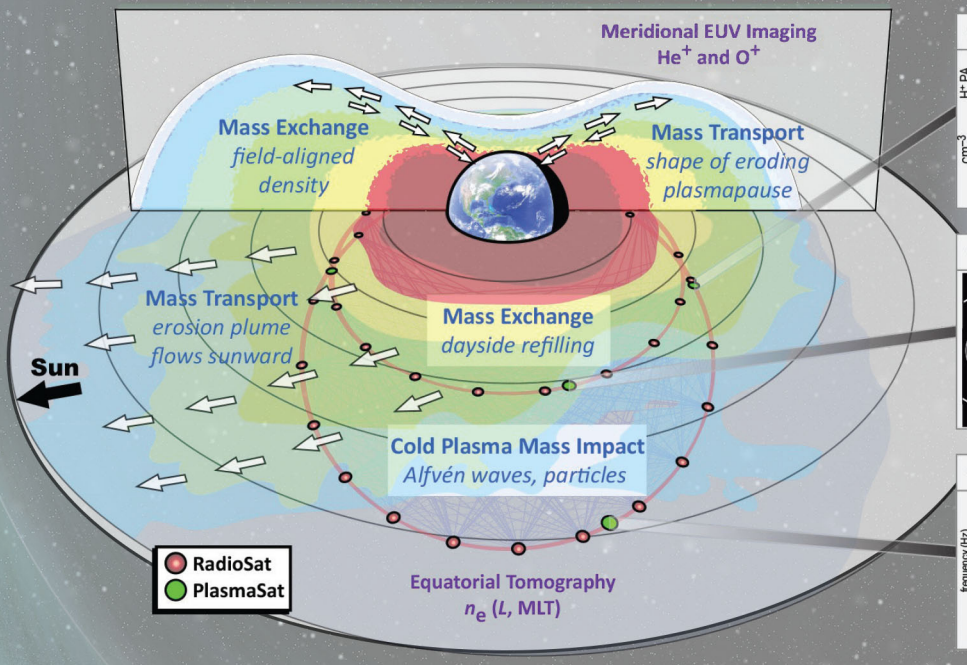

PILOT Science Objectives

Ob1 ***M-I mass and energy exchange***

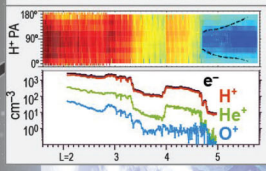

How plasmasphere is refilled or returned to the ionosphere
- global RT images
- meridional EUV
- in situ plasma, waves

Ob2 ***Cold Plasma Mass Transport***

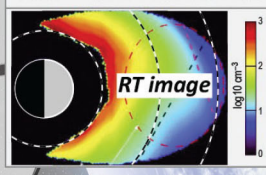

Pathways and mechanisms of cold plasma mass transport
- equatorial e– density
- meridional He+ vs O+
- in situ heating/cooling

Ob3 ***Cold Plasma Mass Impact***

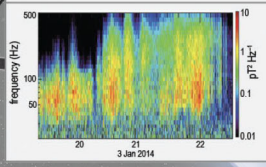

How cold plasma mass affects Alfvén waves, injections, & particles
- global RT images
- global mass weighting
- in situ plasma, waves

Science Payload

RadioSat (30)	
RT	Radio tomography/relaxation sounder
EED	Energetic electron detector
FGM	Fluxgate magnetometer
PlasmaSat PlasmaSat (2) / PlasmaSatEUV (2)	
EMF	Electric & magnetic fields, relaxation sounder
PIMS	Ion mass spectrometer
EPS	Energetic particle spectrometer
EUVCS	EUV He^+ & O^+/O^{++} imager (PlasmaSatEUV only)

Mission Concept Science Team

David Malaspina, PI (CU/LASP)

Robert Ergun (CU/LASP) | Jerry Goldstein (SwRI)
Laila Andersson (CU/LASP) | Joseph Borovsky (SSI)
Xiangning Chu (CU/LASP) | Dennis Gallagher (MSFC) | Vania Jordanova (LANL)
Naomi Maruyama (CU/LASP) | Solene Lejosne (UCB)
Scott Thaller (CU/LASP) | Brian Walsh (BU)

Mission Concept Design Team

Constance Spittler (CU/LASP) | Jason Link (CU/LASP) | Bryce Unruh (CU/LASP)
Diane Brening (CU/LASP) | Maxwell Fowle (CU/LASP) | Jerry Jason (CU/LASP)
Thomas Sparn (CU/LASP) | Jeff Parker (Advanced Space)
Lauren De Mondt (Advanced Space)

PILOT

Plasma Imaging LOcal and Tomographic experiment

Following the Mass to Understand the Flow of Cold Plasma in Earth's Inner Magnetosphere

Mission Parameter	RadioSat	PlasmaSat	PlasmaSatEUV
Duration	3 Year Prime Mission	3 Year Prime Mission	3 Year Prime Mission
Orbit	Inner: 1.52 R_E x 4.25 R_E Outer: 1.1 R_E x 6.25 R_E	1.52 R_E x 4.25 R_E	1.1 R_E x 6.25 R_E
# of S/C Elements	30	2	2
# of Science Instruments	3	3	4
Payload Mass (CBE)	15.5 kg	60.5 kg	91.1 kg
Spacecraft Dry Mass (MEV)	57.3 kg	228.1 kg	228.1 kg
Propellant Mass	5.8 kg	26.5 kg	26.5 kg
Spacecraft Wet Mass (MEV)	63.0 kg	254.6 kg	254.6 kg
Spacecraft Power (MEV)	187 W	290 W	290 W
Risk Class	D	C	C
Data Volume	583 Gb	5923 Gb	17637 Gb

Individual RadioSat (fully deployed)

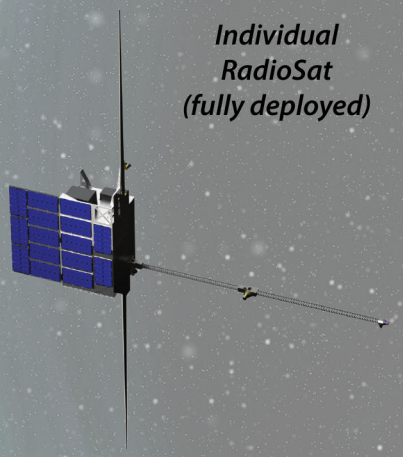

RadioSat Launch Packing

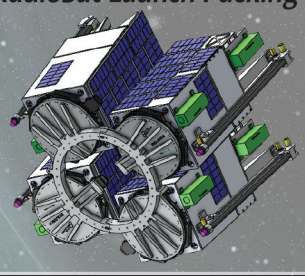

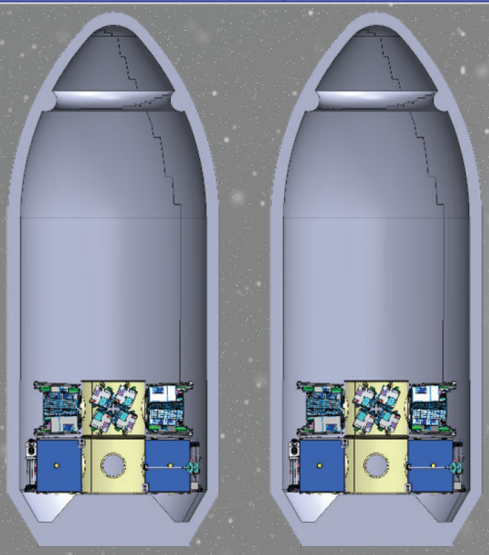

PILOT is launched on two Falcon Heavy LV with 14 RadioSats and 2 PlasmaSats to the inner orbit and 16 RadioSats and 2 PlasmaSatEUVs to the outer orbit.

Individual PlasmaSat (fully deployed)

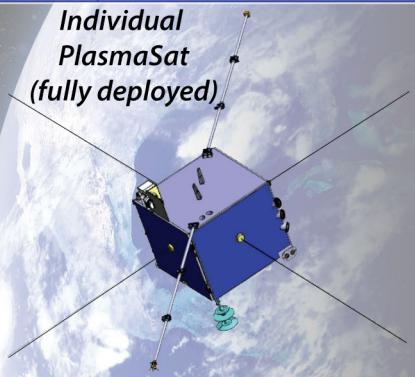

PILOT orbits

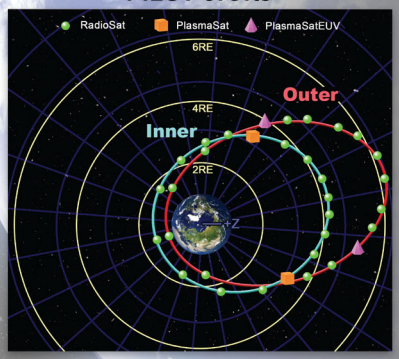

Schedule	Phase A		Phase B		Phase C			Phase D				Phase E	Phase F
Duration	18 Months		12 Months		30 Months			24 Months				36 Months	12 Months
Start	Oct-30		Apr-32		Apr-33			Oct-35				Oct-37	Oct-40
End	Apr-32		Apr-33		Oct-35			Oct-37				Oct-40	Oct-41
Activity	*SRR/MDR*	*KDP-B*	*MPDR*	*KDP-C*	*MCDR*	*SIR*	*KDP-D*	*ORR*	*LRR*	*Launch 1*	*Launch 2*	-	-
Date	Dec-31	Apr-32	Nov-32	Apr-33	July-34	Sep-35	Oct-35	Oct-36	Aug-37	Sep-37	Nov-37	-	-

Cost	Phase A	Phase B	Phase C	Phase D	Phase E	Phase F	Total
Total without Reserves	$10.21M	$25.78M	$438.69M	$874.28M	$99.65M	$2.13M	$1,450.74M
Reserves (30%)	$3.06M	$7.73M	$131.61M	$118.28M	$29.89M	$0.64M	$291.21M
Total with Reserves	$13.28M	$33.51M	$570.30M	$992.56M	$129.54M	$2.77M	$1,741.95M

Contents

1 Executive Summary **1**

2 Science Investigation **2**
2.1 Solar Terrestrial Probes (STP) Science Objectives . . . 2
2.2 PILOT Mission Concept Science Objectives . . . 3
2.2.1 Connection to STP and Heliophysics Objectives . . . 8
2.2.2 Impact of Decrease in Constellation Size . . . 9
2.3 PILOT Mission Concept Science Traceability . . . 9

3 Mission Concept Implementation **10**
3.1 Overview . . . 10
3.1.1 Mission organization . . . 13
3.2 Concept Maturity Level (CML) . . . 14
3.3 Technology Maturity . . . 15
3.4 Key Trades . . . 15

4 Technical Overview **16**
4.1 RadioSat . . . 16
4.1.1 Instrument Payload Description . . . 17
4.1.2 RadioSat Spacecraft . . . 17
4.2 PlasmaSat . . . 20
4.2.1 Instrument Payload Description . . . 20
4.2.2 PlasmaSat Spacecraft . . . 22
4.3 Instrument Production, Integration and Test . . . 23
4.4 Concept of Operations and Mission Design . . . 24
4.4.1 Baseline Concept of Operations and Mission Design . . . 24
4.4.2 RadioSat Concept of Operations . . . 24
4.4.3 PlasmaSat/PlasmaSatEUV Concept of Operations . . . 24
4.4.4 Mission Design . . . 25
4.5 Observatory Integration and Test (I&T) . . . 25
4.6 Ground-based Observatories . . . 26
4.7 Risk List . . . 27

5 Development Schedule and Schedule Constraints **28**
5.1 High-Level Mission Schedule . . . 28
5.2 Science, Technology Development Plans . . . 28
5.3 Development Schedule and Constraints . . . 28

6 Mission Life-Cycle Cost **29**
6.1 Costing Methodology and Basis of Estimate . . . 29

A Acronyms **32**

B Design Team Personnel **37**

C PILOT Instrumentation Detail **39**
C.1 RadioSat RT Instrument . . . 39
C.1.1 RadioSat RT RF . . . 39
C.1.2 RadioSat RT APPS . . . 42
C.2 RadioSat FGM Instrument . . . 43
C.3 RadioSat EED Instrument . . . 45
C.4 PlasmaSat EMF Instrument Suite . . . 47
C.5 PlasmaSat EPS Instrument . . . 50
C.6 PlasmaSat PIMS Instrument . . . 52
C.7 PlasmaSat EUVCS Instrument . . . 53
C.8 Instrument Integration and Test . . . 55

D Technologies and Techniques: Deconvolution **56**
D.1 Radio Tomography Deconvolution . . . 56
D.1.1 Measurement of TEC . . . 58
D.1.2 Radio Tomographic Image Reconstruction . . . 58
D.2 EUV Image Deconvolution: Inversion and Forward Model Algorithms . . . 59

E Technologies and Techniques: Data Accessibility, Constellation Data, and Model-Data Fusion **61**
E.1 Accessibility of Constellation Data . . . 61
E.2 Constellation Data Products . . . 61
E.3 Model-Data Fusion . . . 61
E.3.1 Empirical Models . . . 61
E.3.2 Super Resolution Imaging . . . 62
E.3.3 Stereo EUV Imaging . . . 63
E.3.4 Physics-Based (PB) Modeling . . . 63

F Science Question Detail **65**

G Mission Overview Detail **77**
G.1 Key Architecture and Mission Trades . . . 77
G.2 Mission Requirements . . . 79
G.3 Mission Design . . . 79
G.4 Flight System . . . 82
G.4.1 RadioSat . . . 82
G.4.2 PlasmaSat and PlasmaSatEUV . . . 87
G.5 Concept of Operations . . . 88
G.6 Technology Maturation Plan . . . 91
G.6.1 RT RF . . . 91
G.6.2 EUVCS . . . 92
G.6.3 SPB . . . 93

H References **95**

1 Executive Summary

Heliophysics has a massive problem: we have not yet determined the fundamental processes that govern plasma mass and energy flow through the terrestrial magnetosphere, nor the degree to which these flows regulate key magnetospheric subsystems. Cold plasma (< 1 eV to 100 eV) carries the overwhelming majority of this mass (hundreds of metric tons), and tracking its flow is the weakest link in our chain of understanding for magnetospheric physics. Magnetospheric mass dynamics determine the importance of a planetary magnetic field for atmospheric retention, and therefore habitability, of Earth-like planets.

The fundamental science goal of the PILOT (Plasma Imaging LOcal and Tomographic experiment) mission concept is to determine the primary pathways of mass and energy flow through the coupled systems of the terrestrial magnetosphere. PILOT's science objectives (Ob) are:

Ob1 Identify and quantify the key processes that govern mass and energy exchange between the ionosphere and the magnetosphere.

Ob2 Discover the pathways and processes governing cold plasma mass transport through and out of the inner magnetosphere.

Ob3 Determine how, where, and when cold plasma mass acts most efficiently to regulate coupling between magnetospheric regions and between plasma populations.

PILOT achieves these science objectives by creating movies of the magnetosphere: rapidly imaging plasma mass flow using radio tomography (equatorial plane, $3 < L < 6$ and ≥ 3 MLT-hrs) and EUV imaging (entire meridonal plane). These measurements are anchored by in-situ measurements of cold (0.1–100 eV) ions (H^+, He^+, O^+) and electromagnetic fields embedded in the imaged regions.

PILOT uses a constellation of 34 spacecraft. 30 identical "RadioSats", in two near-equatorial highly elliptical orbits, create a network of total electron content (TEC) measurements for tomographic imaging. They also measure in-situ magnetic field, total density, and energetic electron flux. Four "PlasmaSats" (2 inner, 2 outer) sample in-situ electromagnetic fields, ion and electron distributions, cold ion distribution functions and composition, and total density. Outer PlasmaSats carry EUV cameras to image He^+ and O^+ ions. Figure 2.1 shows the RadioSats (red), tomographic image plane (grey mesh), EUV image plane, and PlasmaSats (green), superimposed on a plasmasphere erosion event.

Key technologies that enable PILOT are small-satellite constellations, radio tomography, advanced EUV filters and coatings, and spacecraft potential control. PILOT employs robust risk mitigation strategies that lower risk ratings to acceptable levels. Key mitigations include: radiation tolerance, constellation architectural redundancy, and selection of experienced high-capacity manufacturers.

PILOT directly addresses all Solar Terrestrial Probe (STP) objectives and advances heliophysics, opening new paths of investigation while closing key knowledge gaps.

STP objective addressed and critical knowledge gaps closed by PILOT

STP$^{\#}$1: Fundamental processes governing mass/energy flow in planetary magnetospheres

STP$^{\#}$2: How planetary magnetic fields affect atmospheric mass loss at habitable planets

STP$^{\#}$3: Mass regulation of plasma dynamics that impact safety & productivity in space

2 Science Investigation

2.1 Solar Terrestrial Probes (STP) Science Objectives

Heliophysics has a massive problem: we have not determined the fundamental processes that govern plasma mass flow through a terrestrial magnetosphere, and its impacts on magnetospheric subsystems. Vast amounts of plasma mass exits the ionosphere, accumulates in inner magnetospheric reservoirs, is transported through the magnetosphere, and can be lost to the solar wind. Cold plasma ($<$ 1 eV to 100 eV) carries the overwhelming majority of this mass (hundreds of metric tons), and tracking its flow is the weakest link in our chain of understanding for magnetospheric physics.

This mass flow, and the energy flows that drive it, govern the rate at which the gases from our planet's atmosphere are lost to space [1], a crucial aspect of Earth's ability to support life. Currently, we know more about the physics of atmospheric mass loss at Mars and Venus than we do at Earth [2, 3], in part because the Earth's planetary magnetic field creates a complex 'system of systems' composed of interdependent plasma populations and overlapping spatial regions that perpetually exchange mass and energy. Earth is the only rocky body in our solar system with both a substantial atmosphere and a strong internal magnetic field, making it an ideal natural laboratory where we can 'follow the mass' to determine how a planet's magnetic field impacts its atmospheric evolution.

During its journey through geospace, the enormous mass carried by cold plasma dynamically and dramatically regulates numerous magnetospheric subsystems [4], including the radiation belts [5], magnetopause [6], plasma sheet, and ring current [7, 8, 9, 10, 11]. Plasma mass density governs a wide range of magnetospheric phenomena including reconnection, tail stability, wave-particle interactions, neutral exospheric dynamics, Alfvén wave propagation, and magnetosphere-ionosphere coupling.

The Plasma Imaging LOcal and Tomographic experiment (PILOT) mission directly addresses all three STP objectives and advances the broader field of heliophysics, opening new paths of investigation (see Table 2.1) while closing key knowledge gaps in geospace.

STP Objectives	**PILOT**
STP #1: "Understand the fundamental physical processes of the complex space environment throughout our solar system, … as well as a dynamic system of magnetic and electric fields."	PILOT 'follows the mass' through geospace, to close a critical knowledge gap about the fundamental physical processes that govern the flow of mass and energy in a planetary magnetic field.
STP #2: "Understand how … the habitability of planets are affected by solar variability and planetary magnetic fields."	PILOT discovers mechanisms that enable planetary magnetic fields to regulate atmospheric mass loss, a key part of habitability.
STP #3: "Develop the capability to predict the extreme and dynamic conditions in space in order to maximize the safety and productivity of human and robotic explorers."	PILOT determines how, when, and where plasma mass density profoundly regulates the magnetospheric subsystems that directly impact safety and productivity, including the radiation belts.
Broader Heliophysics	**PILOT**
Science 2020-2024, a Vision for Scientific Excellence: "Heliophysics incorporates studies of the interconnected elements into a single system … that evolves in response to solar, planetary, and interstellar conditions"	PILOT opens new paths of scientific investigation into magnetospheric system science by providing an essential missing piece to knowledge of the magnetospheric 'system of systems': plasma mass transport.
NASA SMD Science Plan 2014, Heliophysics Objective: "Understand the Sun and its interactions with Earth and the solar system, including space weather"	PILOT advances Heliophysics broadly by obtaining a long overdue, multi-scale view of plasma mass flow's critical contribution to how planetary space environments respond to dynamic space weather.

Table 2.1: *PILOT STP and Heliophysics Objective Coverage*

Magnetospheric mass dynamics remains a critical knowledge gap in large part because prior observations of cold plasma and its impact on magnetospheric subsystems are limited to either few-spacecraft in-situ measurements of total plasma density with limited cold plasma composition data [4] and no contextual mass spatial distribution information [9, 12, 13], or to single-view line-of-sight integrated measurements without in-situ measurements embedded in the imaged plasma [14]. New progress requires simultaneous contextual measurements of plasma mass spatial distribution and embedded in-situ data.

2.2 PILOT Mission Concept Science Objectives

The fundamental science goal of PILOT is to determine the primary pathways of mass and energy flow through the coupled systems of the terrestrial magnetosphere. PILOT accomplishes this by focusing on the largest (and least-measured [4]) carrier of magnetospheric mass, cold plasma, and how its regulation of mass and energy transport unites the disparate plasma populations of a planetary magnetosphere into a coherent whole.

PILOT's science goal motivates three specific science objectives. Each targets a critical aspect of mass and energy exchange among the plasma populations that make up the magnetospheric meta-system. The science objectives are arranged to 'follow the mass' as it (i) exits the ionosphere, (ii) enters, and is transported through and out of, the inner magnetosphere, and (iii) profoundly modifies magnetospheric systems and magnetospheric energy transport along its journey. Achieving each science objective requires addressing specific science questions (SQ), listed below.

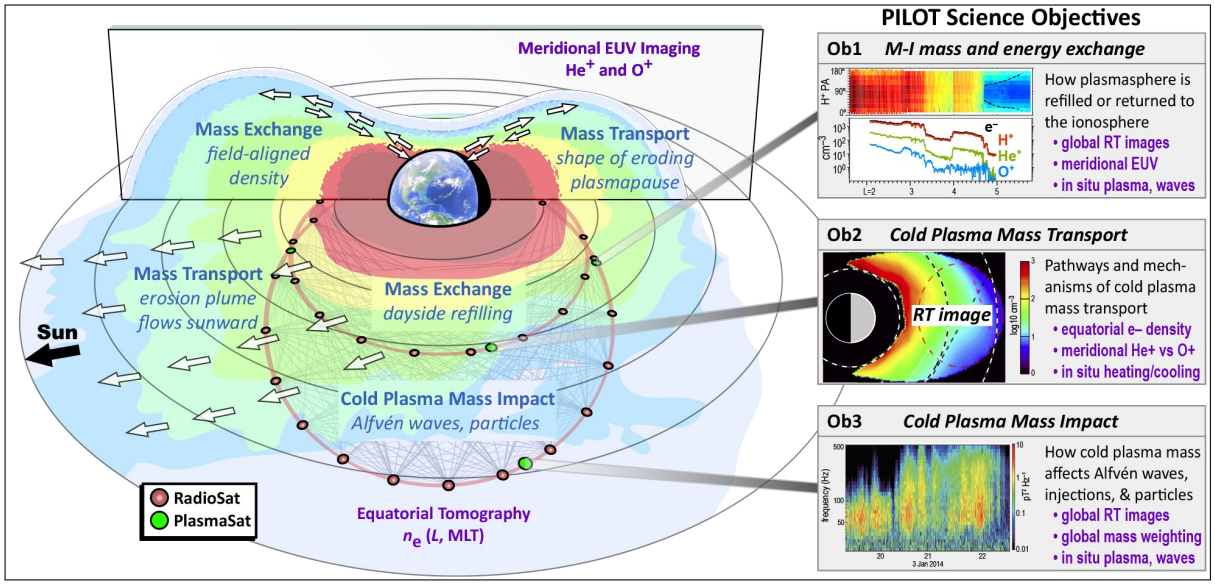

Figure 2.1: *PILOT achieves a long-overdue, cross-scale view of mass flow, via a combination of equatorial tomography, meridional EUV imaging, and in-situ measurements (Figure from [15]).*

PILOT Science Objective 1 (Ob1)

Identify and quantify the key processes that govern mass and energy exchange between the ionosphere and the magnetosphere.

[SQ 1a] How is the plasmasphere refilled from ionospheric sources?

The plasmasphere is the primary reservoir of plasma mass in the magnetosphere. It is refilled by ionized atmospheric gases transported from the ionosphere, and it drains to the outer magnetosphere (dayside and nightside) and solar wind during geomagnetic storms. Behind this basic picture lie major knowledge gaps: the physical processes that enable and regulate plasmaspheric refilling remain unknown.

What processes control the magnetic trapping of outflowing ionospheric mass [16, 17, 18, 19, 20, 21]? What processes cause refilling mass flow to vary by orders of magnitude [22, 23, 24, 25, 26, 27, 28, 29]? Why do refilling rates vary with radial distance from Earth [29]? What is the ion-mass dependence of refilling physics [30]? How does O^+ form a spatially distinct torus of material in the inner magnetosphere [31, 32, 33, 34, 35]?

PILOT achieves closure on this SQ by comparing multi-scale measurements of cold plasma mass flow and variability over a broad swath of the inner magnetosphere against theories for ion trapping [20], refilling variability [29], refilling mass dependence [30], and O^+ torus formation [34].

Closing this SQ requires direct and simultaneous measurements of (i) plasma density images over a broad swath of the near-equatorial inner magnetosphere ($\geq$ 3 hrs Magnetic Local Time (MLT)), (ii) meridional imaging of outflowing ionospheric He^+ ions (He^+ is a reliable proxy for H^+ [36, 37]), and (iii) in-situ observations, embedded within the imaged regions, of cold (0.1 eV to 100 eV) proton and heavy ion distribution functions—and of plasma waves that may isotropize outflowing ions. Observations for this SQ must cover radial distances where refilling is most active (3 <L-shell< 6), in the minutes, hours, and days that follow geomagnetically active times.

[SQ 1b] By what processes, and to what extent, does plasmaspheric mass return to the ionosphere or neutral exosphere?

A full accounting of mass flow between the ionosphere and plasmasphere must include return flow from the plasmasphere back into the ionosphere or neutral exosphere. There is a large knowledge gap related to this mass flow pathway. In the absence of sunlight, low-altitude recombination reduces ion pressure gradients, which is expected to cause downward transport [29, 38], potentially allowing nightside flux tubes to return plasmaspheric mass to the ionosphere. This mechanism may explain the anomalous mass loss reported on L-shells far from the eroded plasmapause boundary [29]. However, the cross-scale measurements required to test this hypothesis, or to identify a new one, currently do not exist. The extent to which charge exchange with the exosphere impacts magnetospheric cold plasma populations is also unknown.

This science question can be addressed by comparing existing predictions for downward ion transport of plasmaspheric mass [29] with direct multi-scale measurements of cold

plasma mass content and its variability over a broad swath of the inner magnetosphere, particularly on L-shells earthward of the eroded plasmapause boundary.

Closing this SQ requires simultaneous measurements of (i) plasma density images over a broad MLT-swath of the near-equatorial inner magnetosphere ($\geq$ 3 hrs MLT), (ii) meridional imaging of ionospheric plasma inflows (of O^+ and He^+, where He^+ acts as a proxy for H^+ [36, 37]), and (iii) in-situ observations of cold (0.1 eV to 100 eV) light and heavy ion distribution functions embedded in the imaged regions. This SQ is best addressed via observations within 3 <L-shell< 4, where plasmapause erosion is weakly active during quiet or moderately-disturbed times.

PILOT Science Objective 2 (Ob2)

Discover the pathways and processes governing cold plasma mass transport through and out of the inner magnetosphere.

[SQ 2a] What are the key *pathways* for transport of plasma mass through and out of the inner magnetosphere?

After cold plasma mass reaches the magnetosphere, it is distributed and transported to other magnetospheric regions. Known mass transport pathways include plasmaspheric plume flows [39], sub-auroral polarization streams (SAPS) [40] and sub-auroral ion drifts (SAID) [41]. Speculated pathways include interchange instability [42], and the warm plasma cloak [43, 44]. Each transport pathway is driven by different, sometimes competing, physical mechanisms. Limited existing measurements [4] do not elucidate which mass flow pathways are most important under which geomagnetic conditions, what feedback exists among transport mechanisms, nor how these mechanisms combine to produce the observed distribution of magnetospheric mass.

Each of the known transport pathways listed above have either a distinct spatial morphology, or a signature in ion energy space (as cold plasma is energized or cooled). Closure on this SQ requires comparing the observed morphology of cold plasma flows in the near-equatorial magnetosphere, and signatures of cold ion heating or cooling, against theoretical expectations for each pathway.

Closure on this SQ requires rapidly refreshing (< 60 s) images of total plasma density in the near-equatorial plane across broad regions of the inner magnetosphere. Observations must target the $3 < L < 6$ region where strong transport is observed. Simultaneous meridional plasma flow information determines whether equatorial plasma density changes are due to flow out of the equatorial plane or within it. Embedded in-situ observations of both light and heavy ion (H^+, He^+, O^+) distribution functions spanning 0.1 eV to 100 eV are required to observe heating or cooling of cold plasma that may be a prerequisite for some transport pathways [43]. Evaluating the suspected primary transport pathways requires measurements at all local times.

[SQ 2b] What are the *mechanisms* of plasma mass transport in the inner magnetosphere and their drivers?

Once ionospheric plasma mass reaches the plasmasphere, it is distributed and transported to other magnetospheric regions. It may go sunward to the dayside magnetopause and participate in reconnection, or it may be diverted to the flanks and travel anti-sunward to load the plasmasheet. Which fundamental processes dictate the transport and distribution of this mass?

Mass transport should be primarily determined by the dynamic electric and magnetic fields in the magnetosphere. But current models are based on electrostatic potential contours, and therefore entirely omit any contributions from induced electric fields. Further, these models are statistical and heavily averaged (e.g. [45]), making them inapplicable to extreme geomagnetic conditions (Table 2.1), and causing them to obscure natural small-scale features that critically impact transport, like SAPS and SAID [46, 47, 48]. These models are unsuccessful at reproducing many plasmaspheric structures observed by IMAGE EUV instruments (including notches, crenulations, fingers and shoulders [49]), demonstrating that key mechanisms of mass transport remain highly uncertain [50, 51, 52].

Answering this science question requires comparing electric and magnetic fields in the inner magnetosphere with resulting plasma mass motions, allowing key transport mechanisms to be identified. Measuring bulk plasma motion requires rapidly refreshing (< 60 s) images of total density in the equatorial plane. These images must cover a region spanning $3 < L - shell < 6$ in radial distance and ~ 3 hrs in MLT, with a resolution of $\sim 0.5\ R_E$. Embedded in the 2D images plane, in-situ point observations of DC-coupled electric and magnetic fields, along with measurements of cold proton, electron, and heavy ion distribution functions, provide ground truth point-sampling of the cold plasma bulk motion and the electric fields that drive it. Simultaneous meridional imaging of cold plasma flow is required to quantify transport into and out of the equatorial plane (with He^+ as a proxy for H^+ [36, 37]). This set of measurements unequivocally enable determination of the mechanisms and drivers of cold plasma mass transport.

PILOT Science Objective 3 (Ob3)

Determine how, where, and when cold plasma mass acts most efficiently to regulate coupling between magnetospheric regions and between plasma populations.

[SQ 3a] To what degree does the dynamic distribution of plasma mass regulate the expression of Alfvén waves?

Propagating at the Alfvén speed, Ultra Low Frequency (ULF) waves carry information via magnetic field fluctuations that enable magnetosphere-ionosphere coupling [53], magnetosphere-solar wind coupling [54], as well as radiation belt energization, loss, and particle transport via radial diffusion [55, 56, 57]. ULF waves are continuously driven at all MLT, and steep plasma gradients that most impact their propagation occur near the plasmapause.

Addressing this SQ requires measuring the dynamic spatial distribution of Alfvén speed, across scale sizes, over a broad region of the inner magnetosphere, and quantifying the degree to which it regulates ULF plasma wave behavior.

Determining the spatial distribution of Alfvén speed over a broad region of the near-equatorial inner magnetosphere requires a network of magnetic field measurements and 2D total plasma density maps that refresh on timescales faster than plasma mass or magnetic field are redistributed in order to resolve temporal changes to this distribution (anticipated to be minutes or faster). A network of magnetic field measurements is also required to measure fluctuating ULF-wave magnetic fields to establish how ULF wave amplitudes, modes (e.g., field line resonance or propagating mode), and wave spatial distribution are determined by the spatial distribution of total plasma density. Also, the Alfvén speed is a function of plasma mass density. Therefore, point measurements of ion composition (H^+, He^+, and O^+) embedded within the 2D total plasma density map plane are required to constrain the extent to which the spatial distribution of cold heavy ions impacts ULF wave properties.

[SQ 3b] By what mechanisms and to what extent does the distribution of plasma mass govern the dynamics of meso-scale plasma flows that reach the inner magnetosphere?

Bursty plasma flows from the magnetotail toward Earth [58, 59, 60, 61, 62] drive magnetic flux sunward as an integral part of the solar-wind driven Dungey cycle [63]. These flows decelerate [64, 65, 66] as they approach the cold dense plasma near Earth, depositing their flow energy into the auroral ionosphere [67, 68, 69, 70, 71] and injecting radiation belt source and seed particles [57].

PILOT achieves closure on this SQ by determining the extent to which cold plasma regulates plasma flow evolution in the inner magnetosphere, including particle injection physics and energy transfer from flows to plasma waves.

Cross-scale measurements, made in concert, are needed to answer this SQ. A network of magnetic field sensors and rapidly-refreshing equatorial total density maps (< 15 s, §F) are required to answer long-persistent questions about the spatial structure and deceleration of flows as they reach the inner magnetosphere (e.g., [62, 64, 72]). A network of energetic electron flux measurements definitively connect flow deceleration with specific electron injection properties, including energy-dependent radial penetration [72, 73, 74, 75, 76, 77, 78]). Embedded within the density map plane, in-situ ground-truth observations are needed. Electron, proton, and heavy ion distribution functions across a wide range of energies (0.1 eV to 1 MeV for e- and p^+, up to 50 keV for heavy ions) determine the evolution of flow-entrained particles [79]. DC-coupled electric and magnetic field observations are required to definitively identify injection flows. AC-coupled electric and magnetic field measurements are needed to observe dissipation of flow energy into plasma waves. Meridional plasma flow observations constrain the amount of new ion outflow that results from flow-breaking energy input to the ionosphere [80] during the dissipation (using He^+ as a proxy for H^+ [36, 37]).

At least 70 flow events per year travel earthward of $6R_E$, and they are best detected between midnight and dusk MLT [81]. Their characterization requires total density image spatial resolution of ≤ 0.5 R_e [82, 83]. A typical flow event is 1 to $2R_E$ in radial and azimuthal spatial extent, traveling earthward at 35 km/s, with a total plasma density (n_e) fractional depletion of $\Delta n_e/n_e \approx 50\%$ [61, 64, 84].

[SQ 3c] To what extent does the dynamic distribution of plasma mass in the magnetosphere determine the expression of wave-particle interactions that energize, de-energize, and precipitate energetic plasma?

Plasma waves are a fundamental driver of particle energization and loss in the inner magnetosphere [57, 85, 86]. Cold plasma density strongly determines the efficiency of the relevant wave-particle interactions [87, 88, 89, 90], and may control electron acceleration to multi-MeV energies [78]. Our knowledge of the spatial extent of these processes currently relies on an elaborate chain of complex modeling and statistical inference (e.g., [4, 91, 92, 93, 94, 95, 96]). Predictions resulting from this chain often sharply disagree with any individual geomagnetic event [97, 98] (especially for extreme driving cases (Table 2.1)), blurring our picture of which physical processes are most relevant under which geomagnetic conditions.

Plasma waves are freshly excited in the inner magnetosphere between $3 \leq$ L-shell ≤ 6 every few days on average, even during weak geomagnetic driving conditions [92, 99]. Very Low Frequency (VLF) electron-driven chorus waves occur most often in the dawn MLT sector [92], whereas ion-driven Electromagnetic Ion Cycltron (EMIC) waves occur most often in dusk MLTs [100]. Plasmaspheric VLF hiss waves appear at all MLTs [96, 101].

A definitive answer to this SQ requires determining the degree to which the dynamic spatial distribution of cold plasma mass and magnetic field controls the expression (growth, damping) of plasma waves over a broad region of the inner magnetosphere.

A network of magnetic field measurements and rapidly refreshing total plasma density maps are required to define the two-dimensional spatial distribution of plasma wave growth conditions near the magnetic equatorial plane. Embedded in this two-dimensional space, in-situ measurements of electron, proton, and heavy ion particle distribution functions, along with AC-coupled electric and magnetic fields, provide ground truth point-sampling of energy transfer from particles to plasma waves as the surrounding density and magnetic field conditions that regulate wave properties vary in time and space. Together, these measurements determine the spatial distribution and temporal variability of regions favorable for plasma wave growth over a broad region of the inner magnetosphere.

2.2.1 Connection to STP and Heliophysics Objectives

PILOT science objectives (Ob1, Ob2, Ob3) directly address all three of the STP science objectives in Table 2.1. PILOT Ob1 and Ob2 directly address STP#2 by discovering pathways of mass flow and transport that are key to determining the role of a planetary magnetic field in atmospheric loss, and therefore habitability. PILOT Ob3 addresses STP#3 by determining how, where, and when plasma mass density regulates magnetospheric subsystems that impact human and robotic safety and productivity, including the radiation belts. All three PILOT science objectives directly address STP#1 by discovering fundamental physical processes that drive mass and energy flow through a planetary magnetosphere, as well as the resulting regulation of magnetospheric subsystem dynamics.

PILOT science objectives significantly impact heliophysics as a whole (Table 2.1). PILOT provides an essential missing piece of magnetospheric physics—plasma mass transport—whose inclusion finally allows a true understanding of how the terrestrial magnetosphere comprises interconnected elements of a single 'system of systems' [4]. Ob1 and Ob2 determine plasma mass transport physics, and Ob3 defines how mass transport medi-

ates the coupling between magnetospheric subsystems. Thus, PILOT science directly aligns with the vision for Heliophysics laid out by the Science 2020-2024 document [102]. PILOT revolutionizes our understanding of Sun-Earth interactions by focusing on how mass flow within the terrestrial magnetosphere responds to space weather forcing.

2.2.2 Impact of Decrease in Constellation Size

PILOT achieves its science objectives with 34 total spacecraft (30 RadioSats, 2 PlasmaSats, 2 PlasmaSatEUV, as described in §3). PILOT's ability to address its science objectives gracefully degrades as the number of spacecraft in the constellation are reduced.

The number of unique lines of sight linking the RadioSats determines the spatial resolution ($\delta\mathbf{r}$) of near-equatorial plasma density images. This resolution $\delta\mathbf{r}$ coarsens as the number of RadioSats is decreased (quantified in §D.1). If the density image resolution becomes worse than $\sim 1\,R_E$, all three objectives are significantly degraded: (1) At $\delta\mathbf{r} > 1\,R_E$, Ob1 studies of mass outflow and return are degraded as adjacent flux tubes experiencing unique refilling or loss rates cease to be spatially separable in the equatorial plane. (2) At $\delta\mathbf{r} > 1\,R_E$, Ob2 studies of electric field driven plasmaspheric mass transport are degraded, as only the largest meso-scale plasmapause structures remain resolvable. (3) At $\delta\mathbf{r} > 1\,R_E$, Ob3 studies of plasma injections are degraded, as only the largest injection structures remain resolvable [82, 83]. 30 RadioSats are required to meet the baseline $0.5R_E$ resolution with 100% duty cycle. $0.5R_E$ resolution is achievable with 26 RadioSats, but with reduced duty cycle $\sim 40\%$ due to fewer intervals of sufficient spacecraft density near apogee. $1.0R_E$ resolution with 100% duty cycle is achievable with 24 RadioSats.

Near-continuous temporal coverage is important for PILOT, because solar wind variability-driven events can occur at any time. Reducing the number of embedded in-situ spacecraft reduces the observation duty cycle. Based on the nominal PILOT orbits (§4.4.4), two PlasmaSatEUV spacecraft enable meridional imaging measurements ($L \geq 5$) for 100% of the mission duration. These observations are vital for Ob1 and Ob2, and impact Ob3 (Table STM-1). On the inner orbit, two PlasmaSats enable density-image embedded composition measurements (key for Ob1, Ob2) for $L \geq 3$ over 100% of the mission. Removing a PlasmaSat from the inner orbit reduces temporal coverage of ion composition measurements to 64%. Removing a PlasmaSatEUV from the outer orbit reduces EUV imaging temporal coverage to 52%. If one PlasmaSat is removed, but both PlasmaSatEUV are retained, then ion composition temporal coverage of $3 \leq L \leq 4$ is only reduced to 73%, because PlasmaSatEUV orbits also cross $3 \leq L \leq 4$.

In 2013, a weak solar maximum, $\sim$20 geomagnetic events led to 'significant' plasmasphere erosion (down to $L \leq 3$) and subsequent refilling. Therefore, a 3-year prime mission duration enables comprehensive PILOT data (equatorial density mapping + meridional imaging + in situ) for $\geq$60 significant erosion events. Combined with an orbital precession rate of 1.7 years / 24 hours MLT (§4.4.4), $\geq$15 events are expected in each MLT quadrant. The number of comprehensively measured events is reduced by approximately half by the removal of either 1 PlasmaSat or 1 PlasmaSatEUV.

2.3 PILOT Mission Concept Science Traceability

Table STM-1 shows traceability from STP goals to PILOT science objectives and to required measurements. Table STM-2 shows traceability from required measurements

to quantitative measurement characteristics, and to mission concept payload instruments. Flow from required measurements to mission design is shown in Table G.2. Technical implementations of each measurement are described in §4. Mission implementation requirements that drive design decisions are summarized in Table G.2. Inability to maintain co-precession would significantly impact the radio tomographic resolution required to meet the PILOT science requirements. Reduction of constellation size by more than six RadioSats would decrease radio tomographic resolution to below that required to meet science objectives.

3 Mission Concept Implementation

3.1 Overview

The PILOT mission concept uses a constellation of spacecraft to measure plasma nearly invisible to most prior observations—simultaneously across a broad range of scale sizes. PILOT science requirements are met by 30 identical microsat spacecraft ("RadioSats") and four smallsat spacecraft ("PlasmaSats") in two near-equatorial, highly elliptical orbits.

The PILOT orbits (*Inner*: 1.52 R_E × 4.25 R_E and *Outer*: 1.10 R_E × 6.25 R_E; see Figure 3.1) are chosen to optimize measurements of the outer plasmasphere, plasmapause, and plasmatrough. PILOT measurements consist of near-equatorial plasma density maps derived from radio tomography, meridional EUV images, as well as embedded in-situ fields and particle measurements. This ground-breaking combination of measurements allows PILOT to observe critical physics of plasmasphere refilling, mass transport throughout the inner magnetosphere, and mass density regulation of magnetospheric subsystems.

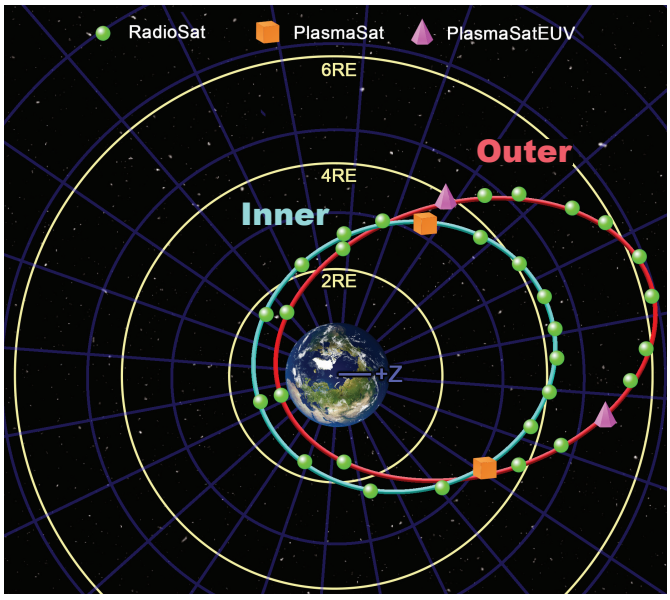

Figure 3.1: *PILOT spacecraft orbits.*

Radio tomography (§D.1), active plasma sounding, in-situ magnetic field, and in-situ energetic electron flux measurements are made by 14 RadioSats in the inner orbit and 16 RadioSats in the outer orbit. These 30 spacecraft are identical. Table 3.1 shows the RadioSat instrument complement and their heritage. The notional spacecraft are described in §4.1.

Tomographic measurements are complemented by PlasmaSat sampling of DC and AC electric and magnetic fields; high-energy ion and electron flux, distributions in energy and pitch angle, and composition; and local electron density. These measurements are made by four PlasmaSats. They are nearly identically-instrumented, except that the two PlasmaSats in the outer orbit, PlasmaSatEUVs, carry EUV cameras to measure the spatial distribution and flow of He^+ and O^+ ions in the meridional plane (with He^+ acting as a proxy for H^+ [36, 37]). PlasmaSat instrumentation and heritage is shown in Table 3.2.

Table STM-1: Science Traceability, STP to Required Measurements

Solar Terrestrial Probes (STP) Science Objectives	PILOT Science Goal	PILOT Science Objectives	PILOT Science Questions	Target Physical Processes	Required Measurements: Network 1	2	3	4	Embedded In Situ and EUV 5	6	7	8	9	10	11	12	13	14	15	16	17	18	19
STP #1: Understand the fundamental physical processes of the complex space environment throughout our solar system, which includes the flow of energy and charged material, known as plasma, as well as a dynamic system of magnetic and electric fields. **STP #2:** Understand how human society, technological systems, and the habitability of planets are affected by solar variability and planetary magnetic fields. **STP #3:** Develop the capability to predict the extreme and dynamic conditions in space in order to maximize the safety and productivity of human and robotic explorers.	Determine the primary pathways of mass and energy flow through the coupled systems of the terrestrial magnetosphere	[Ob1] Identify and quantify the key processes that govern mass and energy exchange between the ionosphere and the magnetosphere.	[SQ1a] How is the plasmasphere refilled from ionospheric sources?	Ionospheric outflow	●	●	●		●	●				●			●		●				●
				Plasmasphere refilling	●	●	●		●	●				●			●		●	●	●	●	●
				O+ torus evolution	●	●	●			●				●	●		●	●	●		●		
			[SQ1b] By what processes, and to what extent, does plasmaspheric mass return to the ionosphere or neutral exosphere?	Ionosphere return flow	●	●	●		●	●	●	●		●	●		●	●	●				
		[Ob2] Discover the pathways and processes governing cold plasma mass transport through and out of the inner magnetosphere.	[SQ2a] What are the key pathways for transport of plasma mass through and out of the inner magnetosphere?	Plume evolution	●	●	●		●	●				●	●		●	●	●		●		●
				Interchange instability	●	●	●		●	●				●			●		●				●
				Plasma cloak	●	●	●		●		●	●		●	●		●	●	●				●
			[SQ2b] What are the mechanisms of plasma mass transport in the inner magnetosphere and their drivers?	Mass transport	●	●	●		●	●	●			●					●		●		●
				Micro/meso E-fields	●	●	●		●	●	●	●		●	●				●		●		●
		[Ob3] Determine how, where, and when cold plasma mass acts most efficiently to regulate coupling between magnetospheric regions and between plasma populations.	[SQ3a] To what degree does the dynamic distribution of plasma mass regulate the expression of Alfvén waves?	Alfvén speed and ULF waves	●	●	●		●	●				●			●		●		●		●
			[SQ3b] By what mechanisms and to what extent does the distribution of plasma mass govern the dynamics of meso-scale plasma flows that reach the inner magnetosphere?	Injection flow dynamics	●	●	●	●	●	●	●	●	●	●	●	●	●	●	●	●	●	●	●
			[SQ3c] To what extent does the dynamic distribution of plasma mass in the magnetosphere determine the expression of wave-particle interactions that energize, de-energize, and precipitate energetic plasma?	VLF and EMIC plasma waves	●	●	●												●	●	●	●	●
				Warm / hot e-, i+ wave growth contributions	●	●	●	●				●	●		●	●			●				●

	Network				Embedded In Situ and EUV														
#	1	2,19	3,15	4	5	6	7	8	9	10	11	12	13	14	16		17		18
Class	Density		EM Fields	Electrons	Photons		Electrons			Protons			Heavy Ions		EM Fields				
Type	Total Plasma Density		Magnetic Field	Energetic e-	He+	O+	Cold e-	Warm e-	Energetic e-	Cold p+	Warm p+	Energetic p+	Cold He+, O+	Warm He+, O+	Magnetic Field		Electric field		
Detail	Equatorial 2D	In situ	DC-coupled, In situ	Trapped Flux	Meridional Profile		Pitch Angle Distributions			Pitch Angle Distributions			Pitch Angle Distributions		AC-coupled		DC-coupled		AC-coupled

Measurement # Key

Table STM-2: Science Traceability, Required Measurements to Notional Instruments

Network Measurements			Range	Cadence	Accuracy	Precision	FOV	Spatial Coverage	Notional Instrument	Mission Requirements
#	Type	Detail								
1	Total plasma density	Equatorial 2D	0.5 to 2,000 cm^{-3}	≤ 15 s between samples	25% Δn/n or 5 cc	25% Δn/n or 1 cc	Near-equatorial 2D plane	3 ≤ L-shell ≤ 6 ΔMLT ≥ 3 Resolution ≤ 0.5 Re	RT RF	30 identically instrumented spacecraft Near-equatorial orbits, Coverage between L = 3, 6 ≥ 24 hr MLT precession in mission lifetime S/C separation for 0.5 Re resolution
2		In situ	0.5 to 2,000 cm^{-3}	≤ 10 s between samples	25% Δn/n or 5 cc	25% Δn/n or 1 cc	-	At every RT node to constrain RT inversions	RT APPS	30 identically instrumented spacecraft Near-equatorial orbits, Coverage between L = 3, 6 ≥ 24 hr MLT precession in mission lifetime
3	Magnetic Field	DC-coupled	1 to 10,000 nT	≤ 15 samples per s	|B| ≤ 5 nT	≤ 0.1 nT	3 vector components	3 ≤ L-shell ≤ 6 ΔMLT ≥ 3	FGM	
4	Energetic e-	Trapped Flux	0.1 to 1 MeV	≤ 15 s between samples	ΔE/E ≤ 30%	ΔE/E ≤ 30%	≥ 45° cone near 90°	3 ≤ L-shell ≤ 6 ΔMLT ≥ 3	EED	
Embedded In Situ & EUV Measurements			**Range**	**Cadence**	**Accuracy**	**Precision**	**FOV**	**Spatial Coverage**	**Notional Instrument**	**Mission Requirements**
#	Type	Detail								
5	He+	Meridional Profile	4–400 cm^{-3}	≤160 s	Δn/n ≤ 50%	Δn/n ≤ 50%	106° x 56°	L ≤ 8 (r ≤ 8 Re, |z| ≤ 3.2 Re)	EUVCS EUV-He	Data from L-shell ≥ 5 for ≥ 50% of mission
6	O+		10–100 cm^{-3}	≤1800 s	Δn/n ≤ 50%	Δn/n ≤ 50%	80° x 37°	L ≤ 5 (r ≤ 5 Re, |z| ≤ 2 Re)	EUVCS EUV-O	
7	Cold e-	Pitch Angle Distributions	0.1 to 100 eV	≤ 15 s between samples	ΔE/E ≤ 30%	ΔE/E ≤ 30%	~4π str ≤ 20° PA bins	Point measurements Inside RT network	PIMS	Simultaneous data near L-shell = 4, 6 Near-equatorial orbits, crossings of L = 4, 6 ≥ 24 hr MLT precession in mission lifetime
8	Warm e-		0.1 to 50 keV							
9	Energetic e-		0.1 to 1 MeV				~4π str ≤ 40° PA bins		EPD	
10	Cold p+	Pitch Angle Distributions	0.1 to 100 eV				~4π str ≤ 20° PA bins		PIMS	
11	Warm p+		0.1 to 50 keV							
12	Energetic p+		0.2 to 1 MeV				~4π str ≤ 40° PA bins		EPD	
13	Cold He+, O+	Pitch Angle Distributions	0.1 to 100 eV He+ to O+				~4π str ≤ 20° PA bins		PIMS	Simultaneous data near L-shell = 4, 6 Near-equatorial orbits, crossings of L = 4, 6 ≥ 24 hr MLT precession in mission lifetime Data in EUV FOV for ≥ 50% of mission
14	Warm He+, O+		0.1 to 50 keV He+ to O+							
15	Magnetic Field	DC-coupled	1 to 10,000 nT	≥ 10 samples per s	|B| ≤ 5 nT	≤ 0.1 nT	3 vector components	Point measurements Inside RT network	EMF FGM	Simultaneous data near L-shell = 4, 6 Near-equatorial orbits, crossings of L = 4, 6 ≥ 24 hr MLT precession in mission lifetime
16	Magnetic Field	AC-coupled	10 to 15,000 Hz	≥ 2 Spectra / s	$1x10^{-9}$ nT^2 / Hz @ 500 Hz	$1x10^{-9}$ nT^2 / Hz @ 500 Hz			EMF SCM	
17	Electric Field	DC-coupled	0.1 to 500 mV/m	≥ 10 samples per s	|E| ≤ 2 mV/m	≤ 0.1 mV/m	2 vector components		EMF EFI	
18		AC-coupled	10 to 500,000 Hz	≥ 2 Spectra / s	$1x10^{-14}$ $(mV/m)^2$ / Hz @ 500 Hz	$1x10^{-14}$ $(mV/m)^2$ / Hz @ 200 Hz				
19	Total plasma density	In situ	0.5 to 2,000 cm^{-3}	≥ 2 samples per s	25% Δn/n or 5 cc	25% Δn/n or 1 cc	-	Point measurements Inside RT network	EMF APPS	

The definition of PILOT instrumentation flows directly from the science objectives (Table STM-1, STM-2) and their associated measurement requirements. Instrumentation baselined for PILOT draws on instrument heritage from NASA missions such as THEMIS, MAVEN, STEREO, IMAGE, Van Allen Probes and Parker Solar Probe.

The PILOT flight system design is driven primarily by the orbits required to achieve the science. The two selected orbits (described in §4.4.4 and §G.3), are required to precess at the same rate for the full mission duration (three years), and necessarily traverse a high-radiation environment. Because of this co-precession requirement, and to achieve precession through all MLTs within the mission lifetime, the inner orbit has a perigee of 1.52 R_E. This requires a delta-V of 40 m/s to comply with the NASA spacecraft disposal requirement at end of mission, which is accomplished by lowering the apogee to 19,000 km, to place the spacecraft in a stable disposal orbit between LEO and GEO, per NASA-STD-8719-14B. The outer spacecraft, with a perigee of 1.1 R_E, are disposed of by deorbiting into the atmosphere, which requires a delta-V of 57 m/s. Radiation requirements of up to 125 krad-Si/year and the need to limit the bit error rate to that experienced by the Van Allen Probes EMFISIS instrument on-board memory (30-40 per year), drive parts selection and shielding mass. A full description of mission requirements is found in §G.2.

The PILOT constellation is launched on two Falcon Heavy LVs (launch vehicles), one for each orbit, from Cape Canaveral, Florida. After launching into an initial 185 × 200 km orbit with 28 degree inclination, the LVs drift to the equator and perform a burn to raise the apogee (4.25 R_E for the inner orbit, 6.25 R_E for the outer orbit). Once at apogee, the LVs perform another burn to lower the inclination to 0 degrees and deploy all spacecraft. PILOT has no launch window constraints.

PILOT is designed as a Class C mission, and implements a resilient mission architecture. For example, if one RadioSat fails before reaching baseline mission duration, the remaining RadioSats can be re-positioned to meet minimum resolution required for science observations with a slightly reduced duty cycle (§2.2.2).

Acronym	Instrument Type	Measurement	Heritage
RT	Radio tomography/relaxation sounder	Total e- content, in-situ e- density	N/A (RT), MAVEN/LPW (sounder)
EED	Energetic electron detector	Energetic e- flux	AeroCube10 µCPT
FGM	Fluxgate magnetometer	Vector DC magnetic fields	ST-5

Table 3.1: *RadioSat instruments and heritage*

3.1.1 Mission organization

The notional PILOT mission organization is shown in Figure 3.2. Mission management is done at a NASA Center. Large-quantity instruments (RT, EED, FGM, EPS) are designed by research institutes and universities and the manufacture and test is competed commercially. Smaller-quantity PlasmaSat instruments are competed through the normal NASA selection process, and their design and manufacture test are assumed to occur at the same institution (as was done on other NASA multi-spacecraft mission such as THEMIS or MMS). System integration and testing are performed by the RadioSat spacecraft provider, and either at the managing NASA Center or by the PlasmaSat spacecraft provider. There are no specific individuals or institutions required to implement the PILOT concept.

Acronym	Instrument Type	Measurement	Heritage
EMF FGM	Fluxgate magnetometer	DC magnetic fields	ST-5
EMF SCM	Search coil magnetometer	AC magnetic fields	Van Allen Probes EMFISIS
EMF EFI	Electric field double probes	AC and DC electric fields	Van Allen Probes EFW
EMF APPS	Relaxation sounder	In-situ e- density	MAVEN LPW
PIMS	Ion mass spectrometer	Cold/warm, e-,p+,He+,O+ PADs	Van Allen Probes HOPE
EPS	Energetic particle spectrometer	Energetic e-/p+ PADs	GTOsat REMS
EUVCS EUV-He	He^{+} imager	He^{+} from 30.4 nm intensity	IMAGE EUV (sensor) Juno UVS (electronics)
EUVCS EUV-O	O^{+}/O^{++} imager	O^{+}/O^{++} from 83.4 nm intensity	

Table 3.2: *PlasmaSat instruments and heritage*

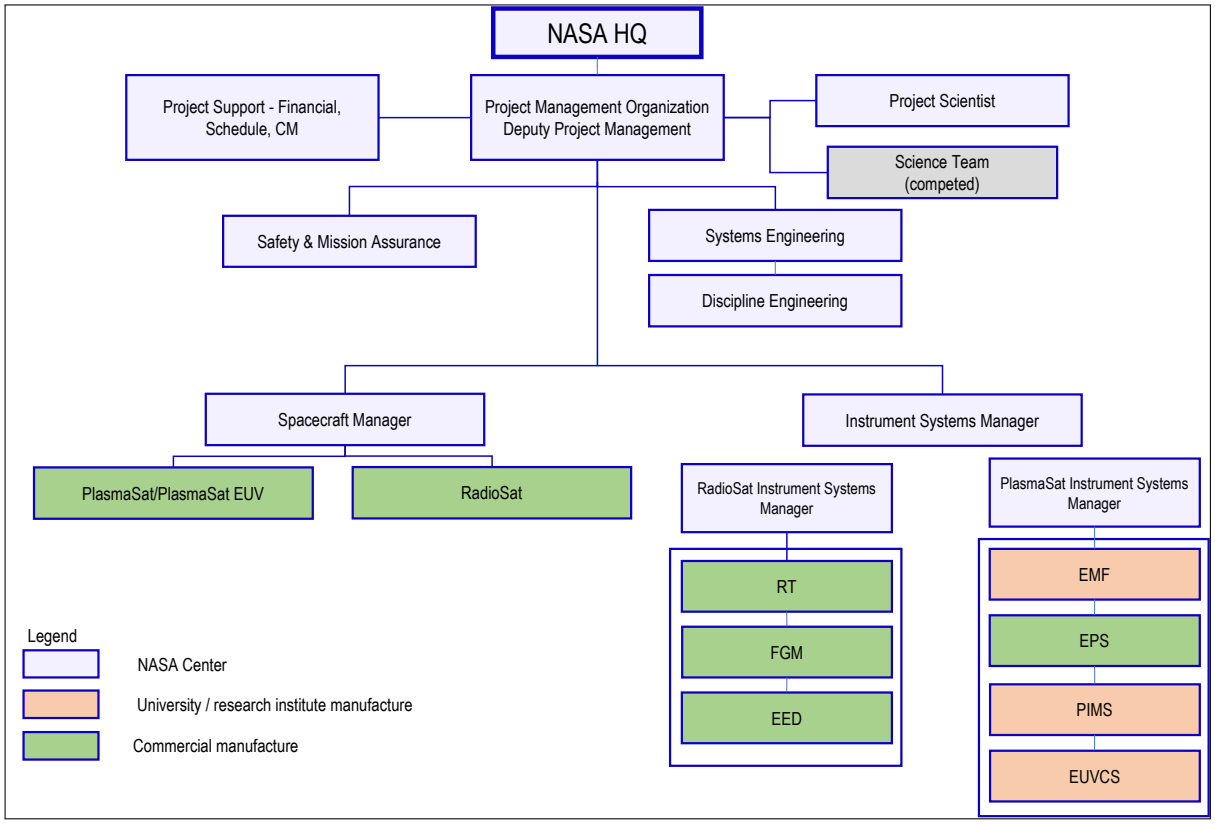

Figure 3.2: *Notional PILOT mission organization chart.*

3.2 Concept Maturity Level (CML)

PILOT has defined a detailed science traceability, with defined relationships and dependencies, partnering strategies, instrument and spacecraft heritage, key risks, and manufacturing strategies have been identified, and as such achieves a CML 5. This assessment is supported by the presentation of technology readiness for all instruments, spacecraft, and subsystems, as well as a detailed science traceability matrix, key technologies, heritage, risks, and mitigations.

3.3 Technology Maturity

Almost all spacecraft and instrument subsystems, subassemblies, and components are matured to at least a Technology Readiness Level (TRL) of 6, with several having achieved a TRL of 9. Payload TRLs are shown in Table 3.3. Technology maturation for RT, EUVCS, and potential biasing for the PIMS instrument is described in §G.6.

Element	Technology	TRL	Rationale
RT RF	Dual-frequency TEC measurement	4	Technique used in ionosphere for GPS signals; not yet demonstrated in plasmasphere at required frequencies
APS	Relaxation sounding	7	Electroncis board, simplfied from MAVEN LPW
FGM	DC magnetic fields	9	Identical to magnetometer for ST-5
EED	Detector stack particle telescope	7	Identical to AeroCube10 μCPT, additional shielding
EFI	Electric fields	9	Identical to Van Allen Probes EFI
SCM	AC magnetic fields	9	Identical to Van Allen Probes EMFISIS
PIMS	ESA with TOF section, surface potential control	7	Identical to Van Allen Probes HOPE, addition of voltage-biased spacecraft-mounting plate
EPS	Energetic particle spectrometer	7	Similar to GTOsat REMS, energy range adjustments
EUV He^+	EUV imaging of He^+	5	Based on IMAGE EUV, subsequent development
EUV O^+/O^{++}	EUV imaging of O^+/O^{++}	5	Simlar to EUV He^+, laboratory prototype demonstrated

Table 3.3: *Most PILOT payload instruments (§4) have significant flight heritage. The rest reach TRL 6 with minimal investment. See Section 5.2.*

3.4 Key Trades

Seven key trades drove the PILOT mission architecture and mission design. Key trades, rationale, and future considerations are described fully in §G.1. PILOT key trades are:

Deorbit propulsion type: To achieve the delta-V required to dispose the spacecraft at end of life, a number of propulsion systems with the capability to provide the required delta-V were examined. The primary implementations considered were an all-hydrazine system, an all-electric propulsion system, or a hybrid hydrazine-electric propulsion system. An all-hydrazine system was selected.

Number of launches: While it is desirable to launch all spacecraft on a single LV to minimize cost, the number of spacecraft, the required two orbits, and NASA guidance to use the current NASA launch services (NLS-II) contract, drove the selection of two launches. In consultation with LV providers, all 34 PILOT spacecraft could easily be placed into their orbits by one super-heavy LV, such as SpaceX's Starship, for significantly reduced cost. However, this concept study is limited to using those vehicles currently on the NLS-II contract, which requires two launches and associated expense.

Radiation hardening: PILOT spacecraft are necessarily in high-radiation orbits. As most baselined PILOT instruments are designed for use in a highly-shielded environment, radiation mitigation via shielding was chosen to preserve instrument heritage.

RadioSat bus: A plethora of micro- and mini-sat providers with capability to produce constellations has recently emerged. Beginning with the 22 commercial microsatellite

providers referenced in the State-of-the-Art Small Spacecraft Technology report ([103]), a cross-section of micro- and mini-satellite providers was examined and it was concluded that there is a healthy supply base to support PILOT constellation development. Designs from three spacecraft providers, representing established micro- and mini-satellite providers (Blue Canyon Technologies), emerging micro-satellite constellation providers (Muon Space), and universities (CU/LASP) were considered. The Muon Space design is presented here.

PlasmaSat bus Leveraging heritage science instruments, rather than focusing on miniaturization, drove the design to use a smallsat bus. This concept study focuses on existing manufacturers able to provide multiple spinning platforms for a high-radiation environment and Ball Aerospace provided the PlasmaSat bus concept design.

Two transmission frequencies vs. atomic clock: The PILOT radio tomography measurement (§D.1) requires two transmission frequencies to ensure accurate scientific measurements. It is also possible to provide an accurate measurement using one frequency by using an accurate atomic clock to precisely determine the absolute time of pulse transmission by each RadioSat. This trade determined that current spaceflight-compatible chip scale atomic clocks do not currently have the accuracy and stability ($\sim 10^{-12}$ s) to support PILOT science.

Multi-instrument manufacturing: PILOT has several large quantity instruments, which may be difficult to obtain through the traditional research organizations. This trade focused on utilizing traditional university instrument development vs. commercial manufacturers who could more easily produce hardware in mass quantities.

4 Technical Overview

The baseline PILOT configuration consists of 34 spacecraft: 30 RadioSats, 2 PlasmaSats, and 2 PlasmaSatEUVs. While the constellation could be launched with one super-heavy LV at far reduced cost, to comply with NLS-II constraints, the PILOT mission baseline uses two Falcon Heavy launch vehicles with 5-m fairings in the expendable configuration, one for each orbit. For each launch, all RadioSats are mounted on a single ESPA-Grande, using ExoLaunch ExoPods to mount four RadioSats to each port (Figure 4.2). For each launch, the two PlasmaSats or PlasmaSatEUVs are mounted on a separate, stacked ESPA-Grande, as shown in Figure 4.1.

4.1 RadioSat

PILOT includes 30 RadioSats, 16 in the outer orbit, and 14 in the inner orbit. An industry survey was conducted to determine the capability of spacecraft providers to produce 30 RadioSats that meet the PILOT science and environment requirements. Multiple providers were identified. The capabilities of three are considered here: Blue Canyon Technologies (BCT), Muon Space (Muon), and CU/LASP (LASP). These providers span the spectrum from established microsat providers (BCT), emerging manufacturers of large constellations (Muon) and universities (LASP). The Muon RadioSat design is used in this report as representative of microsat provider capabilities. A summary of mass and power for the notional RadioSats is shown in Table 4.3, and an image of the RadioSat flight system with the instrument suite is shown in Figure 4.3. See §G.4.1 for a detailed description of the RadioSat flight system.

4.1.1 Instrument Payload Description

Each RadioSat carries three scientific instruments: Radio Tomagraphy (RT), Fluxgate Magnetometer (FGM), and Energetic Electron Detector (EED). Table 4.1 provides mass, power, and data volume for the baseline RadioSat instruments.

The **RT** instrument consists of two subsystems: Radio Frequency (RF) and Active and Passive Plasma Sounder (APPS), both of which share the same dipole pair of axially-deployed 1.5-m stacer antennas for transmitting and receiving signals. RF transmits dual-frequency radio signals from each RadioSat to all other RadioSats. The RF on each RadioSat receives these signals and measures their relative phase delay to determine the total electron content (TEC) along the line of sight between spacecraft (§D.1). Two-dimensional total plasma density maps used for all PILOT SQ (§2.2, STM-1) are derived from a network of TEC measurements via tomographic inversion (§D.1). Previous studies of the feasibility of radio tomography for magnetospheric observation have been performed (e.g. [104]), and form the basis of this instrument concept. APPS is a relaxation sounder that measures in-situ electron density needed for radio tomographic inversion (§D.1). It is similar to Cluster Whisper [105] and the relaxation sounding portion of MAVEN/LPW [106]. APPS stimulates the ambient plasma with a low-power electrostatic pulse and measures the frequency of resultant plasma-resonant waves. It also measures these resonances passively (§C.1.2). The **FGM** measures the DC-coupled three-axis vector magnetic field, and is located at the end of a 2-m boom. The network of FGMs measure the detailed terrestrial magnetic field configuration, as well as spatial variation in ULF wave properties (§C.2). The **EED** is a compact solid state telescope that measures fluxes of trapped ($\sim 90^o$ pitch angle) electrons in the 50 keV - 3 MeV range, to determine how energetic particle injections and (SQ 3a) and plasma wave growth (SQ 3c) are regulated by the distribution of cold plasma mass in the inner magnetosphere.

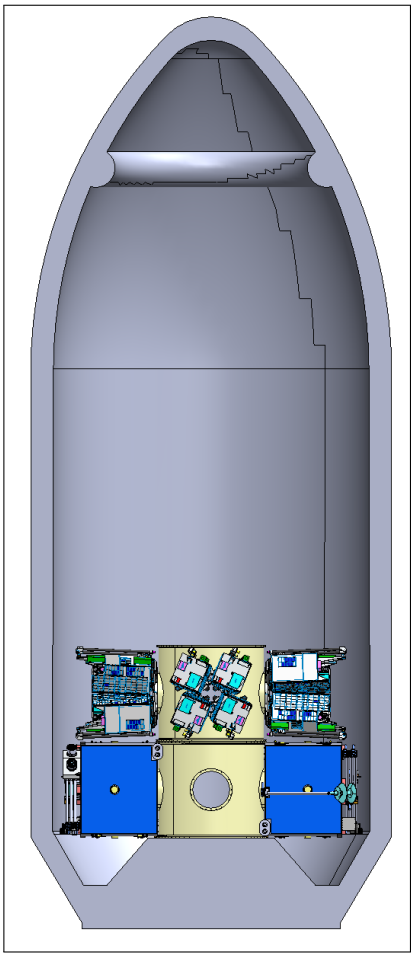

Figure 4.1: *16 Radiosats and 2 Plasmasats are easily accommodated by a Falcon Heavy LV*

4.1.2 RadioSat Spacecraft

The RadioSats bus design is driven by RT instrument power requirements, the radiation environment, and the propellant needed for disposal delta-V. RadioSats in the outer orbit are deorbited into Earth's atmosphere; RadioSats in the inner orbit are placed in a graveyard orbit between LEO and GEO, per NASA-STD-8719-14B.

RadioSats are deployed on two Space X Falcon Heavy LVs, one for each orbit, with four RadioSats mounted per ESPA-Grande port using ExoLanch ExoPod adapters (Figure 4.2).

Instrument	Mass			Average Power			Mission Data Volume (Gb)
	CBE (kg)	Cont (%)	MEV (kg)	CBE (W)	Cont (%)	MEV (W)	
RT	9.89	27	12.53	13.54	27	17.15	454
FGM	5.24	24	6.48	2.28	18	2.68	65.4
EED	0.34	12	0.38	0.12	15	0.13	63.6
Total	**14.91**	**26**	**18.74**	**15.36**	**26**	**19.29**	**583**

Table 4.1: *RadioSat instrument payload resources*

Item	RadioSat Instrument			Units
Instrument	RT	FGM	EED	
# channels	2 (50 MHz, 150 MHz)	3 (2 gain stages)	12	cm
Size/dimensions	20x20x15 (electronics) 10x10x25 (x2) (antennas - stowed)	10x12x5 (electronics) 106x6.5x15 (boom - stowed)	7.6x4.8x4.1 (instrument)	cm
Mass (CBE)	9.3	5.2	0.3	kg
Mass contingency	27.3	21.1	15.0	%
Mass with contingency	11.9	6.3	0.3	kg
Average power (CBE)	13.0	2.3	0.6	W
Power contingency	27.1	17.5	15.0	%
Power with contingency	14.5	2.7	0.7	W
Data rate (CBE)	4000	576	4	bps
Data rate contingency	20%	20%	25%	
Data rate w/ contingency	4800	691.2	5	bps
Field of view	Near-equatorial 2-D plane	N/A	48, full-angle cone	deg
Pointing knowledge	10 deg	0.1 deg	N/A	deg
Pointing control	10 deg	1 deg	N/A	deg
Pointing stability	N/A	0.1 deg/orbit	N/A	deg

Table 4.2: *RadioSat instrument payload characteristics*

For the inner orbit, 14 RadioSats are mounted on a single ESPA-Grande; for the outer orbit, 16 RadioSats are mounted on an ESPA-Grande. Once deployed from the LV, they use on-board propulsion to achieve spacing in mean anomaly such that they are bunched at apogee to increase radio tomographic image resolution. Each RadioSat carries an X-band high-gain antenna and S-band patch antenna, and contacts an Amazon Web Services ground station at each perigee for data downlink and commanding (§G.5). RadioSats are three-axis stabilized. The 0.1^o pointing knowledge requirement (Table 4.2) is met by combining data from the six sun sensors (providing pointing knowledge to 1^o) with comparisons between FGM measurements near perigee and geomagnetic field models. This approach was used on prior missions [107, 108] to achieve attitude knowledge that meets PILOT requirements. Reaction wheels are used for attitude control, with desaturation thruster firings performed as needed. To meet the 300 km position knowledge requirement (Table G.2), the RadioSats use GPS position determination near perigee combined with orbit modeling.

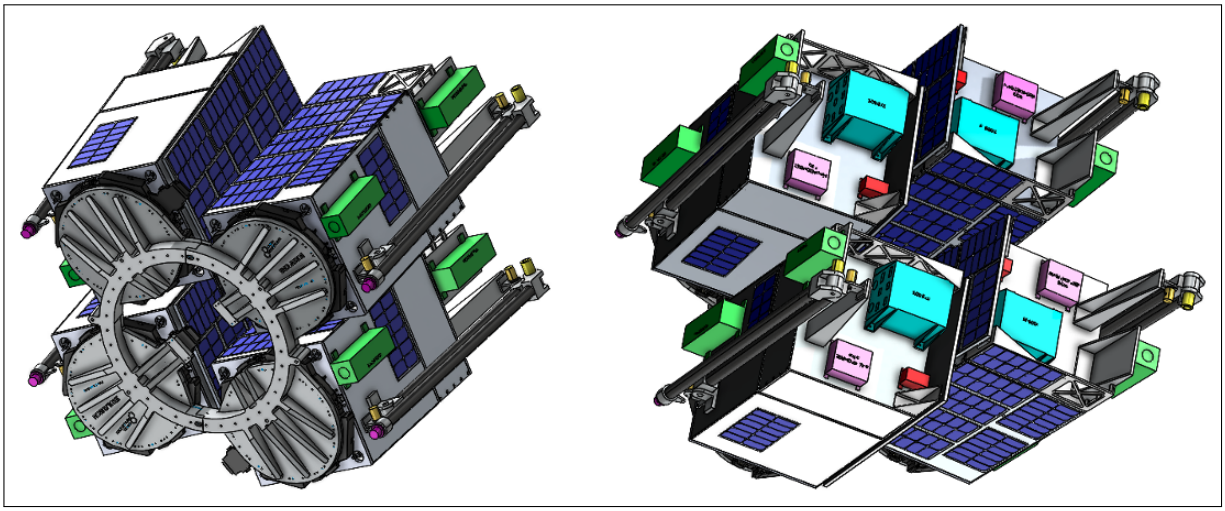

Figure 4.2: *Set of four RadioSat spacecraft mounted to a single ESPA Grande port.*

RadioSats use deployed solar arrays with multi-junction GaAs solar cells that provide 185 W Beginning of Life (BOL) to the spacecraft. The propulsion system mounts as a separate structural unit to the spacecraft bus, and is designed to carry launch loads. Table 4.3 shows RadioSat mass and power. A Master Equipment List was developed, and each component assigned a contingency based on TRL, consistent with AIAA and NASA GOLD Rules standards. All RadioSat bus subsystems have achieved TRL > 6. Detailed RadioSat design is discussed in §G.4.1. Radiation tolerance and reliability is achieved through parts selection, testing, and shielding (§G.4.1.8). RadioSat design and parts selection are guided by the need to withstand the radiation environment for the mission life. Spacecraft are manufactured using Class D Safety and Mission Assurance (S&MA) procedures, but achieve Class C through architectural redundancy, as PILOT baseline science requirements can be met with 26 RadioSats (§2.2.2).

	Mass			Power		
	CBE (kg)	Cont (%)	MEV (kg)	CBE (W)	Cont (%)	MEV (W)
Structures & Mechanisms	23.7	26%	29.80	0	--	0
Thermal Control	1.3	20%	2.0	8.0	20%	48.1
Propulsion (Dry Mass)	2.4	15%	2.8	39.0	20%	46.8
Attitude Control	5.9	13%	6.6	19.8	20%	48.1
Command & Data Handling	0.6	35%	0.8	22.0	20%	26.4
Communications	0.9	35%	1.2	25.0	20%	30.0
Power	9.7	44%	14.0	0	--	0
Total RadioSat Dry Mass	**44.5**	**29%**	**57.2**	**113.8**	**20%**	**199.4**
Propellant	4.5	25%	5.6	0	--	0
Total RadioSat Wet Mass	**49.0**	**29%**	**62.8**	**113.8**	**20%**	**199.4**

Table 4.3: *RadioSat bus system resources*

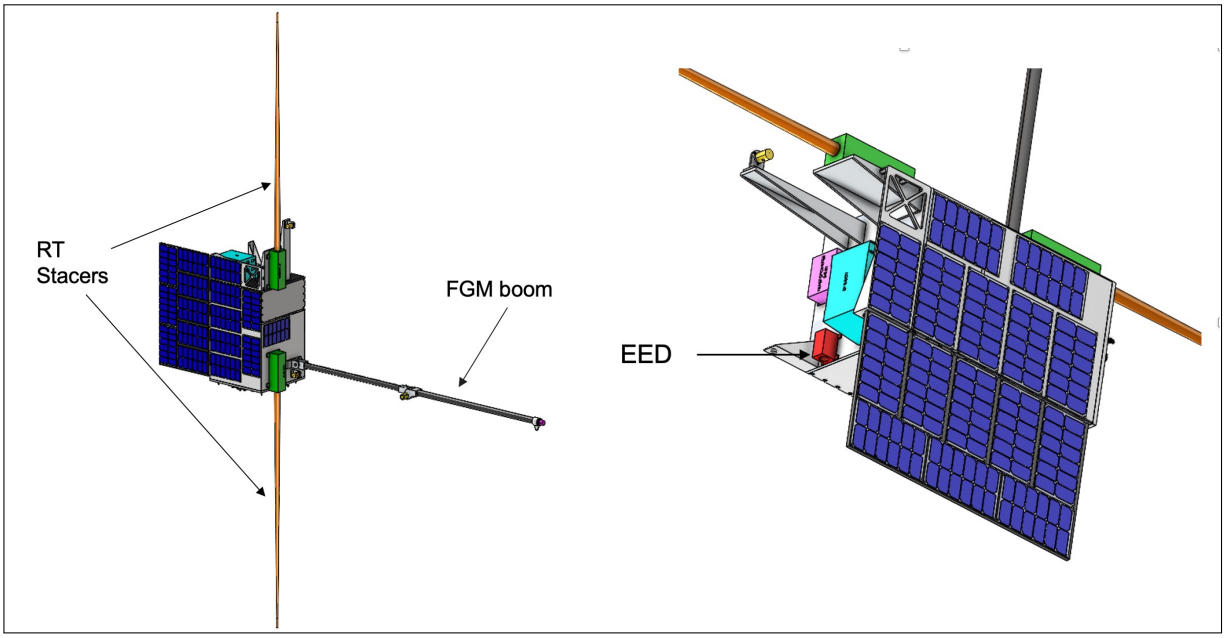

Figure 4.3: *RadioSat spacecraft, with instruments indicated.*

4.2 PlasmaSat

PILOT has four PlasmaSat spacecraft: two in the inner orbit without an EUV imaging instrument (PlasmaSats), and two in the outer orbit with an EUV imaging instrument (PlasmaSatEUV). The PlasmaSat design is based on the Ball Aerospace BCP-Small spacecraft, and is driven by the need to spin for particle and fields measurements, and to withstand the radiation environment. The 5 rpm spin rate is driven by EFI wire booms. The PlasmaSat propulsion system is driven by the delta-V needed for disposal (§3). A PlasmaSat mass and power summary is shown in Table 4.6.

4.2.1 Instrument Payload Description

All four PlasmaSats have identical spacecraft buses. All four carry identical copies of the Electromagnetic Fields (EMF) instrument suite, Energetic Particle Sensors (EPS), and the Plasmasphere Ion Mass Spectrometer (PIMS). The two outer-orbit PlasmaSatEUVs also carry an EUV Camera System (EUVCS). Table 4.4 provides mass, power, and data volume of PlasmaSat instruments.

The **EMF** suite measures in-situ electric and magnetic fields across a range of frequencies using several sensors. The electric field instrument (EFI) measures electric fields from DC to $\sim$ 500 kHz along two axes in the equatorial plane, as well as the spacecraft floating potential, using the double probe technique [109]. A fluxgate magnetometer (FGM) identical to the one flown on the RadioSats, measures the DC-coupled magnetic field vector, and a search coil magnetometer (SCM) measures the AC magnetic field vector. EMF includes identical APPS electronics to the RadioSats. The PlasmaSat APPS uses EFI antennas to broadcast and receive relaxation sounding signals. EMF suite instruments have have extensive heritage on magnetospheric missions including the Van Allen Probes [110, 111, 112] THEMIS [113, 114] and MMS [115, 116]. EMF measurements are key for identifying plasma

waves (SQ 1a,3a,3b,3c), determining particle pitch angles (all SQ), and measuring quasi-DC electric fields (SQ 1a,2a,2b,3a,3b). APPS-measured densities and EFI-measured spacecraft potential values are also used to calibrate plasma measurements by PIMS [117].

PIMS obtains in-situ distribution functions (flux versus energy, pitch angle, gyrophase angle) and derived moments (density, temperature) for three major ion species (H^+, He^+, O^+) and electrons. These local measurements provide essential microphysics and ground-truth information for multiple SQ: proton data required for all SQ, and He^+, O^+ data vital for SQ 1a, 2a, and 3a, and contextually important for SQ 3b and 3c (§2.2). PIMS is nearly identical to the Van Allen Probes HOPE instrument that comprises an electrostatic analyzer (ESA) with a time of flight (TOF) section [118]. Measurement of full cold ion distributions (down to ∼0 eV) is enabled by the Sensor-Panel Bias (SPB) system, which applies a voltage bias to the entire PIMS instrument and its adjacent spacecraft panel relative to spacecraft chassis ground. Biasing an instrument or its aperture has been performed previously, e.g., Cassiope/e-POP, Freja, and DE-1/RIMS [119, 120, 121, 122]. The PILOT SPB system allows cold ions to reach PIMS while minimizing angular deflection (§C.6). PIMS's modular design allows it to be biased with only very minor changes from HOPE. PIMS is mounted on the PlasmaSat such that it measures a full particle distribution in energy and pitch angle with each spin.

EPS consists of five electron and proton magnetic spectrometers per PlasmaSat. Together, they measure the in-situ energy flux and distribution functions of energetic electrons ($\sim$ 0.2 to $\sim$ 1.5 MeV) and protons ($\sim$ 0.15 to $\sim$ 8 MeV), required to address SQ 3b and SQ 3c. A full description is found in (§C.5). The field of view for each spectrometer is 20^o by 10^o, and five spectrometers are arranged on each PlasmaSat such that the 20^o portion of their fields of view are symmetrically distributed along the 180^o between PlasmaSat spin axes. This arrangement, combined with the spacecraft rotation, enables a nearly full sky coverage with the PlasmaSat spin axis orientation. Each individual PILOT EPS spectrometer is baselined to be an identical copy of the REMS instrument on GTOSat.[123] REMS is a miniaturized version of the MagEIS-Medium instrument on Van Allen Probes [124].

EUVCS comprises two imager types: EUV-He (2 cameras) and EUV-O (one camera). A full description is found in (§C.7). EUVCS provides global images of EUV light scattered from He^+ at 30.4nm (EUV-He) and O^+/O^{++} at 83.4nm (EUV-O). These populations are both high priority science targets (§2.2); He^+ is a reliable proxy for H^+ or electrons [36, 37], and the distinct dense O^+/O^{++} torus morphology can drastically alter the plasma mass density [37, 125]. EUVCS images the meridional ion distribution, orthogonal and complementary to the equatorial distribution obtained via radio tomography (§4.1.1). EUVCS images and their derived data products (density and flow inversions §D.2) are essential for SQ 1a, 1b, 2a, and 2b (§2.2), and provide important information about energy feedback for SQ 3a (§2.2). The optical design shared by both EUV-He and EUV-O is an evolution of the IMAGE EUV instrument [126], with an expanded 40^o field of view (FOV) and improved 0.45^o resolution [125, 127] to image structures as small as 0.05 R_E. EUVCS cameras take advantage of the PlasmaSat spin to cover the entire plasmasphere torus within about one third of a spacecraft rotation (§C.7). Deconvolution of EUVCS images extracts densities and convection flow velocities (§D.2).

Instrument	Mass			Average Power			Mission Data Volume (Gb)
	CBE (kg)	Cont (%)	MEV (kg)	CBE (W)	Cont (%)	MEV (W)	
EMF	31.8	19	37.7	7.5	15	8.6	4666
PIMS	22.1	15	25.4	32.7	15	37.6	1058
EUVCS	30.6	15	35.2	25.0	30	32.5	11714
EPS	6.7	20	8.0	9.4	30	12.2	199
Total	**91.1**	**17%**	**106.2**	**74.6**	**22%**	**90.9**	**17637**

*on PlasmaSatEUV s/c only

Table 4.4: *PlasmaSat instrument payload resources*

Item	PlasmaSat Instrument				Units
Instrument	EMF	PIMS	EPS	EUVCS	
# channels	3 (FGM), 3 (SCM), 1 (APPS), 6 (EFI)	10 channel e-multiplier detectors	9 (e-), 1 (p+)	2 (He+, O+/O++)	
Size/dimensions	106x6.5x15 (2x) (FGM/SCM Booms)	19.6x19.6x33.5 (Instrument)	4.25x4.42x2.1 for each EPS enclosure	25x25x33 (O+ Camera)	cm
	4x8x5 (4) (EFI Boom Deployer)			25x59x40 (He+ Cameras)	cm
	50x2x2 (SCM)			20x20x8 (Electronics)	cm
	7x7x5 (FGM)				cm
	20x20x15 (Electronics)				cm
Mass (CBE)	32.12	22.05	25.00	30.59	Kg
Mass contingency	18.51	15.00	30.00	15.00	%
Mass w/ contingency	38.06	25.36	32.50	35.18	Kg
Average power (CBE)	10.15	32.72	25.00	26.10	W
Power contingency	20	15	30	15	%
Power w/ contingency	12.85	37.63	32.50	30.02	W
Data rate (CBE)	38846	9320	2100	54940	bps
Data rate contingency	20	20	30	20	%
Data rate w/ contingency	46615.2	11184	2730	65928	bps
Field of view	N/A	162°x 4.5°	20°x 10°	40° Full Angle	deg
Pointing knowledge	0.1°	0.45°	N/A	0.03°	deg
Pointing control	1°	0.9°	N/A	0.1°	deg
Pointing stability	<0.1° per spin	0.05° per 2 second	N/A	0.1° per 2 second	deg

Table 4.5: *PlasmaSat instrument payload characteristics*

4.2.2 PlasmaSat Spacecraft

PlasmaSats are powered by body-mounted multi-junction GaAs solar cells that generate 290 W at BOL. PlasmaSats adopt a Class C mission assurance posture, with avionics redundancy and parts selection consistent with a Flagship-class mission in the PILOT radiation environment.

PlasmaSat and PlasmaSatEUV spacecraft are identical except for the EUVCS instrument. Spacecraft mass and power are shown in Table 4.6. See §G.4.2 for detailed de-

scription of the PlasmaSat and PlasmaSatEUV flight systems. PlasmaSat design is driven by instrument power requirements, the radiation environment, and propellant needed for disposal delta-V. PlasmaSats in the outer orbit are deorbited into Earth's atmosphere; PlasmaSats in the inner orbit are placed in a graveyard orbit between LEO and GEO, per NASA-STD-8719-14B. The notional design presented here demonstrates that this instrument suite can be accommodated on a smallsat-class spacecraft. Further design work may explore other spacecraft configurations, such as hexagonal or octagonal, to optimize instrument placement.

PlasmaSats are deployed on two Space X Falcon Heavy LVs, one for each orbit, on a single ESPA-Grande (4.1). Once deployed from the LV, they use hydrazine-based propulsion to achieve spacing such that the two PlasmaSats in each orbit are maximially separated along their orbit, and spin to 5 RPM. Each PlasmaSat carries an X-band high-gain antenna, and contacts an Amazon Web Services ground station throughout the orbit to downlink data, and uplink commands once per day. To meet the 0.1^o pointing knowledge requirement, star trackers are used for attitude determination. A reaction wheel is used for attitude control, with desaturation thruster firings performed as needed. Position knowledge is determined using delta differential one-way ranging (DDOR).

PlasmaSats use radiation-tolerant avionics. A Master Equipment List was developed, and each component assigned a contingency based on TRL, consistent with AIAA and NASA GOLD Rules standards. All PlasmaSat bus subsystems have achieved TRL $>$ 6. Radiation tolerance and reliability is achieved through parts selection, testing, and shielding. Propellant margin allocated contains 33% margin relative to delta-V required.

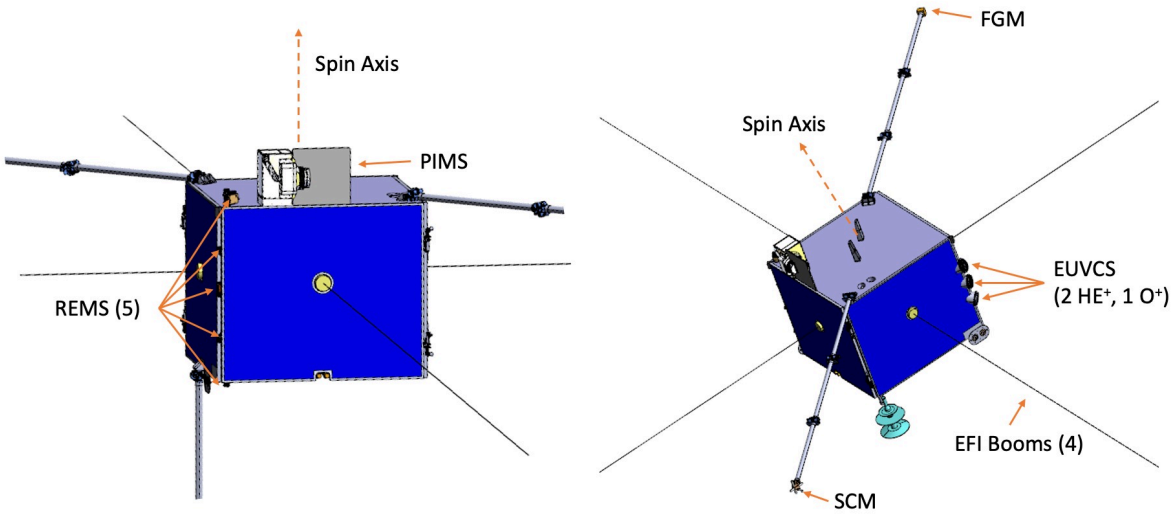

Figure 4.4: *PlasmaSat spacecraft, with instruments indicated.*

4.3 Instrument Production, Integration and Test

PILOT's approach to manufacturing and integrating 30+ identical copies of each RadioSat instrument is to perform a careful calibration of the first five copies of each

	Mass			Power		
	CBE (kg)	Cont (%)	MEV (kg)	CBE (W)	Cont (%)	MEV (W)
Structures & Mechanisms	104.2	21%	126.0	0	--	0
Thermal Control	6.6	20%	8.0	39.0	24%	48.36
Propulsion (Dry Mass)	15.7	8%	16.9	1.0	24%	1.24
Attitude Control	8.8	16%	10.2	0.4	24%	0.496
Command & Data Handling	5.9	5%	6.2	38.9	24%	48.236
Communications	11.7	13%	13.1	64.0	24%	79.4
Power	36.1	32%	47.6	0	--	0
Total PlasmaSat Dry Mass	**189.0**	**21%**	**228.0**	**143.3**	**24%**	**177.7**
Propellant	26.0	--	26.0	0	--	0
Total PlasmaSat Wet Mass	**215.0**	**29%**	**254.0**	**143.3**	**20%**	**177.7**

Table 4.6: *PlasmaSat / PlasmaSatEUV bus system resources*

instrument, then characterize other instruments at an acceptance level. Engineering Models (EMs) are used for the RT and EUVCS instruments, whose current TRL is below 6. Instruments are designed and parts selected to meet Flagship-class reliability. During instrument manufacture, Class D S&MA procedures are followed. Upon instrument delivery and acceptance, Class C S&MA procedures are followed until launch. Detailed instrument Integration and Test (I&T) discussion is found in §C.8.

4.4 Concept of Operations and Mission Design

4.4.1 Baseline Concept of Operations and Mission Design

The PILOT spacecraft are integrated onto two Falcon Heavy LVs, and launched from Cape Canaveral directly into two coplanar, near equatorial orbits: 1.52 x 4.25 R_E (inner) and 1.1 x 6.25 R_E (outer) (Table G.3). After being individually deployed by the LV into a string-of-pearls configuration, the spacecraft use on-board propulsion over the course of a month to achieve the mean anomaly spacing required for science operations.

The spacecraft contact an Amazon Web Services (AWS) ground station at each perigee. Downlink occurs at every perigee, and uplink occurs once per day (Table G.6). PlasmaSat/PlasmaSatEUV spacecraft use X-band for downlink and uplink using two X-band high-gain antennas. RadioSats downlink using an omni-directional X-band (high-gain) antenna and uplink using an S-band patch antenna. For a detailed description of mission operations, see §G.5.

4.4.2 RadioSat Concept of Operations

RadioSat spacecraft have two operational modes: Launch & Early Operations and Science. During Launch & Early Operations, all RadioSat spacecraft are checked out. After spacecraft checkout is complete, all instruments are powered on, the FGM booms are deployed, followed by the RT stacers, and instrument commissioning begins. After the RadioSats achieve their final orbital configuration, science operations begin. The FGM, RT, and EED maintain a 100% duty cycle for the duration of the mission lifetime.

4.4.3 PlasmaSat/PlasmaSatEUV Concept of Operations

PlasmaSat and PlasmaSatEUVs have two operational modes: Launch & Early Oper-

ations and Science. During Launch & Early Operations, PlasmaSats and PlasmaSatEUVs fire thrusters to spin the spacecraft. After spacecraft checkout, SCM and FGM booms are deployed. The EFI wire boom antennas are then deployed over many orbits in a pair-wise fashion. PIMS and EUVCS are powered on and instrument commissioning begins. After the PlasmaSats achieve their final orbital configuration, science operations begin. All instruments maintain a 100% duty cycle for the duration of the mission lifetime.

4.4.4 Mission Design

PILOT's highly-elliptical, co-planar, near-equatorial orbits are designed to form a radio tomographic imaging plane on the apogee side (§D.1). In each of the orbits, the satellites are spaced in mean anomaly so that they bunch up near apogee to enhance tomographic resolution (Figure 3.1, §D.1). The orbits are designed to simultaneously optimize radio tomographic mapping of the inner magnetosphere, in-situ observations near the plasmasphere, and large-scale photon imaging of plasma structures. Both the inner and outer orbits have the same orbital precession rates to ensure that the area between the orbits, which defines the radio tomographic observation region, remains fixed.

The chosen precession rate is 0.81° per day for AoP and −0.41° per day in RAAN, resulting in an overall orbital precession of 0.41° per day. Combined with the orbital motion of the Earth (−0.99° per day), this results in a full orbital precession through all MLT in about 1.7 years, and ∼1.75 full MLT precessions in 3 years (Figure 4.5).

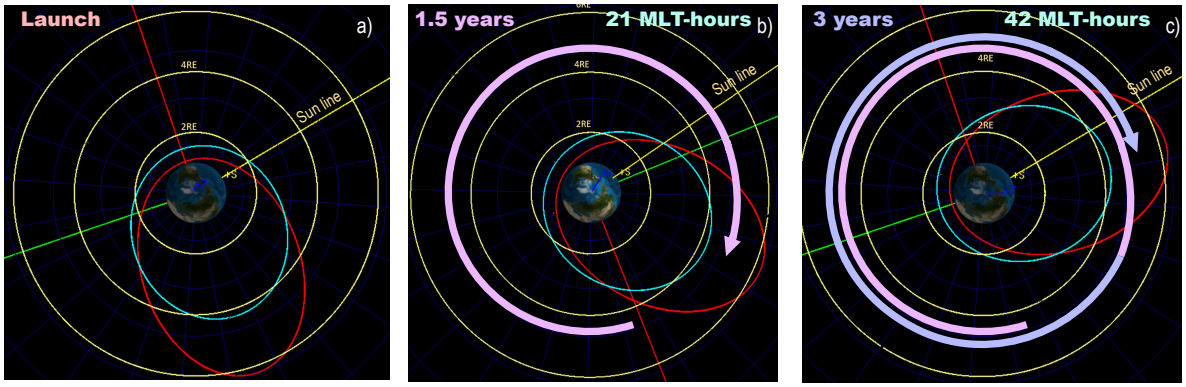

Figure 4.5: *PILOT orbits at launch (Left), at 1.5 years (Middle), and at 3 years (Right).*

4.5 Observatory Integration and Test (I&T)

PILOT I&T relies on a systematic, organized integration of well- characterized and tested instruments into the observatory payloads followed by payload level workmanship and system performance verification including acceptance testing of completed payloads and testing with the ground system. This approach draws upon I&T experience from past NASA missions and commercial manufacturers, adapted to the PILOT constellation.

I&T for the PlasmaSat and PlasmaSatEUV spacecraft draw on heritage from previous NASA heliophysics constellations such THEMIS, STEREO, Van Allen Probes, and MMS, which provide a successful roadmap for how to conduct I&T on multiple identical or nearly identical payloads. I&T for the 30 RadioSat spacecraft is modeled after successful programs

implemented by commercial constellations that fly much larger numbers of spacecraft than PILOT, such as Starlink, Planet, and Iridium.

Large-quantity instruments are built, tested and integrated in batches of five on a staggered schedule to enable a smooth production process. Any manufacturing or I&T issues are identified using the first batch of instruments. The second batch of instruments begins 2-3 months after the start of the first batch. Subsequent batches begin at intervals of 1-2 months, depending on the instrument. Additional schedule margin is included in the production of the first five flight units. This batch serves as pathfinders to reveal any I&T issues and enable them to be addressed before subsequent batches are ready for integration. In addition, all PILOT instruments have a simple interface (data and bus power) with the spacecraft bus and are integrated and tested using spacecraft-emulator Ground Support Equipment (GSE) to help early identification of issues.

RadioSat spacecraft are integrated and tested in batches of five. As with PILOT's instrument I&T philosophy, the first spacecraft is tested at full protoflight levels, and subsequent units undergoing acceptance testing only. Any single unit that fails acceptance testing is removed and diagnosed separately so production of other units can continue, unless a systematic failure is identified. While it is possible that not all failure modes are identified during I&T, the architectural redundancy inherent in PILOT's mission design allows for baseline science to be met with the loss of up to four RadioSat spacecraft (with adjustments to orbital spacing), and degraded science to be met with the loss of up to six (§2.2.2).

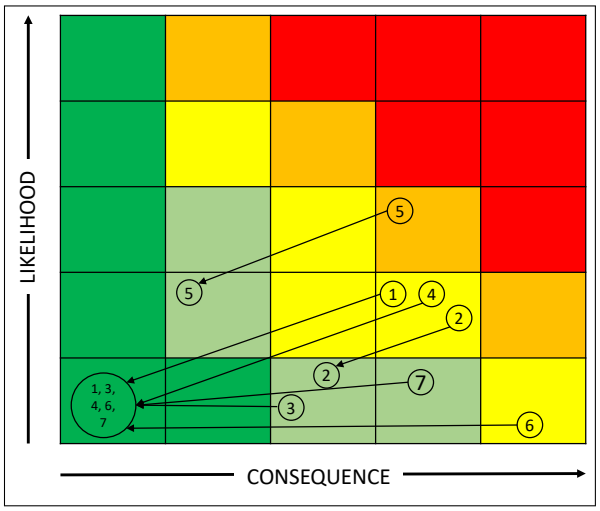

Figure 4.6: *Mission concept risk matrix, with risk trajectories before and after mitigation*

PILOT RadioSat I&T requires a spacecraft integrator equipped to handle multiple simultaneous I&T activities. Because of the rise of large commercial constellations, many microsatellite manufacturers are emerging [103]. These manufacturers, including BCT and Muon space, have configurable integration facilities for 5-10 simultaneous builds.

4.6 Ground-based Observatories

PILOT has many clear paths to engage with the ground-based space science community. Although the PILOT mission concept does not directly support ground-based facilities, or rely on ground-based observations to meet mission requirements, many natural partnerships exist that can strengthen the entire community and enhance science outcomes.

PILOT can engage the ground-based community through targeted efforts to leverage existing capabilities. These capabilities include the wide spatial coverage of ionospheric TEC measurements (e.g. [128]) which can provide maps of the ionospheric projections of large-scale cold plasma structures such as Storm Enhanced Density (SED) plumes evolving with time. Ionosphere plasma flows associated with SAPS [47] can be probed by facilities

such as Millstone Hill and SuperDARN radars [129]. Also, ground-based magnetometer arrays (accessible via the SuperMag consortium [130]) can measure magnetic perturbations from the Earthward plasma flows and ULF waves targeted by PILOT.

4.7 Risk List

#	Risk Statement	Type	L X C	Mitigation	Residual L X C
1	**Given that:** PILOT baseline science requires 30 RadioSats **There is a possibility of:** Acceptance testing does not catch all failure modes on all units **Resulting in:** a RadioSat failsure before reaching baseline mission duration	Msn	2 X 4	Can meet baseline science objectives with ≥ 26 RadioSats (14 outer, 12 inner) (§D.1). Reposition remaining spacecraft to meet minimum resolution required for science, with reduced observing duty cycle. Threshold science can be met with 24 RadioSats (13 outer, 11 inner)	1 X 1
2	**Given that:** PILOT requires 4 PlasmaSats with selective redundancy **There is a possibility of**: Radiation effects causing failure without redundant backup **Resulting in**: a PlasmaSat failure before reaching baseline mission duration	Msn	2 X 4	If one outer orbit PlasmaSat fails, observing duty cycle drops to 52%, sufficient for threshold science. If one inner orbit PlasmaSat fails, observing time duty cycles drops to 73%, sufficient for baseline science	1 X 3
3	**Given that:** Radio tomography measurements have not been made at these frequencies **There is a possibility of:** unanticipated obstacles in instrument design, **Resulting in:** cost overruns and schedule delays	Dev	1 X 3	Technique robustly demonstrated with GPS TEC measurements. Pre-Phase A technology development. Cost to implement $1.6M	1 X 1
4	**Given that:** 30 RT instruments are required for the baseline constellation **There is a possiblity of:** RT instrument delivery to RadioSat delay **Resulting in:** cost overruns and schedule delays	Dev	2 X 4	Select manufacturer with industry experience for RT instrument build	1 X 1
5	**Given that:** PILOT orbits traverse radiation belts **There is a possibility of**: Increased radiation exposure, SEEs **Resulting in:** Loss of lifetime science return	Dev	3 X 4	Implement radiation mitigation in parts selection, shielding and electronics architecture to meet baseline science	2 X 2
6	**Given that:** PILOT requires licensing of FM band frequencies **There is a possibility of**: RT transmit frequencies (50/150 MHz) being unavailable for license **Resulting in**: transmit frequency shift that requires RT instrument redesign	Dev	1 X 5	Apply for licenses early phase A. Relatively low broadcast power and large distance from Earth favorably factors into license approval. Can shift frequencies to comply with available licensing by ≤ 25 MHz (§C.1) with minimal impact to science, cost and schedule	1 X 1
7	**Given that:** Multiple RadioSats (≤ 6) can be lost on orbit **There is a prossiblity of**: requiring propulsion to modify orbit to re-establish baseline science resolution **Resulting in**: inadequate propulsion for mission life and deorbit	Msn	1 X 4	Allocated 5 m/s delta-V for constellation redistribution in addition to worst case orbit insertion, station keeping and deorbit delta-V. Additionally include 25% mission delta-V propellant margin	1 X 1

Table 4.7: *PILOT baseline risks include a robust mitigation strategy that lowers risk ratings to acceptable levels*

Risks identified during the PILOT study are listed in Table 4.7. Mitigations are presented with resultant Likelihood and Consequence (L X C). Figure 4.6 shows each risk before and after mitigation.

5 Development Schedule and Schedule Constraints

5.1 High-Level Mission Schedule

A high-level Phase A through Phase F schedule highlighting the key design reviews and the length of each phase is shown in Table 5.1. A detailed schedule of instrument and spacecraft development, and system integration and test is shown in Figure 5.1.

Phase	Phase A		Phase B		Phase C			Phase D				Phase E	Phase F
Duration	18 months		12 months		30 Months			24 Months				36 Months	12 Months
Start	Oct-24		Apr-26		Apr-27			Oct-29				Oct-31	Oct-34
End	Apr-26		Apr-27		Oct-29			Oct-31				Oct-34	Oct-35
Activity	*SRR/MDR*	*KDP-B*	*MPDR*	*KDP-C*	*MCDR*	*SIR*	*KDP-D*	*ORR*	*LRR*	*Launch 1*	*Launch 2*	-	-
Date	*Dec-25*	*Apr-26*	*Nov-26*	*Apr-27*	*Jul-28*	*Sep-29*	*Oct-29*	*Oct-30*	*Aug-31*	*Sep-31*	*Nov-31*	-	-

Table 5.1: *Top-level mission schedule*

5.2 Science, Technology Development Plans

PILOT spacecraft bus technologies have extensive flight heritage. TRL advancement of PILOT instrument components can start in Phase A and reach TRL 6 by PDR (Table 5.2). Prior to Phase A, the RT instrument is brought to TRL 6 via a separately-funded development program. The steps required for space qualification and alternatives are described in §G.6.

Development Target	**System Component**	**Start TRL**	**TRL Advancement**	**Duration**	**Fallbacks/ Alternatives**	**Cost**	**Funding Source**
Radio Tomography	Transmitter/ Receiver / Capacitive Power Board	4	Demonstrate RT prototype in relevant environment	3 years	None	$1.6M	Pre-phase A technology development
EUVCS	Camera Sensor	5	Verify new filters and mirrors for improved camera operation	11 months	Utilize IMAGE filter and mirrors with sub-optimal performance or build with filters and mirrors not fully tested and characterized	$4M	PILOT mission Phase A
PIMS Sensor Panel Bias/Bias Box	Bias Plate	5	Verify SPB and Bias Box performance	8 months	Utilize HOPE SPB design without changes leading to suboptimal performance or build with a SPB not fully tested and characterized	$250K	PILOT mission Phase A

Table 5.2: *Technology development plans*

5.3 Development Schedule and Constraints

A notional PILOT schedule is shown in Table 5.1. Phase A includes development for the EUVCS and SPB (§G.6). Pre-Phase A technology development brings the RT instru-

ment to TRL 6, and is not included in this schedule. EUVCS and PIMS/SPB technology maturation is completed in Phase A. Phase B is 12 months and includes the Preliminary Design Review, by which time all technologies are at TRL 6. Phase C is 30 months and concludes with all instruments and most spacecraft fabricated, tested, and ready for mission integration. Phase D lasts 24 months and includes system integration, test, and launch site activities. Phase E begins 30 days after the first launch and lasting 36 months. This is followed by a 12-month Phase F, during which outer-orbit spacecraft are deorbited and inner-orbit spacecraft are placed into a graveyard orbit. There are no launch restrictions, and minimal impacts of a launch slip. PILOT has no required launch windows.

The PILOT mission schedule outlines all phases of the project. The schedule is consistent with program lifecycle recommendations in the NASA Schedule Management Handbook NASA/SP-2010-3403. High-heritage subsystems and instruments result in a low-risk development schedule with low likelihood of development delays. Long-lead items and bulk buys for RadioSat instruments and spacecraft, as well as development of EMs for low-TRL instruments, occur in early Phase B. For RadioSat I&T, units not passing acceptance tests are taken out of the manufacturing flow and analyzed outside of production, allowing other units to be qualified.

6 Mission Life-Cycle Cost

6.1 Costing Methodology and Basis of Estimate

The PILOT mission Phase A-F total cost is $1.74B in FY2022 dollars, and $2.28B in real-year dollars, which includes 30% reserve. Excluding LV costs, the PILOT Phase A–F mission cost is $1.26B FY22$ (see Table 6.1). Cost was estimated at Work Breakdown Structure (WBS) level 2 or 3, as appropriate. The payload and spacecraft estimates capture the resources required for a notional point design and were modeled in conjunction with the Cost Estimating, Modeling, and Analysis (CEMA) office at GSFC using standard cost modeling tools: NICM for instrument costs and PCEC for spacecraft costs at 50% confidence levels. Estimates for Science, Mission Operations, and Ground System elements are grassroots estimates based on actuals for these WBS elements phased according to the PILOT mission schedule, and validated with cost modeling. The result is a mission estimate that is representative of expenditures that might be expected to execute the PILOT mission concept. Cost modeling for instruments and spacecraft, and system integration and test was conducted for units of five for large-quantity instruments and spacecraft and single units for those with smaller quantities. Further details concerning cost modeling methodology and the assumptions underlying it can be made available upon request.

Separately-funded pre-Phase A technology development of the RT instrument requires three years and $1.6M (FY2022$) The Phase A cost is $13.28M (FY2022$). Phase A is 18 months in duration and includes technology maturation for EUVCS and PIMS/SPB.

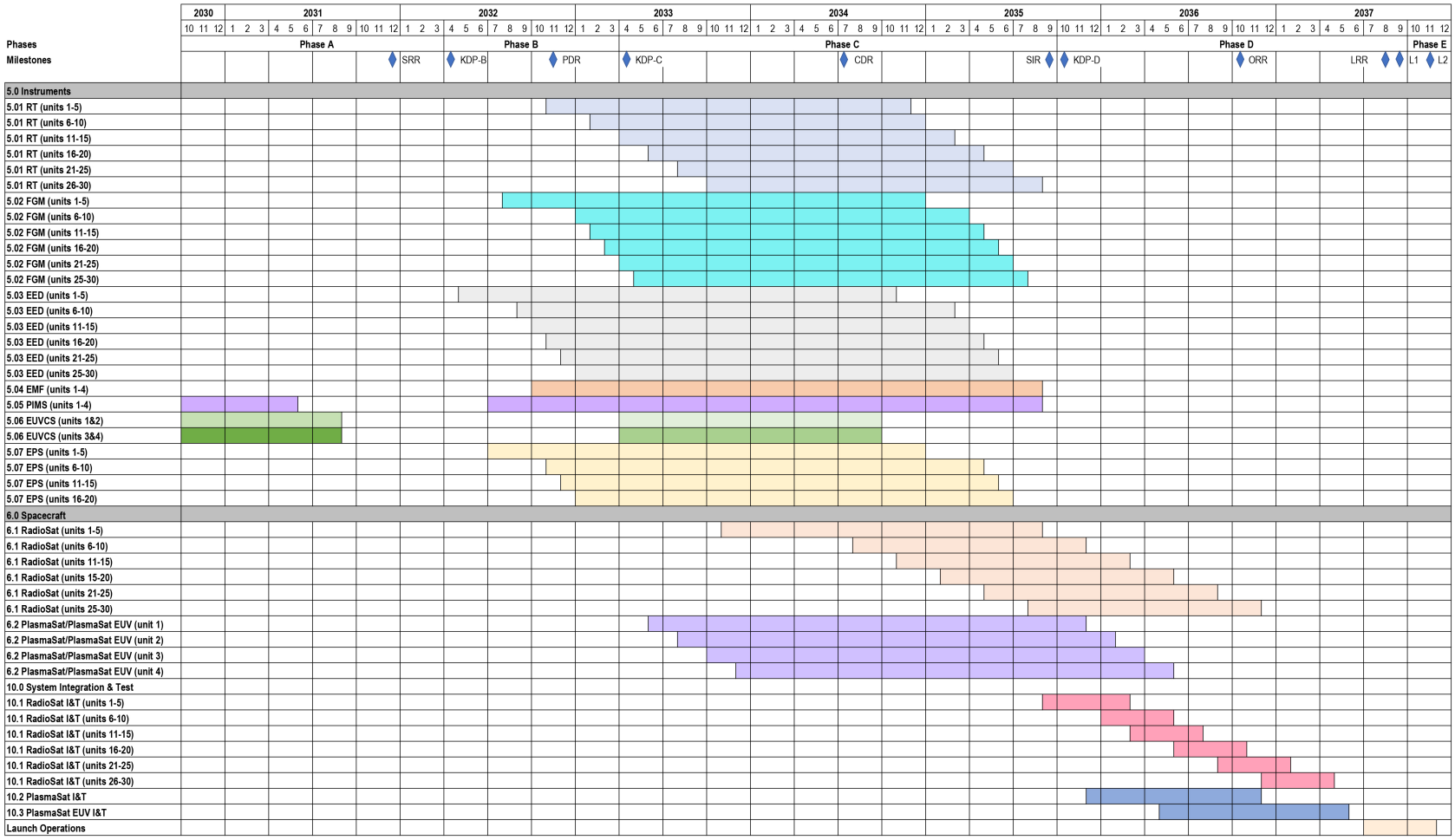

Figure 5.1: *PILOT notional development schedule*

WBS #	Description	Prior (not included in total)	2031	2032	2033	2034	2035	2036	2037	2038	2039	2040	2041	2042	Total
1, 2, 3	PM, SE, SMA		$ 2.34	$ 6.12	$ 12.28	$ 14.19	$ 14.17	$ 14.00	$ 11.93	$ 1.43	$ 1.13	$ 0.74	$ 0.01	$ -	$ 78.35
4	Science		$ 0.21	$ 2.40	$ 4.40	$ 9.42	$ 5.48	$ 15.71	$ 18.45	$ 18.83	$ 16.59	$ 16.40	$ 1.40		$ 109.30
5	**Payload**		**$ 1.06**	**$ 3.19**	**$ 18.98**	**$ 109.28**	**$ 122.97**	**$ 36.04**	**$ -**	**$ -**	**$ -**	**$ -**	**$ -**	**$ -**	**$ 291.52**
5.01	RT	$1.60	$ -	$ -	$ 2.85	$ 24.19	$ 35.58	$ 11.39	$ -	$ -	$ -	$ -	$ -	$ -	$ 74.01
5.02	FGM		$ -	$ -	$ 4.13	$ 10.82	$ 10.82	$ 7.85	$ -	$ -	$ -	$ -	$ -	$ -	$ 33.61
5.03	EED		$ -	$ -	$ 3.30	$ 4.30	$ 4.30	$ 3.50	$ -	$ -	$ -	$ -	$ -	$ -	$ 15.41
5.04	EMF		$ -	$ -	$ 1.90	$ 13.50	$ 13.50	$ 1.90	$ -	$ -	$ -	$ -	$ -	$ -	$ 30.81
5.05	PIMS		$ 0.06	$ 0.19	$ 3.05	$ 16.19	$ 18.50	$ 7.66	$ -	$ -	$ -	$ -	$ -	$ -	$ 45.66
5.06	EUVCS		$ 1.00	$ 3.00	$ -	$ 32.72	$ 32.72	$ -	$ -	$ -	$ -	$ -	$ -	$ -	$ 69.44
5.07	EPS		$ -	$ -	$ 3.74	$ 7.55	$ 7.55	$ 3.74	$ -	$ -	$ -	$ -	$ -	$ -	$ 22.58
6	**Spacecraft**		**$ -**	**$ -**	**$ -**	**$ 21.89**	**$ 91.02**	**$ 174.38**	**$ 74.02**	**$ -**	**$ -**	**$ -**	**$ -**	**$ -**	**$ 361.32**
6.01	RadioSat		$ -	$ -	$ -	$ 5.58	$ 44.95	$ 128.31	$ 63.47	$ -	$ -	$ -	$ -	$ -	$ 242.32
6.02	PlasmaSat		$ -	$ -	$ -	$ 16.31	$ 46.07	$ 46.07	$ 10.55	$ -	$ -	$ -	$ -	$ -	$ 119.00
7	Mission Operations		$ 0.28	$ 0.58	$ 1.98	$ 17.04	$ 3.99	$ 4.99	$ 9.50	$ 9.31	$ 8.02	$ 2.58	$ 0.37	$ 0.20	$ 58.84
8	Launch		$ -	$ -	$ -	$ -	$ -	$ -	$ 480.00	$ -	$ -	$ -	$ -	$ -	$ 480.00
9	Ground System		$ 0.01	$ 0.20	$ 1.34	$ 3.03	$ 2.12	$ 2.31	$ 14.00	$ 14.28	$ 9.51	$ 0.83	$ 0.15	$ -	$ 47.77
10	System I&T		$ 0.03	$ 0.06	$ 0.02	$ 0.02	$ 4.58	$ 18.43	$ 0.51	$ 0.00	$ -				$ 23.65
	Total (before reserve)		$ 3.93	$ 12.56	$ 39.00	$ 174.87	$ 244.33	$ 265.87	$ 608.42	$ 43.84	$ 35.26	$ 20.55	$ 1.93	$ 0.20	$ 1,450.75
	Reserves (30%)		$ 1.18	$ 3.77	$ 11.70	$ 52.46	$ 73.30	$ 79.76	$ 38.52	$ 13.15	$ 10.58	$ 6.17	$ 0.58	$ 0.06	$ 291.22
	Total (FY2022$)		**$ 5.11**	**$ 16.32**	**$ 50.70**	**$ 227.33**	**$ 317.62**	**$ 345.63**	**$ 646.94**	**$ 56.99**	**$ 45.83**	**$ 26.72**	**$ 2.51**	**$ 0.26**	**$ 1,741.97**

WBS #	Description	Prior (not included in total)	2031	2032	2033	2034	2035	2036	2037	2038	2039	2040	2041	2042	Total
1, 2, 3	PM, SE, SMA		$ 2.95	$ 7.91	$ 16.28	$ 19.32	$ 19.82	$ 20.10	$ 17.13	$ 2.17	$ 1.76	$ 1.18	$ 0.02	$ -	$ 108.66
4	Science		$ 0.27	$ 3.10	$ 5.84	$ 12.82	$ 7.66	$ 22.57	$ 27.22	$ 28.52	$ 25.82	$ 26.21	$ 2.30	$ -	$ 162.33
5	**Payload**		**$ 1.34**	**$ 4.12**	**$ 25.17**	**$ 148.82**	**$ 171.98**	**$ 51.77**	**$ -**	**$ -**	**$ -**	**$ -**	**$ -**	**$ -**	**$ 403.20**
5.01	RT	$ 1.96	$ -	$ -	$ 3.78	$ 32.95	$ 49.76	$ 16.36	$ -	$ -	$ -	$ -	$ -	$ -	$ 102.85
5.02	FGM		$ -	$ -	$ 5.48	$ 14.73	$ 15.13	$ 11.27	$ -	$ -	$ -	$ -	$ -	$ -	$ 46.61
5.03	EED		$ -	$ -	$ 4.38	$ 5.86	$ 6.02	$ 5.03	$ -	$ -	$ -	$ -	$ -	$ -	$ 21.29
5.04	EMF		$ -	$ -	$ 2.52	$ 18.39	$ 18.88	$ 2.73	$ -	$ -	$ -	$ -	$ -	$ -	$ 42.53
5.05	PIMS		$ 0.08	$ 0.24	$ 4.05	$ 22.05	$ 25.87	$ 11.01	$ -	$ -	$ -	$ -	$ -	$ -	$ 63.30
5.06	EUVCS		$ 1.26	$ 3.87	$ -	$ 44.56	$ 45.76	$ -	$ -	$ -	$ -	$ -	$ -	$ -	$ 95.46
5.07	EPS		$ -	$ -	$ 4.96	$ 10.28	$ 10.56	$ 5.37	$ -	$ -	$ -	$ -	$ -	$ -	$ 31.17
6	**Spacecraft**		**$ -**	**$ -**	**$ -**	**$ 29.81**	**$ 127.30**	**$ 250.48**	**$ 109.20**	**$ -**	**$ -**	**$ -**	**$ -**	**$ -**	**$ 516.80**
6.01	RadioSat		$ -	$ -	$ -	$ 7.60	$ 62.87	$ 184.31	$ 93.64	$ -	$ -	$ -	$ -	$ -	$ 348.41
6.02	PlasmaSat		$ -	$ -	$ -	$ 22.21	$ 64.44	$ 66.18	$ 15.56	$ -	$ -	$ -	$ -	$ -	$ 168.39
7	Mission Operations		$ 0.35	$ 0.75	$ 2.63	$ 23.21	$ 5.59	$ 7.17	$ 14.01	$ 14.10	$ 12.47	$ 4.13	$ 0.60	$ 0.34	$ 85.34
8	Launch		$ -	$ -	$ -	$ -	$ -	$ -	$ 480.00	$ -	$ -	$ -	$ -	$ -	$ 480.00
9	Ground System		$ 0.01	$ 0.25	$ 1.78	$ 4.13	$ 2.96	$ 3.32	$ 20.66	$ 21.63	$ 14.80	$ 1.33	$ 0.25	$ -	$ 71.10
10	System I&T		$ 0.04	$ 0.08	$ 0.02	$ 0.02	$ 6.40	$ 26.48	$ 0.75	$ 0.00	$ -				$ 33.80
	Total (before reserve)		$ 4.95	$ 16.21	$ 51.72	$ 238.14	$ 341.72	$ 381.89	$ 668.98	$ 66.42	$ 54.86	$ 32.84	$ 3.17	$ 0.34	$ 1,861.24
	Reserves (30%)		$ 3.37	$ 4.86	$ 15.52	$ 71.44	$ 102.52	$ 114.57	$ 56.69	$ 19.93	$ 16.46	$ 9.85	$ 0.95	$ 0.10	$ 416.26
	Total (Real Year)		**$ 8.31**	**$ 21.08**	**$ 67.23**	**$ 309.59**	**$ 444.24**	**$ 496.46**	**$ 725.67**	**$ 86.34**	**$ 71.31**	**$ 42.70**	**$ 4.12**	**$ 0.44**	**$ 2,277.49**

Figure 6.1: *PILOT cost estimate in FY2022$ (top) and RY$ (bottom)*

A Acronyms

Acronym	Full Expression
AC	Alternating Current
AIAA	American Institute of Aeronautics and Astronautics
AMPERE	Active Magnetosphere and Planetary Electrodynamics Response Experiment
AoP	Argument of Perigee
APPS	Active and Passive Plasma Sounder
AWS	Amazon Web Services
BARREL	Balloon Array for Radiation-belt Relativistic Electron Losses
BB	Bias Box
BBF	Bursty Bulk Flows
BCT	Blue Canyon Technologies
BOE	Basis of Estimate
BOL	Beginning of Life
C&DH	Command and Data Handling
CAN	Controller Area Network
CASSIOPE	Cascade, Smallsat and Ionospheric Polar Explorer
CBE	Current Best Estimate
CEMA	Cost Estimating, Modeling, and Analysis
CMD	Command
CML	Concept Maturity Level
CONOPS	Concept of Operations
COSMIC-2	Constellation Observing System for Meteorology, Ionosphere, and Climate-2
COTS	Commercial-Off-The-Shelf
CPIC	Curvilinear Particle-In-Cell
CRRES	Combined Release and Radiation Effects Satellite
CSS	Coarse Sun Sensor
CT	Computerized Tomography
CU	University of Colorado
DAPPER	Dual-Amplifier with Pulse Processing and Energy Readout
DC	Direct Current
DCB	Data Controller Board
DD	Displacement Damage
DDOR	Delta Doppler One-way Ranging
DE	Dynamics Explorer
DFB	Digital Fields Board
DFW	Digital Fields Waves

DLSR	Deep Learning-based Super Resolution
DOD	Depth of Discharge
DSS	Digital Sun Sensors
DTV	Dynamic Test Vehicle
e-POP	Enhanced Polar Outflow Probe
EDAC	Error Detection and Correction
EED	Energetic Electron Detector
EELV	Evolved Expendable Launch Vehicle
EFI	Electric Field Instrument
EFW	Electric Fields and Waves
EM	Engineering Model
EMF	Electromagnetic Fields
EMFISIS	Electric and Magnetic Field Instrument Suite and Integrated Science
EMIC	Electromagnetic Ion Cyclotron
EOL	End of Life
EOM	End of Mission
EPS	Energetic Particle Sensor
EPS	Electrical Power System
ESA	Electrostatic Analyzer
ESPA	EELV Secondary Payload Adapter
EUV	Extreme Ultraviolet
EUVCS	Extreme Ultraviolet Camera System
eV	Electron Volt
EXOport	Launch vehicle adapter
FEEPS	Fly's Eye Energetic Particle Sensor
FGM	Fluxgate Magnetometer
FOV	Field Of View
FPGA	Field Programmable Gate Array
GEO	Geostationary Earth Orbit
GOLD	Goddard Open Learning Design
GPIM	Green Propellant Infusion Mission
GPS	Global Positioning System
GSE	Ground Support Equipment
GSM	Geocentric Solar Magnetospheric
GTO	Geostationary Transfer Orbit
HOPE	Helium, Oxygen, Proton, and Electron
HQ	Headquarters
HV	High Voltage
HVPS	High Voltage Power Supply
I&T	Integration and Test

IDL	Interactive Data Language
IMAGE	Imager for Magnetopause-to-Aurora Global Exploration
IMU	Interial Measurement Unit
IPE	Ionosphere Plasmasphere Electrodynamics
IT	Ionosphere Thermosphere
IVM	Ion Velcity Meter
KDP	Key Decision Point
LASP	Laboratory for Atmospheric and Space Physics
LEO	Low Earth Orbit
LLC	Limited Liability Corporation
LLNL	Lawrence Livermore National Laboratory
LPW	Langmuir Probe and Waves
LRR	Launch Readiness Review
LV	Launch Vehicle
LVPS	Low Voltage Power Supply
MagEIS	Magnetic Electron Ion Spectrometer
MAVEN	Mars Atmosphere and Volatile Evolution
MCDR	Mission Critical Design Review
MCP	Micro Channel Plate
MDR	Mission Design Review
MEU	Mass spectrometer Electronics Unit
MEV	Maximum Expected Value
MIDEX	Medium Explorer
ML	Multi-Layer
ML	Machine Learning
MLAT	Magnetic Latitude
MLI	Multi-Layer Insulation
MLT	Magnetic Local Time
MMS	Magnetospheric Multiscale
MOC	Mission Operations Center
MPDR	Mission Preliminary Design Review
MTM	Mission Traceability Matrix
NASA	National Aeronautics and Space Administration
NICM	NASA Instrument Cost Model
NLS	NASA Launch Services
NOAA	National Oceanic and Atmospheric Administration
NORAD	North American Aerospace Defense Command
NVR	Non-Volatile Residues
Ob	Objective
ORR	Operational Readiness Review

PAD	Pitch Angle Distribution
PB	Physics Based
PBI	Power and Bus Interface Board
PCEC	Project Cost Estimating Capability
PILOT	Plasma Imaging LOcal and Tomographic experiment
PIMS	Plasmasphere Ion Mass Spectrometer
PySPEDAS	Python Space Physics Environment Data Analysis Software
RAAN	Right Ascension of the Ascending Node
RAM-SCB	Ring current-Atmosphere interaction Model and Self-Consistent Magnetic Field
REMS	Relativistic Electron Magnetic Spectrometer
RF	Radio Frequency
RIMS	Retarding Ion Mass Spectometer
RMS	Root Mean Squared
RPM	Revolutions Per Minute
RT	Radio Tomography
RWA	Reaction Wheel Assembly
S/N	Signal-to-Noise
S&MA	Safety and Mission Assurance
SAID	Subauroral Ion Drifts
SAPS	Subauroral Polarization Streams
SBC	Single Board Computer
SCM	Search Coil Magnetometer
SDC	Science Data Center
SED	Storm Enhanced Density
SEE	Single Event Effect
SEL	Single Event Latchup
SEU	Single Event Upset
SHIELDOSE	Computer Code for Space-Shielding Radiation Dose Calculations
SIR	System Integration Review
SPB	Sensor Panel Bias
SPDF	Space Physics Data Facility
SPEDAS	Space Physics Environment Data Analysis Software
SPENVIS	SPace ENVironment Information System
SQ	Science Question
SRR	System Requirements Review
SRU	Stellar Reference Unit
SSL	Space Sciences Laboratory
ST	Space Technology
STD	Standard

STEREO	Solar Terrestrial Relations Observatory
STM	Science Traceability Matrix
STP	Solar Terrestrial Probe
STPSat	Space Test Program Satellite
SuperDARN	Super Dual Auroral Radar Network
SwRI	Southwest Research Institute
TEC	Total Electron Content
THEMIS	Time History of Events and Macroscale Interactions during Substorms
TID	Total Ionizing Dose
TLM	Telemetry
TMP	Technology Maturation Plan
TOF	Time of Flight
TREO	Tomographic Refilling and Erosion Observatory
TRL	Technology Readiness Level
TTPC	Time-Tagged Photon Count
UCLA	University of California Los Angeles
ULF	Ultra Low Frequency
USTEC	United States Total Electron Content
UVS	Ultraviolet Imager/Spectrograph
VLF	Very Low Frequency
WBS	Work Breakdown Structure
WHISPER	Waves of High Frequency and Sounder for Probing of Electron Density by Relaxation Experiment
μCPT	Micro Charged Particle Telescope

B Design Team Personnel

Name	Role	Institution
David Malaspina	PI, Science Team	University of Colorado, LASP
Laila Andersson	Science Team	University of Colorado, LASP
Xiangning Chu	Science Team	University of Colorado, LASP
Robert Ergun	Co-I, Science Team	University of Colorado, LASP
Naomi Maruyama	Science Team	University of Colorado, LASP
Scott Thaller	Science Team	University of Colorado, LASP
Joseph Borovsky	Science Team	Space Science Institute
Dennis Gallagher	Science Team	NASA Marshall Space Flight Center
Jerry Goldstein	Co-I, Science Team	Southwest Research Institute
Vania Jordanova	Science Team	Los Alamos National Laboratory
Solène Lejosne	Science Team	University of California, Berkeley, SSL
James McFadden	Science Team	University of California, Berkeley, SSL
Brian Walsh	Science Team	Boston University

Table B.1: *PILOT Mission Concept Science Team*

Name	Role	Institution
Diane Brening	Electrical Engineering	University of Colorado, LASP
Maxwell Fowle	Mechanical Engineering	University of Colorado, LASP
Jerry Jason	Mission Operations	University of Colorado, LASP
Jason Link	Instrument Systems Engineering	University of Colorado, LASP
Thomas Sparn	Cost Analysis	University of Colorado, LASP
Constance Spittler	Concept Study Management, Mission Systems Engineering	University of Colorado, LASP
Bryce Unruh	Mission Systems Engineering	University of Colorado, LASP
Lauren De Moudt	Orbital Dynamics Design	Advanced Space LLC
Jeffrey Parker	Co-I, Orbital Dynamics Design	Advanced Space LLC

Table B.2: *PILOT Mission Concept Engineering Team*

Industrial Team	Discussion Topic
Aerojet Rocketdyne	RadioSat Propulsion System
Aerospace Corporation	Particle Detector Implementation
Amazon Web Services	Ground Communication Systems
Ball Aerospace	PlasmaSat Design
Blue Canyon Technologies	RadioSat Design
Blue Origin	Launch Vehicle Performance
Exolaunch GmbH	Spacecraft Deployment
Microchip Technology Inc.	Chip-scale Atomic Clock Technology
Muon Space	RadioSat Design
SpaceX	Launch Vehicle Performance

Table B.3: *Industrial Teams Consulted During the PILOT Mission Concept Study*

C PILOT Instrumentation Detail

All PILOT instruments, with the exception of RT and EUVCS, have measurement requirements that are met by existing flight instrumentation with TRL > 6 (Table 3.3).

Each PILOT instrument or suite operates and collects data independently of the other instruments or suites. Each instrument or suite performs its own regulation of bus voltage power, monitors instrument health, accepts commands from spacecraft command and data handling (C&DH) software and sends science and housekeeping data to the spacecraft C&DH memory for storage and transmission to the ground. This 'independent instrument' approach simplifies instrument I&T, as well as integration with the spacecraft by allowing each instrument or suite to be tested alone or in batches as stand-alone units.

C.1 RadioSat RT Instrument

The Radio Tomography **RT** instrument baselined for the PILOT mission concept consists of two subsystems: Radio Frequency (RF) and Active and Passive Plasma Sounder (APPS), both of which share the same dipole pair of axially-deployed 1.5-m stacer antennas for transmitting and receiving signals.

C.1.1 RadioSat RT RF

Radio tomography (§D.1) combines well-established radio science techniques and computerized tomography (CT) to form rapidly refreshing images of electron density, essentially creating a motion picture of cold plasma in the inner magnetosphere.

The density image spatial and temporal resolution required by PILOT science (Table STM-2) are readily achieved with the PILOT RT RF concept (§D.1). The core of radio tomography imaging is to measure TEC, using the measured phase shift between two radio signals, along a large set of lines-of-sight. As is done in CT medical imaging, the network of TEC measurements are then inverted to form an image of electron density. The PILOT CT inversion is described in §D.1.

C.1.1.1 Design constraints

To measure electron density in the inner magnetosphere, the RT RF must transmit and receive a pair of discrete-frequency radio signals to measure TEC in the range of $\sim 3{\times}^{12}$ m^{-2} to $\sim 3{\times}^{17}$ m^{-2}. The ability to make this TEC measurement is limited by a combination of the signal-to-noise ratio (S/N) of the radio signals and the expected phase advance or group delay.

Achieving this TEC measurement requires defining low (f_L) and high (f_H) signal frequencies (§D.1). The choice of frequency involves: (a) Selecting a sufficiently low f_L so that group delays and phase advances are measurable with good S/N in the expected TEC range. (b) Selecting a sufficiently high f_L to avoid 2nd order effects such as scintillation, refraction, reflection, Faraday rotation, and absorption. (c) Selecting a frequency so that a transmitter and receiver can be implemented on a microsat.

The above criteria (a) and (b) are optimized for PILOT with $f_L \approx 50$ MHz for the probing frequency and $f_H = 150$ MHz for the reference frequency. While less optimal, other 1st and 3rd harmonic pairs with f_L between 25 MHz and 100 MHz can be acceptable for PILOT. With $f_L = 50$ MHz, a dipole antenna system with opposing 1.5 m (1/4 wavelength)

antennas can be used to transmit and receive, which satisfies (c). A lower frequency for f_L requires longer antennas. A system with $f_L >\sim 100$ MHz may be possible using a phase-array antenna system. Such high frequency, however, requires very high phase accuracy (see below) and therefore a significantly more complex instrument (§G.1).

One issue with the required frequency range is obtaining licensed frequency bands. In addition to satisfying radio signal regulatory requirements, a licensed band would best avoid interference from surface radio transmissions. While such interference could be avoided with very narrow-band transmissions and high transmission power, a licensed band would be more effective at reducing risk and simplifying instrument design.

Assuming $f_L = 50$ MHz and $f_H = 150$ MHz, a tuned, half-wave dipole transmitter/receiver with two, ∼1.5-m stacer antennas normal to the orbital plane is realizable for PILOT. The third harmonic can be simultaneously tuned with the fundamental frequency using the same antenna. A "square wave" or digital driver automatically produces both the 1st and 3rd harmonic. The dipole antenna transmission pattern covers all points along the orbit at all times. Also, stacer antennas have a long spaceflight heritage (e.g., [111, 114, 131]), and 1.5 m stacers can be easily accommodated on a microsat bus.

The power required for RF signal transmission is primarily driven by the required accuracy of individual TEC measurements. TEC measurement accuracy required to reproduce plasma structures is ∼2% [104]. Since the plasmasphere often has a sharp density gradient at the plasmapause, the scientific requirements for imaging are slightly more stringent and call for ∼1% TEC accuracy in densities between 10 cm^{-3} and 100 cm^{-3} near the gradient (empirically tested using output from the IPE model plasmasphere simulations [132]). The most demanding accuracy requirement on an individual TEC measurement is for the longest ray path length (6 R_E) through the lowest average density, set at 10 $cm^{-}3$ (TEC $= 2.55 \times 10^{14}$ m^{-2}; see black dashed line in Figure D.1c). The signal strength decreases with spacecraft separation distance squared (d^2), overcoming the linear increase in TEC (proportional to d).

Densities near the outer part of the outer orbit can be as low as 0.5 cm^{-3} with ray path lengths up to 4 R_E (see magenta dashed line in Figure D.1c). The accuracy requirement in such low densities is less stringent, since small perturbations of small densities are not scientifically required to be imaged. A 10% TEC accuracy is sufficient to identify a large ($> 10\%$) perturbation at the outer-most part of the image plane. Given a density of 0.5 cm^{-3} and a path length of 4 R_E, the TEC is 1.3×10^{13} m^{-2}. Therefore, measuring TEC $= 1.3 \times 10^{13}$ m^{-2} with 10% accuracy at a distance of 4 R_E sets a second minimum accuracy requirement.

Because TEC is determined from the relative phase shift between two radio signals (§D.1), the accuracy of an individual TEC measurement depends on phase measurement accuracy, which is approximately $(S/N)^{-1}$ radians for a narrow band signal sustained over a period of several inverse bandwidths. For PILOT, a 100 Hz bandwidth signal that endures for 0.1 s (10 inverse bandwidths) meets this requirement.

To estimate the transmitter power needed, Equation 5 (in §D.1) can be reversed to determine the time delay between the two signals:

$$\delta t_{\phi HL} = \frac{C}{4\pi^2}\frac{f_H^2 - f_L^2}{f_L^2\ f_H^2}T_{EC} = 12.1\ ns\ (Case\ 1) \tag{1}$$

$$\delta t_{\phi HL} = \frac{C}{4\pi^2}\frac{f_H^2 - f_L^2}{f_L^2\ f_H^2}T_{EC} = 0.62\ ns\ (Case\ 2) \tag{2}$$

The expected phase delay for the first case is 3.8 rad (218^o) and, for the second case is 0.19 rad ($\sim 11^o$). For Case 1, a S/N of 28 dB is required for 1% accuracy at 6 R_E. For Case 2, an S/N ratio of ~34 dB is required for 10% accuracy at 4 R_E. The two cases place nearly equal requirements on transmitted power with Case 1 being marginally more stringent.

Using a noise floor of 10^{-18} W m^{-2} Hz^{-1} (achieved on NASA's Wind spacecraft), 100 Hz bandwidth, and assuming no interference from terrestrial radio sources, 25 W of transmitted power at the fundamental yields ~28 dB S/N at a distance of 6 R_E and achieves the worst-case TEC measurement at 1% accuracy for average densities of 10 cm^{-3}.

This demonstrates the importance of using narrow band signals in licensed frequency bands. Interference from radio transmissions from Earth's surface can increase the noise by up to 30 dB, which would, in turn, force significantly higher RF transmitter power, or a system designed around a quiet, narrow-band carrier range.

C.1.1.2 RF Instrument Design

Figure C.1 shows a block diagram of a notional RF transmitter and receiver using a half-wave dipole. The antennas are best mounted normal to the orbital plane, $\pm 10^o$, to avoid significant radiation pattern signal loss. To achieve ~ 25 W RMS power for each of the signal pair, the antennas must be driven oppositely with a +200 V signal pair (1st and 3rd harmonic) resulting in ~ 1 A of peak current to each antenna. Technology for such transmission is well understood.

The notional instrument design (Figure C.1) uses a 20:1 inductive stepper demanding a +10 V, 20 A power source. This voltage range allows for use of solid-state electronics to deliver power for transmission. Due to resistive losses and other system losses, both pairs of radio signals may require up to ~200 W of surge power. Since the transmitting duty cycle is 0.1 s every ~10 s, the average power is ~3 W (when considering conversion and other losses). The power system design must withstand a very large number (12 million cycles in 3 years) of 0.1 second, 20 A surges from a source with a minimum of 20 V.

In an earlier effort [104], a 60 J, 28 V capacitor bank was proposed for the surge power supply (Figure C.1). This capacitor bank requires ~0.15 F at 28 V (estimated mass of ~1 kg). During transmission, the capacitor bank discharges to ~22.5 V delivering 20 J of energy. The capacitor bank is then recharged directly from a standard 28 V power system over the subsequent ~9.5 s. This system requires investigation and qualification, in particular for thermal properties. Investigation into alternative approaches such as a dedicated lithium battery bank is suggested.

Since the antennas are tuned, and each RadioSat transmits at separate times, the RT RF receiver electronics can use the same antennas to transmit and receive radio signals. The use of the antenna for transmission and receiving is best accomplished using a mechanical relay, since a highly-sensitive receiver may not withstand the 200 V transmission. Either

qualifying such a relay for 12 million cycles or developing solid-state isolation is required. All other aspects of the receiver and phase detection portions of the RT RF instrument are well-understood and can be readily developed.

Radio frequency transmission and receiving technologies for space applications are well-established and well-understood, so successful development is realizable. The primary areas of investigation are (1) need for licensed frequency bands, (2) developing a power system to deliver 200 W surges for 0.1 s every ∼10 s for the planned duration of the PILOT mission, and (3) investigating methods that enable the use of the same antennas for transmitting and receiving. These challenges are entirely solvable with existing technologies, allowing for a TRL 6 development prior to the start of the PILOT mission. §G.6 details a technology development plan for an RT RF instrument to reach TRL 6.

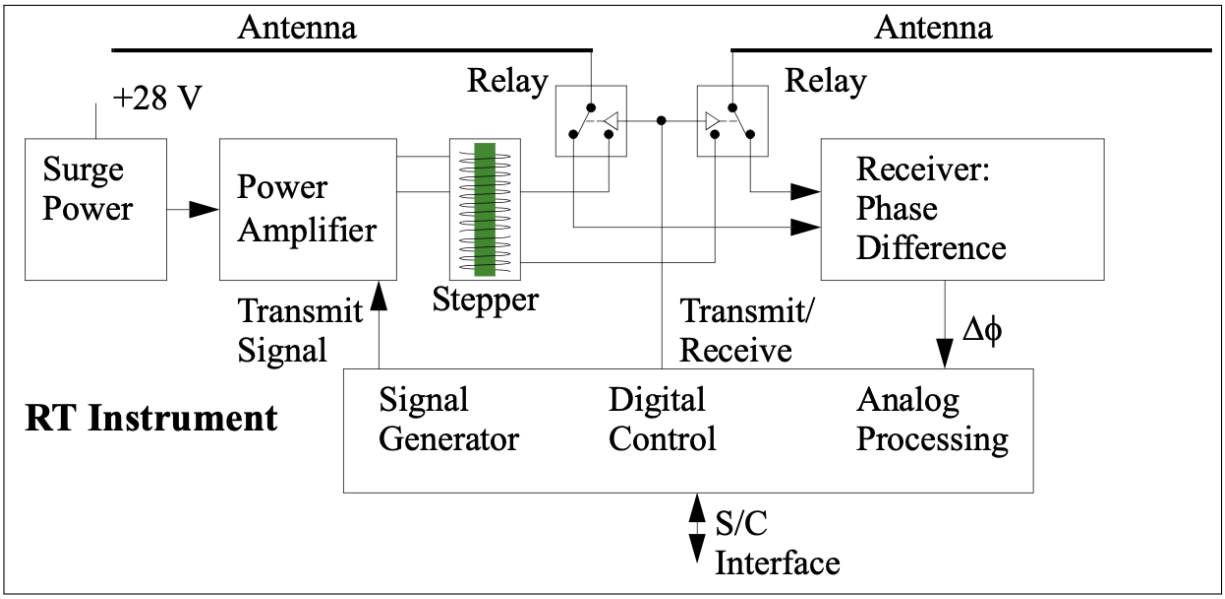

Figure C.1: *A block diagram of an RT RF instrument.*

C.1.2 RadioSat RT APPS

Accurate in-situ plasma density measurements at each RadioSat provide important constraints on radio tomographic inversion solutions (§D.1.2), therefore these measurements are important to all science goals that use the RT RF data.

The Active and Passive Plasma Sounder (APPS) subsystem baselined for the PILOT mission concept uses well-established active plasma sounding [105, 106] and passive observation techniques [12] to determine the total in-situ electron plasma density.

The notional APPS is an electronics board (Digital Fields Waves - DFW) that uses the RT RF antennas to actively and passively measure the local upper hybrid frequency (f_{UH}). This frequency is uniquely determined by the total in-situ electron plasma density and the in-situ magnetic field magnitude.

In active mode (best for densities < 100 cm^{-3}), APPS uses voltage-controlled antenna surfaces to transmit a low-power ($\sim 100\ \mu W$, ~ 3 V), electrostatic, broadband white-noise signal into the plasma. The plasma responds by resonating at f_{UH}, the plasma frequency

f_{pe}, and harmonics of the electron cyclotron frequency Nf_{ce} [105, 106]. This signal is broadcast for a few ms, followed by a period when APPS 'listens' to the plasma response as a receiver. APPS digitizes the 'listen' voltage data from the antennas as a time-series, then performs rapid on-board Fourier transforms to produce wave power spectra. Plasma resonance signals are extracted on the ground from the power spectral data and used to determine the plasma density (e.g. [133]).

In passive mode (best for densities > 100 cm^{-3}), APPS functions identically to active mode, but without transmitting the sounding signal. At these densities, natural resonant plasma fluctuations at f_{UH} create signals large enough to be detected by passive receivers [12].

A small portion (< 0.5 s) of the $\sim$10 s RT RF duty cycle (§C.1, §D.1) is set aside for APPS operation (instead of sending / receiving RT RF signals). The APPS on each RadioSat operates first in passive mode, then in active mode, ensuring a density measurement in any ambient density. Data returned consist of a one-channel power spectra with sufficiently high frequency resolution to measure plasma density to $\Delta n/n = 25\%$ or 5 cm^{-3} precision (Table STM-2).

APPS ground calibrations include electrical frequency-response tests to verify operation of the transmission and receive signal paths, as well as duty cycle alignment with RT RF operation. No on-orbit calibrations are required. Because plasma resonance frequencies relate to the plasma density by fundamental physical constants, APPS precision and accuracy are limited primarily by the frequency resolution of the power spectra used.

APPS signal processing occurs in FPGA-based firmware, using evolutions of heritage algorithms implemented on prior missions [106]. Flight software implemented in the RadioSat RT instrument processor packetizes data from APPS and forwards it to the spacecraft C&DH system for storage and transmission to the ground. Appropriate flight software modules exist with direct heritage from MAVEN LPW [106].

Analysis of APPS power spectral data is well developed given prior observations by active relaxation sounders [133] and passive f_{UH} detection in the inner magnetosphere [12]. An example of data from the Cluster Whisper relaxation sounder during a crossing of the plasmapause is shown in Figure C.2 [133].

C.2 RadioSat FGM Instrument

On PILOT, it is critical to have a near-equatorial, distributed network of space-borne DC-coupled vector magnetic field measurements for two reasons: (i) to constrain the geomagnetic field configuration in the inner magnetosphere, (ii) to determine spatial variation in ULF wave properties and place constraints on ULF wave azimuthal mode number (SQ 3a §2.2). Knowledge of the magnetic field and its spatial variability on scale sizes comparable to RadioSat spacing is important for all PILOT science questions (Table STM-1) in order to (i) quantify spatial variation of magnetic flux tubes that mediate mass transfer between the ionosphere and plasmasphere (SQ 1a, 1b), (ii) determine the spatial size of regions undergoing specific transport processes (SQ 2a, 2b), and (iii) determine the spatial sizes of both Earthward plasma flow magnetic perturbations and wave growth regions (SQ 3b, 3c).

FGMs have over 60 years of space flight heritage from dozens of missions. The FGM baselined for PILOT is similar to those flown on ST5 [134] and GTOSat [123]. Similar FGM

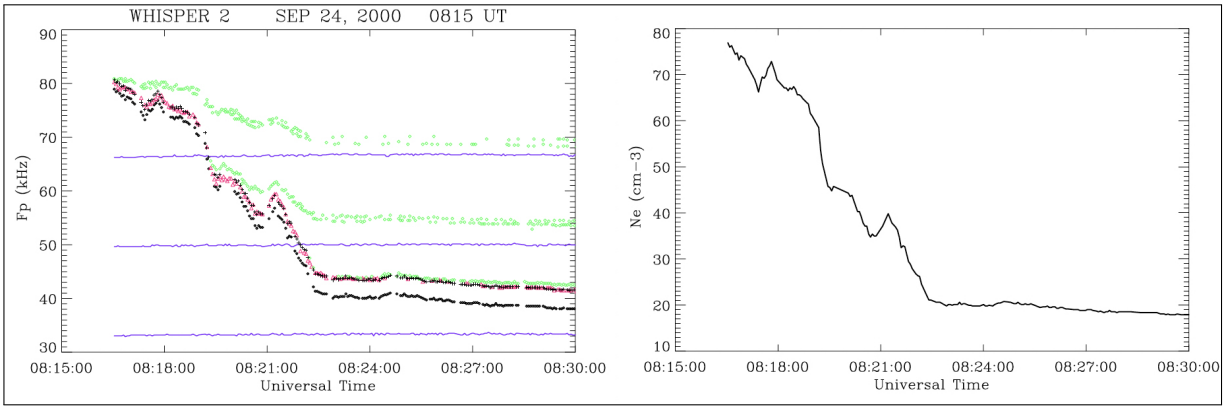

Figure C.2: *Top: Plasma resonances observed by the Cluster Whisper instrument during a plasmapause crossing. Bottom: Total plasma density derived from the observed resonances. Figure after [133].*

designs have flown on multi-spacecraft mission like THEMIS [135] and MMS [136]. FGM technology is well understood and highly mature. The FGM from GTOsat is shown in Figure C.3. Identical FGMs and booms are used by the PILOT RadioSats and PlasmaSats (§C.4).

FGMs are sensitive to magnetic fields generated by a spacecraft bus and other instruments. This is mitigated by locating the FGM sensor on a deployable boom from the spacecraft. A 2 meter rigid deployable carbon-fiber boom provides adequate mitigation for the PILOT RadioSats [137].

Time-series data from the three orthogonal FGM axes are continuously sampled, filtered and digitized by the magnetometer electronics board before being packetized and sent to the spacecraft. The PILOT FGM must have at least two selectable ranges, a high range covering up to ∼64,000 nT, for observations within a few R_E of Earth, and a low range covering up to ∼1000 nT, for observations beyond a few R_E of Earth, where higher sensitivity (∼ 0.1 nT) is required to observe ULF waves (§2.2, SQ 3a). Required sample rates are listed in Table STM-2. Switching between ranges can be triggered by the radial distance of a given spacecraft from Earth, without ground command intervention.

Ground calibration of the fluxgate magnetometer is done inside a Helmholtz coil where the local magnetic field can be brought to zero along all axes and then set to known calibrated values. As thermal variations are important to understand for the sensitive magnetometer measurements, testing occurs inside a non-magnetic thermal vacuum chamber where the magnetometer is brought to a given temperature before the system is turned off and a measurement is made. This approach was used with great success for the BARREL experiment which flew ∼40 balloon magnetometer payloads over the course of two years [138]. There are a number of facilities capable of performing these calibrations, including at UCLA, the Billingsley Aerospace & Defense Testing Facility, and the Mario H. Acuna Magnetic Test Facility at NASA Goddard Spaceflight center. In flight, the spin-modulation of FGM signals on the PlasmaSats is used for offset drift identification and removal [139]. On the RadioSats, periodic rolls of the spacecraft can be used for offset drift identification and removal.

FGM signal processing occurs in FPGA-based firmware, using evolutions of heritage algorithms that were implemented on prior missions ([123, 136, 139]. Flight software implemented in the RT (RadioSat) or EMF (PlasmaSat) instrument processor packetizes data from the FGM and forwards it to the spacecraft C&DH system for storage and transmission to the ground. Appropriate flight software modules exist with direct heritage from Van Allen Probes EMFISIS [111], and Parker Solar Probe [140].

Analysis of FGM three-axis time-series data is well developed given the long flight heritage of these instruments. Established techniques exist to synthesize a network of FGM measurements into high-resolution models of the geomagnetic field in the magnetosphere (e.g. [141]). An example of individual spacecraft FGM data [81] is shown in Figure C.3.

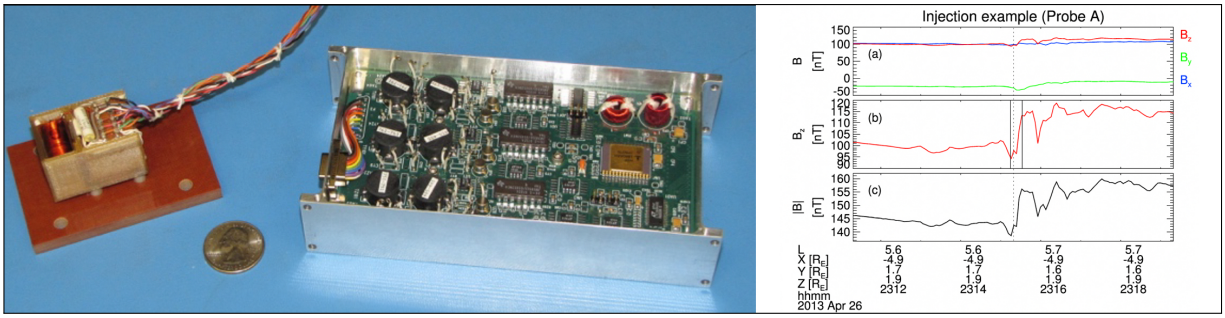

Figure C.3: *Left: FGM sensor and electronics from GTOsat (Figure from [123]). Right: Example FGM data, Figure after [81].*

C.3 RadioSat EED Instrument

A distributed network of energetic electron measurements is critical to addressing key aspects of SQ 3b and SQ 3c (§2.2). For SQ 3b, existing single-point and serendipitous multi-point measurements are insufficient to determine how, upon encountering the cold plasmasphere, energetic particles are removed from Earthward plasma flows and injected into the trapped drift paths that define the radiation belts [72, 74, 76]. For SQ 3c, the distribution of cold plasma density is expected to modulate plasma wave growth rates and therefore their ability to scatter energetic electrons into the atmosphere. In both cases, a distributed network of energetic electron measurements is needed to quantify the spatial and temporal variability of particle flux during and after its initial injection into the inner magnetosphere.

To accomplish this measurement, the PILOT RadioSats each carry an Energetic Electron Detector (EED), with a wide field of view centered on the orbital plane, designed to measure magnetically trapped energetic (50 keV to 3 MeV) electron fluxes.

An instrument with a cubesat resource profile is appropriate for this measurement because the primary goal is to resolve time variability of trapped electron fluxes at many locations, not to achieve highly accurate absolute phase space density values. Therefore: (i) pitch-angle resolved measurements are not required, (ii) a moderate level of background contamination due to secondary particles produced through higher energy particle interaction with the EED housing is acceptable.

The EED instrument baselined for this study is based on the μCPT (Micro-Charged Particle Telescope) flown as part of a solar cell degradation experiment on the AeroCube-10 designed and operated by The Aerospace Corporation [142, 143, 144]. The AeroCube-10 version of the μCPT is an electron and proton sensor configured to measure the differential flux of ions over the range of 80 keV to 1 MeV, hydrogen isotopes from 1.5 to 3.9 MeV, alpha particles from 1 to 4 MeV and electrons from 100 keV to 2.5 MeV.

The AeroCube-10 μCPT instrument consists of an aluminum collimator assembly with tantalum baffles providing a 48 degree field of view to a stack of custom silicon detectors. A filter foil of 18 μm thick aluminum integrated in front of the detectors protects the front detector from total dose of low energy ions. It also blocks sunlight or other sources of illumination that can otherwise contaminate the particle detection scheme. Detector signals are amplified by a front-end electronics board located behind the detector stack. An application specific integrated circuit called DAPPER (dual-Amplifier with Pulse Processing and Energy Readout) originally flown on the NASA MMS FEEPS instrument [145] provides low noise amplification, pulse shaping, and Wilkinson rundown of the pulse peak to form a digital pulse whose width is proportional to the detector signal. An FPGA-based back-end electronics board provides digital conversion of these pulse-width energy signals, binning of particle species and energy, and serial communication of the data to the spacecraft. Housekeeping electronics are integrated as part of the instrument's modular electronics suite and handles power to the sensor subsystem while a dedicated board handles biasing to the detectors.

The sensor operation is automated following turn-on and can respond via scheduled commanding to collect/read out data in different rate collection modes. The PILOT required cadence of 15 s for electron flux measurements on the RadioSats is easily met. A picture of the μCPT flown on AeroCube-10 along with a diagram of it is shown in Figure C.4.

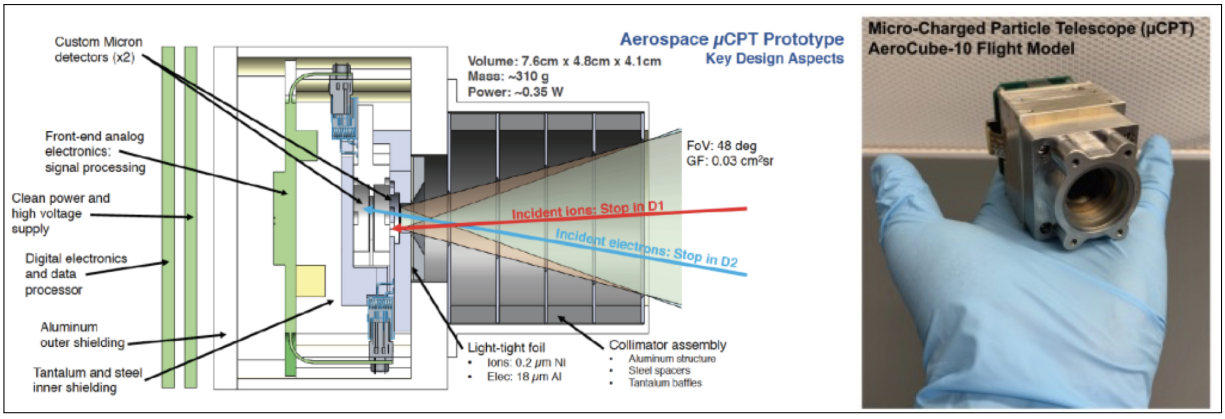

Figure C.4: *μCPT instrument diagram (Left) and picture of μCPT flight unit flown on AeroCube 10 (Right). Figures courtesy of Aerospace Corporation.*

The μCPT is a self-contained instrument following the philosophy of the other PILOT instruments. Instrument configuration is accomplished by uploading configuration files through the spacecraft bus into the FPGA back end board of the μCPT which enables setting threshold and other configuration parameters. Analog signals from the detectors

are digitized and histogrammed according to uploaded configuration files. This approach leverages heritage instrument architecture from the MMS and Van Allen Probe missions [124, 145]. The data is sent to the spacecraft over a serial connection to be packetized and transmitted to the ground. The configuration file can be changed to poll histogram data at different rates as needed in flight.

Data from the μCPT are straightforward to analyze, following processes developed on other NASA missions (e.g., THEMIS, MMS). Existing processing code can be tailored for the PILOT mission easily even with the large number of μCPT instruments flown.

The μCPT histogram data files contain the particle counts per channel per timestamp. Ground software can be used to process the raw counts data into count rate or differential flux (or energy flux) using the sensor geometry factor and sensor channel efficiencies as informed by Geant4 simulations and ground calibration.

Ground calibration of the μCPT has two stages. The first involves a detailed calibration of a set of five units at a particle accelerator to understand the response of the instrument to an electron beam at different energy and incident angles and current intensities. This is verified with Geant4 simulations to ensure the instrument behavior is well understood, mapped and modeled. The second stage involves characterization using laboratory sources (e.g., 137Cs, 244Cm and 207Bi) for detector characterization, cross calibration and identification of any units that have significant variation from expected behavior. This stage screens out poor performers and units with issues that can be sequestered, and identify any issues so they can be addressed for future production units. Multiple units can be tested at once in an automated or mostly automated fashion to speed the evaluation process. Accelerator data from the design production run and the calibration with sources provides excellent understanding of the absolute and relative calibration of the electron flux detectors. In-flight calibration involves cross-calibration between units that were not accelerator-tested with at least two accelerator-tested units. Calibration factors comparing data between units can be applied to data during ground processing.

C.4 PlasmaSat EMF Instrument Suite

The ElectroMagnetic Fields (EMF) is a suite of instruments including the Electric Field Instrument (EFI), Active and Passive Plasma Sounder (APPS), Fluxgate Magnetometer (FGM) and Search Coil Magnetometer (SCM). Together, they measure in-situ electric and magnetic fields in the inner magnetosphere. This suite of instruments covers the broad range of frequencies and amplitudes (specified in Table STM-2) that are required to address PILOT science objectives (Table STM-1) and bring closure to PILOT science questions (§2.2).

The PILOT concept study baseline EFI and SCM instruments are based on the Van Allen Electric Fields and Waves instrument [111] and the EMFISIS instrument suite [112]. On PILOT, they share common electronics and signal processing hardware. APPS is based on the relaxation sounder on the MAVEN LPW instrument [106] and operates similarly to the Cluster Whisper instrument [105]. The FGM baselined here is similar to those flown on ST5 [134] and GTOsat [123]. APPS and FGM are also part of the PILOT RadioSat instrument payloads, utilizing nearly identical hardware in their RadioSat and PlasmaSat configurations.

EFI uses the double probe technique [109] to measure electric fields from DC to hundreds of kHz, as well as the spacecraft floating potential. Two-axis electric fields are sufficient to address PILOT science (§2.2). EFI includes four voltage sensors deployed along 50 m wire booms that extend orthogonal to the spin axis of the spacecraft. The spin plane sensors are 4 cm radius conducting spheres with a set of preamplifiers located a few meters from the sensor. The sensors are current biased to control their floating potential with respect to the ambient plasma. The spin plane booms are deployed after launch gradually as the spacecraft spins, using angular momentum to extend and keep the booms deployed.

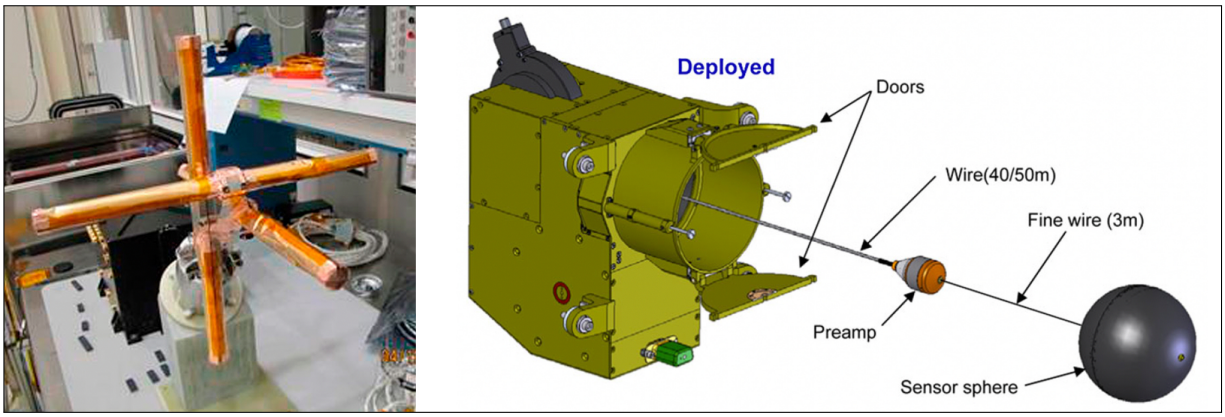

Figure C.5: *Left: Van Allen Probes SCM sensors [112]. Right: Van Allen Probes EFI spin plane booms deployer, preamplifier housing, and voltage sensor sphere [111]*

APPS uses relaxation sounding and passive observation of plasma resonances to measure total electron plasma density. The APPS instrument, data, and operation is described in §C.1.2. The PlasmaSat APPS uses the EFI spin plane booms to stimulate the plasma, and the EFI voltage sensors to measure the driven resonances. APPS and EFI preamplifiers are co-located. The sounding pulse and measurement are controlled by the Digital Field Wave board (DFW) housed within the EMF electronics enclosure. The PlasmaSat APPS uses the same preamplifiers and DFW board as the RadioSat RT APPS instrument. Minimal changes in FPGA firmware are needed for duty cycle coordination with EFI.

The FGM measures the DC-coupled vector magnetic field via the flux gate technique [136]. The FGM sensor is held away from the spacecraft bus using a 2m boom, in order to provide a low-noise measurement [137]. The FGM sensor, boom, and signal processing electronics used for EMF are identical to the FGMs used on the PILOT RadioSats (§C.2).

The SCM measures AC-coupled vector magnetic fields using a set of three solenoids mounted orthogonally on a 2m boom. The boom provides a low-noise measurement environment, far from the spacecraft, for the SCM sensors. The baseline SCM is based on previous instruments including SCMs on CRRES, Polar, Wind, Van Allen Probes, and Juno [146]. Each solenoid utilizes a mu-metal core wound with wire. PILOT requires sensitivity over the frequency range 10-15,000 Hz which is similar to the Van Allen Probes SCM, shown in Figure C.5.

The PILOT EMF baseline configuration has a common electronics enclosure consisting of several electronics boards: (i) the Boom Electronics Board (BEB) generates voltages and

currents needed to bias the EFI probes and surfaces near the sensors. The BEB also receives and filters signals from EFI before passing them to the Digital Fields Board (DFB), (ii) The DFB processes the analog signals from SCM and EFI performing anti-alias filtering, analog to digital conversion, and onboard digital signal processing, including calculation of time-series, spectral, and cross-spectral products, (iii) The APPS DFW board generates a low-power electrostatic white noise pulse on the EFI booms and measures the frequency of plasma-resonance waves driven by the pulse using signals from the EFI sensors, (iv) FGM sensor signals are passed to an FGM electronics board that extracts magnetic field information, then digitizes these data, (v) The EMF common electronics enclosure also includes a Power and Bus Interface board (PBI), which handles regulation of the spacecraft bus power to support the electronics and detectors, instrument level housekeeping data collection, buffering of data in internal EMF memory, as well as command and data handling between the instrument and spacecraft bus. This board arrangement is similar to Van Allen Probes EFW or EMFISIS with the addition of the APPS DFW board and the functionality of the Data Controller Board (DCB) and Low Voltage Power Supply (LVPS) combined as the PBI board.

All EMF instruments have a single operational mode: continuous survey sampling. EFI and FGM DC-coupled data are recorded as time-series (two differential and four single-ended signals for EFI, three axes of FGM), while EFI and SCM AC-coupled data are reported using on-board calculated power spectra (two EFI axes, three SCM axes) and all real and imaginary 5x5 cross-spectral matrix components. APPS data consist of one axis of high frequency electric field power spectra. Representative time-series and spectral data from Van Allen Probes EFW and EMFISIS are shown in Figure C.6.

Spectral and time-series data compression schemes successful on similar instruments are assumed here [147]. Similar to the Van Allen Probes FGM [112], the PILOT FGM requires multiple gain states to cover the required amplitude range ($<$ 0.1 nT to 10,000 nT). The gain state changes can be triggered based on the radial distance of the spacecraft from the Earth. Sample rates for time series and spectral data required to address PILOT science are reported in Table STM-1.

The EMF data volume estimate is in Table 4.4. It is based on operation of the heritage instruments described and the measurement cadences required for PILOT (Table STM-2).

EFI ground calibrations include electrical frequency-response and deployment tests (as in [111] and [114]). EFI in-flight calibrations include (i) for DC-coupled signals, comparisons with the motional electric field near perigree [148], (ii) for AC-coupled signals, comparisons with plasma wave SCM data [149]. The spin-modulation of EFI signals is used to identify and remove any spurious offsets.

FGM ground calibrations are described in §C.2. In flight, on the PlasmaSats, spin-modulation of FGM signals is used for offset drift identification and removal.

The SCM is calibrated on the ground using solenoid calibration coils and μ-metal shielded containers. In flight, the EMF Digital Fields Board (DFB) can periodically generate a calibration signal (e.g. [147]) to identify any variation in gain or phase response over time.

APPS calibrations are discussed in §C.1.2. In flight, APPS data provide the gold standard for plasma density [105], and are used to calibrate other density measurements.

Duty cycling of APPS and EFI high-frequency measurements can be implemented, as on Cluster WHISPER, if APPS sounding is found to interfere with EFI high-frequency measurements.

The bulk of EMF signal processing occurs in FPGA-based firmware, using evolutions of heritage algorithms that were implemented on prior missions [111, 112, 140, 147]. Flight software resides only in the PBI, and serves primarily to packetize and buffer the processed data from the other electronics boards and communicate with the spacecraft (sending data, receiving commands, configuring the firmware on the other EMF boards). Appropriate instrument-specific flight software exists with direct heritage from Van Allen Probes EFW [111], Van Allen Probes EMFISIS [111], and Parker Solar Probe [140].

The complexity of PILOT EMF data analysis is similar to the complexity of analysis for THEMIS EFI or Van Allen Probes EFW or Van Allen Probes EMFISIS data sets. The major advance and additional complexity for PILOT is the availability of simultaneous plasma density, electron flux, and magnetic field constellation data products (§E.2), as well as meridional plasma density and flow structures (§C.7). PILOT EMF observations are be embedded within these spatially broad contextual data, and must be analyzed and interpreted as such to achieve the PILOT scientific objectives (§2.2). A common method of accessing constellation, remote sensing, and in-situ data products is required to take full advantage of the synergy between these measurements (§E.1).

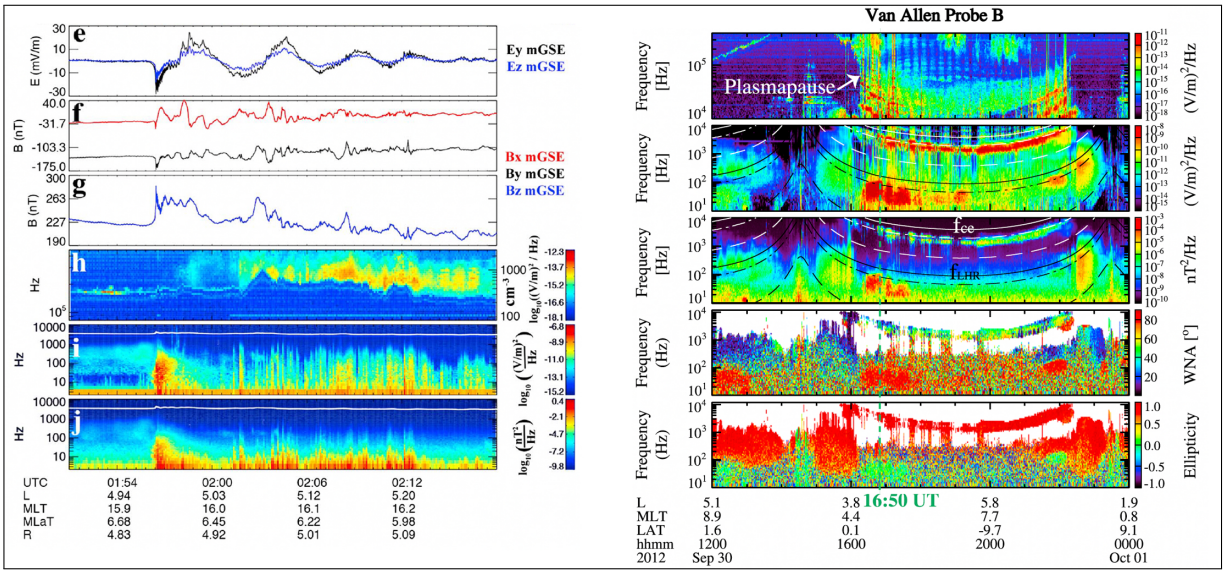

Figure C.6: *Left: Example EMF-type data from Van Allen Probes, after [150], DC-coupled electric and magnetic field data (e,f,g), upper hybrid line data (h), plasma wave spectra (i,j). Right: Example EMF-type data from Van Allen Probes, after [151], including plasma wave spectra and wave polarization from cross spectra.*

C.5 PlasmaSat EPS Instrument

The Energetic Particle Sensors (EPS) consists of five electron and proton magnetic spectrometers per PlasmaSat. Together, they measure the in-situ energy flux and distributions

in energy and pitch angle for energetic electrons ($\sim$ 0.2 to $\sim$ 1.5 MeV) and protons ($\sim$ 0.15 to $\sim$ 8 MeV). EPS mass, power, and data rate are listed in Table 4.4. A magnetic spectrometer particle detector is used to achieve low-noise observations while traversing the radiation belts, where high penetrating radiation and secondary particle fluxes are present.

The field of view for each spectrometer is 20^o by 10^o, and five spectrometers are arranged on each PlasmaSat such that the 20^o portion of their fields of view are symmetrically distributed along the 180^o between PlasmaSat spin axes. This arrangement, combined with the spacecraft rotation, enables a nearly full sky coverage with the PlasmaSat spin axis orientation. Each individual PILOT EPS spectrometer is baselined to be an identical copy of the REMS instrument on GTOSat [123]. REMS is a miniaturized version of the MagEIS-Medium instrument on Van Allen Probes [124].

Figure C.7 shows a schematic of the REMS magnetic spectrometer. Particles entering the aperture have their trajectories bent onto a detector array with the gyroradius determined by the particle energies and the instrument's internal magnetic field. Electrons are detected by one of the nine silicon detectors located on the aperture wall. Protons are deflected in the opposite direction towards the proton detector array opposite to the aperture. The REMS design utilizes a series of nine 1.5 mm thick silicon detectors for electrons and one detector for protons. The internal magnetic field $\sim$ 1590 G is produced by a samarium-cobalt alloy. The detectors and magnetic field can be adjusted to optimize the energy range. A magnetic yoke blocks most of the magnetic field from extending beyond the yoke. The chamber design is based on MagEIS-Medium which measured stray fields of $<$ 1 nT at a 1 m distance [124], which is sufficiently small for PILOT FGM measurements.

EPS data readout occurs via a multi-chip ASIC, which amplifies and digitizes the charge pulse from each silicon detector pixel. Each of the five EPS spectrometers on each PlasmaSat has its own interface control unit and power regulation system. This maximizes GTOsat heritage.

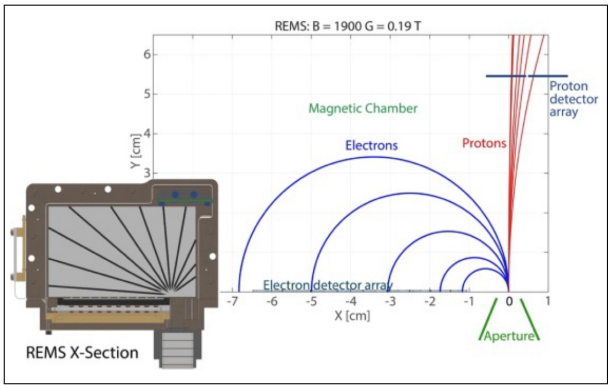

Figure C.7: *Schematic of a single REMS magnetic spectrometer. Figure from [123].*

EPS data undergoes pulse height analysis and is binned on the spacecraft into energy channels to form flux vs. energy data products similar to those on THEMIS or MMS. Pulse height data on each detector can be transmitted if there is need and telemetry allows. EPS has one operational mode: science mode, where standard particle and housekeeping data are sampled on sub-spin cadences sufficient to create full-sky distributions in energy and pitch angle. The cadence of sub-spin measurements can be adjusted by command.

Ground calibration of the detectors and electronics make use of laboratory radiation sources such as Bi-207, Pm-147, and Ni-63 and a beta spectrometer. This testing is used to confirm the response of each silicon pixel and determine the gain and offset of each electronics channel. For at least five individual spectrometer flight units, the angular and energy response are fully characterized using using particle accelerator beam testing at

a LINAC or synchrotron accelerator facility. In flight, each preamplifier can be pulsed during calibration runs to measure the gain, offset and noise of each channel. Data can be compared between beam-tested and non-beam-tested individual spectrometer units to identify and correct for any significant variations among the silicon detectors. EPS uses existing flight software and analysis software written for the MagEIS and REMs instruments with only minor changes.

C.6 PlasmaSat PIMS Instrument

The Plasmaspheric Ion Mass Spectrometer (PIMS) obtains in-situ distribution functions (flux versus energy, pitch angle, gyrophase angle) and derived moments (density, temperature) for three major ion species (H^+, He^+, O^+) and electrons. These local measurements provide essential microphysics and ground-truth information for multiple SQ: proton data required for all SQ, and He^+, O^+ data vital for SQ 1a, 2a, and 3a, and contextually important for SQ 3b and 3c. The PILOT baseline for PIMS is a nearly identical copy of the Van Allen Probes HOPE instrument (Figure C.8) that comprises an electrostatic analyzer (ESA) with a time of flight (TOF) section [118].

Figure C.8: *Van Allen Probes HOPE flight unit*

Measurement of full cold ion distributions (down to ∼0 eV) is enabled by a Sensor-Panel Bias (SPB) system: biasing the entire PIMS instrument and its adjacent spacecraft (SC) panel negative relative to SC chassis ground. Biasing an instrument or its aperture has been performed previously, e.g., Cassiope/e-POP, Freja, and DE-1/RIMS [119, 120, 121, 122]. PILOT builds on these previous methods by biasing the entire adjacent SC panel plus instrument, allowing cold ions to reach PIMS while minimizing angular deflection.

PIMS's modular design allows it to be biased negative with very minor changes from the flight-proven design of Van Allen Probes HOPE. Instrument ground is biased relative to the SC by a negative, stepping, low-voltage power supply enclosed in a separate Bias Box (BB). The PIMS Mass spectrometer Electronics Unit (MEU) connects to the BB rather than to SC ground. The adjacent SPB spacecraft panel is also at instrument ground. The SPB system is thus implemented without altering the heritage sensor or MEU, which are TRL 7. All parts in the BB and SPB panel are TRL 6 or higher. The current to maintain the maximum SPB bias voltage (–60V) is <1 mA.

The PIMS field of view (FOV) is discretized into $18^o \times 4.5^o$ pixels centered at incident polar angles of [0^o, $\pm 36^o$, $\pm 72^o$] (0^o=perpendicular to the SC spin axis), thus with an instantaneous FOV of $162^o \times 4.5^o$ and a per-spin FOV of $162^o \times 360^o$. The per-spin sampling is programmable (i.e., can be increased) based on inflight calibration.

PIMS measures ions in 72 logarithmically spaced energy steps, every 750 ms. Each sweep covers energies at the aperture from 1 eV – 50 keV. Coupled with the SPB that accelerates cold ions to the aperture, ambient ions of 0 eV – 50 keV are measured. Successive

bias voltage steps can be programmed (e.g., once per SC spin, or in multiples of the 750 ms energy sweep) to make multiple measurements of cold ion distribution functions (Figure C.9).

Figure C.9a shows simulated potentials (using the Curvilinear Particle-In-Cell (CPIC) code) for Bias Voltage=–30V and SC potential=+5V. All cold ions can reach the instrument aperture. Figure C.9b shows potential vs radius: Bias Voltage=–30V case has no potential barrier. Figure C.9c shows count distribution functions for Bias Voltage Steps=[–6.5, –10.5, –20, –30]V. Stepping through several voltages provides multiple measurements of the ion distribution. These multiple measurements (including at bias = 0 V, i.e., unperturbed) are used together (and alongside self-consistent particle-in-cell modeling) to remove any angular distortion introduced by the SC potential sheath.

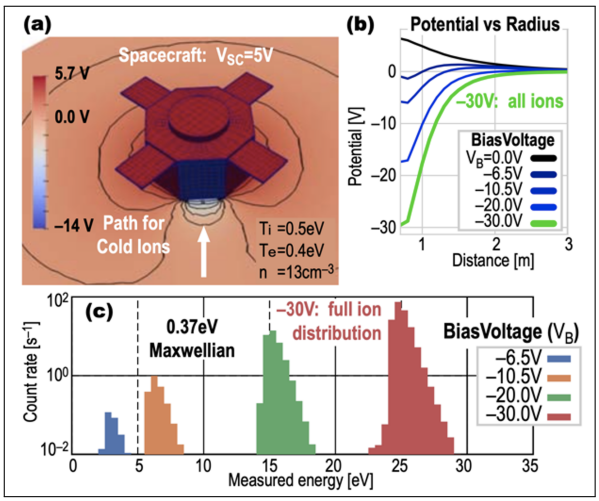

Figure C.9: *The Sensor Panel Bias (SPB) system enables measurement of the coldest ions (to 0 eV). Details in text.*

The PIMS total data volume is given in Table 4.4. PIMS flight software, data processing, and data analysis techniques are similar to those used by Van Allen Probes HOPE.

C.7 PlasmaSat EUVCS Instrument

The Extreme Ultraviolet Camera System (EUVCS) is an imaging suite comprising 2 imager types: EUV-He and EUV-O.

EUVCS provides global images of extreme ultraviolet (EUV) light scattered by plasmaspheric He^+ at 30.4nm (EUV-He) and O^+/O^{++} at 83.4nm (EUV-O). These populations are both high priority science targets. The morphology of the He^+ population is a reliable proxy for that of the dominant H^+ ions or electrons [36, 37]. The O^+/O^{++} population, i.e., the dense oxygen torus, has a dramatically different morphology from the light ions and electrons, and can drastically alter the plasma mass density [37, 125]. EUVCS images the meridional distribution, orthogonal and complementary to the equatorial distribution obtained via radio tomography (§D.1).

The EUV-He and -O instruments baselined for PILOT are mechanically and electrically identical to each other, with respective bandpasses determined by choice of filter material multilayer (ML) mirror coating [34, 125]. The optical design is an evolution of IMAGE EUV [126] with mirror diameter and radius of curvature increased to expand FOV from 30^o to 40^o and to improve the resolution from 0.6^o to 0.45^o [125, 127] , but the design is otherwise identical to IMAGE EUV (Figure C.11). Like IMAGE EUV, each sensor uses a spherical MCP detector at the focus of the mirror. The EUVCS detector electronics have Juno-UVS heritage.

EUVCS is mounted on a spacecraft with spin axis (+Z direction) normal to the orbit plane. EUV-He uses a 2-camera stack arrayed along Z, with each 40^o camera tilted ±18.5^o from the orbit plane, to obtain a 77^o FOV covering Z=±4.8 R_E (Figure C.10, top). This 2-camera EUV-He stack spins through the orbit plane to cover the plasmasphere torus within about one third of a spacecraft rotation. The dense oxygen torus is a smaller target: the EUV-O imager can use a single camera to observe Z=±2.2 R_E (Figure C.10, bottom), again swept across the target every ∼third of a spin.

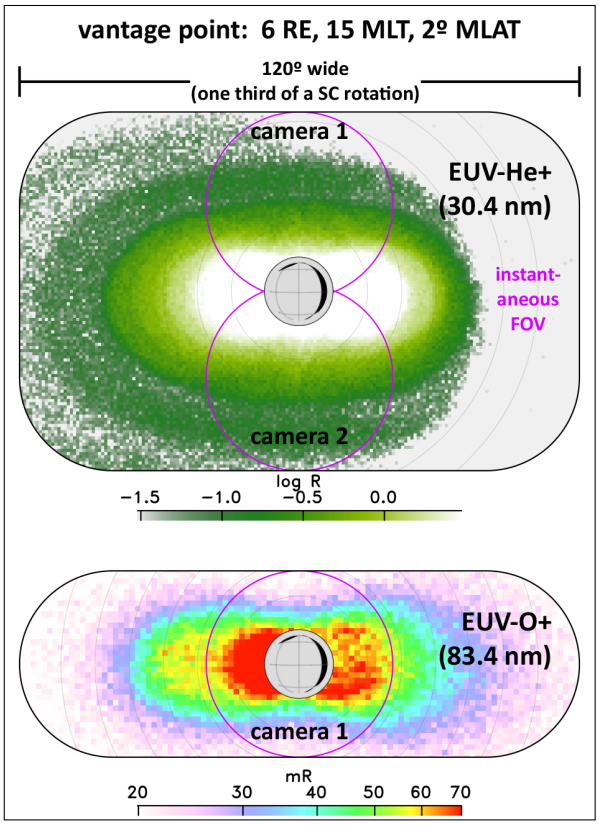

Figure C.10: *EUVCS images (simulated) of the He^+ and O^+/O^{++} distributions in the meridional plane, orthogonal and complementary to the equatorial distribution obtained via radio tomography.*

EUVCS has two operational modes: checkout and science. EUVCS electronics are programmed to reduce high voltage (HV) if the total count rate exceeds the safety level, either from ambient radiation/-particles or from sunlight in the FOV.

EUVCS optics are highly sensitive to contamination by particulates and non-volatile residues (NVR). Before installation, the EUVCS mirrors, filters and detectors are stored in purge boxes. EUVCS's optical cavities are protected by red tag covers and purged with GN2 (99.999% purity) from installation until launch, with maximum cumulative outage <5 hrs. Ideally, the spacecraft should be mounted with EUVCS entrance apertures facing downward for launch.

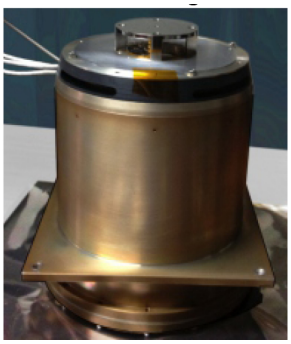

Figure C.11: *IMAGE EUV Flight Unit*

The version of the EUVCS baselined for PILOT is currently TRL 5, following development efforts to qualify partial-aperture filters, and the mirror coatings applied to flat SiO2 substrates. The Juno-UVS heritage electronics (C&DH, LVPS/HVPS) are TRL 6+. A robust/detailed Technology Maturation Plan (TMP), developed (for the 2019 TREO MIDEX proposal) by SwRI in partnership with Lawrence Livermore National Laboratory (LLNL), builds and tests a TRL 6 prototype (with swappable filters and mirrors for 30.4nm or 83.4nm wavelengths) in 11 months (§G.6).

EUVCS collects time-tagged photon count (TTPC) data consisting of 24-bit photon events (detector position and pulse height), interspersed with periodic 24-bit time markers (every 4ms–2s, adjustable). Maximum data rates before compression are 87 kbps per camera for EUV-He and 12 kbps for EUV-O (note dimmer 83.4 nm source [34]). The

estimated total data volume is given in Table 4.4. The EUVCS flight software is similar to Juno-UVS [152] and Alice [153] spectrographs.

Bringing down TTPC data enables on-the-ground optimization of images using adaptive time-binning and pixelization (e.g., conformal pixels, statistical smoothing, cf. [34]). Deconvolution of EUV-He images extracts densities and convection flow velocities using established techniques (§D.2, [48, 154, 155, 156, 157, 158]). Reconstructing O^+ density requires some development during the mission (as IMAGE did) to account for complexities of interpreting 83.4-nm images such as earthshine, O^{++} ions, and temperature effects [34, 159].

C.8 Instrument Integration and Test

The PILOT concept requires many copies of some scientific instruments, particularly for the 30 RadioSats, each of which carries three instruments (RT, FGM, EED). To mitigate risks associated with this requirement (§4.7), PILOT adopts integration and test philosophies developed by large commercial constellations such as Starlink and Planet.

The PILOT PlasmaSat instruments follow NASA Class C S&MA procedures, with parts selection consistent with a Flagship mission. PILOT draws on heritage from previous missions, such as MMS, THEMIS and Van Allen Probes to ensure successful production, integration, and test.

The 30 RadioSats are built using Class D S&MA procedures, until delivery for instrument integration, at which point the S&MA process transitions to Class C. PILOT adopts the approach used by MMS FEEPS [145]: a careful calibration and characterization of the first batch of five instruments. Subsequent units undergo acceptance testing. Instrument elements that perform out of family are taken out of production, evaluated separately, and may not be used for flight.

This approach enables selection of appropriate working flight systems without requiring an exhaustive analysis if one or two instrument elements fails testing. Production, integration, and test continue unless there is a failure across a number of instrument elements.

D Technologies and Techniques: Deconvolution

D.1 Radio Tomography Deconvolution

The PILOT radio tomographic imaging system produces rapidly refreshing (as fast as 10 s cadence) images of electron (total) plasma density with high spatial resolution over a large region of the inner magnetosphere. The PILOT mission concept baseline achieves image resolution as small as 0.4 R_E over a region of space ∼2 R_E in radial extent and ∼3.5 hours in MLT (Figure D.1). These images allow detailed tracking and analysis of cold plasma mass flow, as well as the impact of these flows on magnetospheric subsystems (§2.2). Radio tomographic images are made even more scientifically powerful by in-situ measurements within the image plane (§2.2).

Technological advancements in the last two decades make space-borne radio tomographic imaging feasible:

1. Spacecraft manufacturing technology has matured to the point where spacecraft can be fabricated and launched in the quantities needed for radio tomographic imaging with scientifically meaningful resolution (tens of spacecraft).

2. Instrumentation miniaturization has progressed to the point where microsat spacecraft can host instruments that return in-situ multi-point measurements surrounding the region of interest.

3. Launch and deployment costs for spacecraft constellations have dropped such that spacecraft can be arranged in two orbits to encircle the image region, enabling unique reconstruction of the electron density in that region.

4. Accurate in-situ measurement of electron density has been demonstrated in space using active plasma sounding techniques [105, 106]. These measurements are highly beneficial to radio tomographic image reconstruction [104].

Radio tomography imaging with PILOT is summarized in Figure D.1. Each of the RadioSat RT RF instruments transmits, one at a time, a coherently-phased pair of radio signals at two discrete frequencies that are received by all other RadioSat spacecraft. The measured phase difference combined with the group delay between the two signals yields an accurate measurement of TEC [104, 160]. Each transmission is slated to endure for 0.1 s followed by a 0.15 s wait to accommodate propagation delays until the next RadioSat transmits. In less than 10 seconds, each of the satellites has transmitted (Figure D.1b), after which, the transmission cycle repeats. At any given time, four satellites are expected to be behind Earth (near perigee) relative to the bulk of the RadioSat constellation. Therefore 325 TEC measurements (and 325 redundant measurements) are expected, along with and 26 in-situ plasma density measurements from the 26 active RadioSat spacecraft. The 325 TEC measurements and 26 in-situ plasma density measurements produce an image of total electron density every 10 s (Figure D.1c).

(a) 30 satellites are equally phased in two orbits. At any given time, 26 satellites are active in radio tomography (RT) imaging; the other 4 satellites are poorly positioned for RT imaging but ideally located for ground contact. Each satellite is given a time slot for transmission, which is received by all other active RT satellites as diagrammed on the right. The transmission endures for 0.1 s followed by a 0.15 s wait for signal propagation. The phase advance and the group delay between the two frequencies in the dual-frequency transmission results in a direct measurement of the Total Electron Content (TEC) between the transmitting satellite and each of the receiving satellites.

(b) In less than 10 seconds, each of the satellites has transmitted resulting in (N^2-N)/2 = 325 unique lines-of sight; each TEC measurement is redundant. Tomographic image reconstruction requires that (1) the image region (red dashed line) is densely covered by TEC lines-of-sight and that (2) the lines-of-sight have 2π angular coverage. For the latter requirement, it is important that the satellites surround the image region. The two-orbit mission design satisfies both requirements for tomographic reconstruction of a region surrounding the plasmasphere's boundary. Each of the satellites also measures the plasma density in-situ.

(c) The reconstructed image is based solely on 325 TEC measurements combined with 26 in-situ measurements of plasma density. The reconstruction region has 0.2 x 0.2 R_E pixels that are inside of at least one of the orbits and bounded by the inner-most lines-of-sight. There are more pixels than lines-of-sight, so the iterative tomographic reconstruction not only matches the TEC measurements, but also produces the image with least variance. The region is demarked by a dashed red circle is valid to ~0.4 R_E resolution. Outside of that region, the lines-of-sight do not have sufficient coverage or angular coverage. The black dashed line and magenta dashed line represent the two most challenging TEC measurements as discussed in the text.

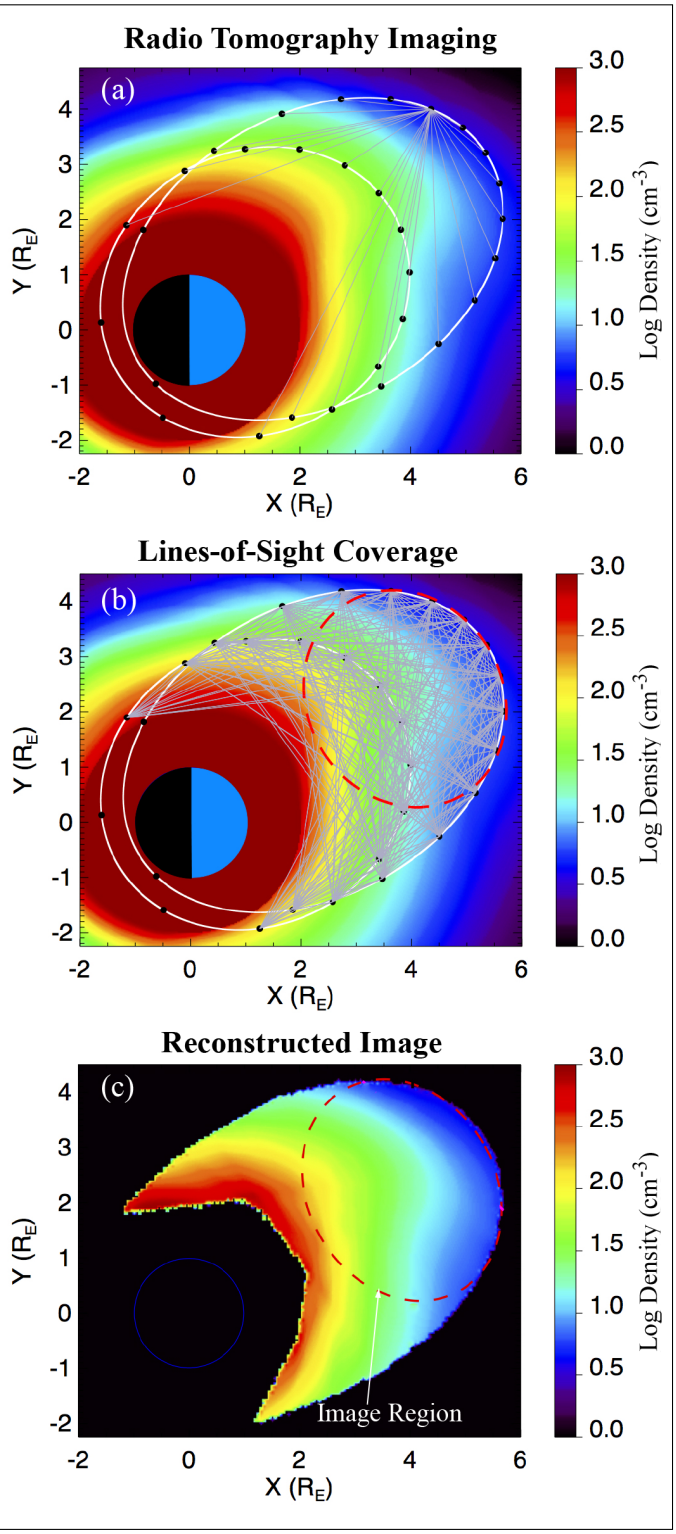

Figure D.1: *A description and demonstration of radio tomographic imaging of plasma density. The radio tomographic imaging can produce images of total plasma density every 10 s.*

D.1.1 Measurement of TEC

Radio propagation experiments and extensive use of GPS signals have demonstrated the ability to determine TEC using radio wave propagation (e.g. [161], [162] and references therein). The phase and group velocities of a radio signal propagating through a region of free electrons are well established [104]:

$$v_\phi = \frac{\omega}{k} \approx c\left(1 + \frac{\omega_{pe}^2}{2\omega^2}\right) \; ; \; v_g = \frac{d\,\omega}{d\,k} \approx c\left(1 - \frac{\omega_{pe}^2}{2\omega^2}\right) \tag{3}$$

Here, ω is the radio signal angular frequency ($\omega = 2\pi f$), k is the wave vector, c is the speed of light and ω_{pe} is the plasma frequency. Also, $\omega_{pe}^2 = n_e e^2/\epsilon_0 m_e$, where n_e is the total electron plasma density, m_e is electron mass, e is the electron charge, and ϵ_0 is the permittivity of space). Radio signal phase advance (δt_ϕ) and group delay (δt_g) acquired during propagation over a distance L are linear with electron density:

$$\delta t_\phi = -\frac{C}{\omega^2}\int_0^L n_e dl = -\frac{C}{\omega^2} TEC \; ; \; \delta t_g = \frac{C}{\omega^2}\int_0^L n_e dl = \frac{C}{\omega^2} TEC \; ; \; C = \frac{e^2}{2c\epsilon_0 m_e} \tag{4}$$

Importantly, δt_ϕ and δt_g, are sensitive to the inverse of the radio wave frequency squared ($1/f^2$). In practice, δt_ϕ and δt_g, are very small compared to L/c, so single-frequency measurement would require extremely accurate clocks (1 part in 10^{12}, see §G.1) and a precise measurement of L (accurate to $\sim$ 1 m). A dual-frequency carrier method avoids these two issues entirely. A low-frequency signal (f_L) is far more sensitive to TEC than a high frequency signal (f_H) so the TEC can be determined [104] as:

$$TEC = \frac{4\pi^2}{C}\frac{f_H^2 f_L^2}{f_H^2 - f_L^2}\delta t_{\phi HL} \tag{5}$$

Where $\delta t_{\phi HL}$ is the time delay between the two carrier frequencies. The advantage of the two-carrier method is clear (Equation 5): the two carrier frequencies can be precisely known and the time (phase) delay between them can be very accurately measured. Details of a two-carrier system implementation are in §C.1.1.

D.1.2 Radio Tomographic Image Reconstruction

Once TEC is measured between all spacecraft line of sight pairs and the data are received by ground stations, the plasma density image can be tomographically reconstructed. Image reconstruction for a space-borne system differs from that used in medical scans. Medical scans use circular lines-of sight with high-resolution, well-defined angular coverage, and they deliberately oversample the image region. In space, one cannot arrange spacecraft in a perfect circle around a region of interest and the number of unique lines-of-sight are limited to $(N^2 - N)/2$, where N is the number of satellites, so over-sampling requires an impractical number of spacecraft.

Electron density images are constructed from the TEC and in-situ density data. For example, the image in Figure D.1c was reconstructed solely from TEC and in-situ density data (extracted from IPE model simulation data [132]) using an iterative inversion technique. This technique produces an image with the least variance that satisfies the TEC

and in-situ density measurements [104, 163]. As stated above, the two most important considerations are the spacing of the lines-of-sight and the angular coverage of the lines-of-sight. A two-orbit configuration provides the needed spacing and angular coverage for PILOT science goals.

The reconstruction algorithm for unevenly spaced lines-of-sight is iterative. An extended region between the spacecraft is gridded with 0.2 R_E × 0.2 R_E pixels (the jagged region in Figure D.1c). In inversion is not necessarily valid in the region outside the red dashed circle in Figure D.1b, since there are many more pixels than lines of sight. To initialize, the pixels are assigned a previous image or a time-averaged value. Pixels that contain an in-situ measurement are fixed at the in-situ value of electron density.

To converge to a valid reproduction of the density, several image quality metrics are evaluated. TECError is the difference between the actual (measured) TEC and the TEC derived from the current iteration of the image for each line-of-sight. The lines of sight that are completely inside the red dashed circle in Figure D.1b are given the highest weighting. The path length of each line-of-sight in each of the pixels is used in this evaluation. NeVar is the RMS normalized variation between all of the pixels and the surrounding four pixels. For each iteration, the pixels containing at least one line of sight are adjusted to partially reduce TECError and NeVar. The reduction is targeted at $\sim 50\%$ of the TECError. The image is then smoothed with higher weighting on pixels with the most lines-of-sight or an in-situ measurement. Each pixel is then assigned a random variation (percent), which, a first, dominates the changes. TECError and NeVar are then recalculated and the process is repeated. As the iteration advances, the random variations are slowly reduced. These random variations are needed to assure that reconstruction is not caught in a local minimum of TECError and NeVar.

The end result of the reconstruction is an image of the electron density that satisfies the TEC measurements with the least variance. This process avoids implanting aberrant features in an electron density image at the cost of possibly suppressing a real feature. By repeating the pseudo-random reconstruction multiple times, uniqueness can be tested and uncertainties can be quantified [104].

D.2 EUV Image Deconvolution: Inversion and Forward Model Algorithms

The PILOT EUVCS instrument provides global, line of sight integrated images of photons resonantly scattered by plasmaspheric He^+ at 30.4nm (EUV-He) and by O^+/O^{++} at 83.4nm (EUV-O). EUVCS images the meridional plane of the magnetosphere, orthogonal and complementary to the equatorial distribution obtained via radio tomography (cf. diagram in upper right of Table STM-1).

Inversion of EUV-He images extracts ion densities and convection flow velocities. From these flows, the corresponding convection E-field can be derived. Using IMAGE EUV data, several existing, well-established but less sophisticated techniques have demonstrated the basic capability to retrieve density and full 2D flow vectors [48, 154, 155, 156]. The full potential of EUV inversion was demonstrated by state-of-the-art, Bayesian/ Kalman inversion algorithms that yield the most robust inversions to date [157, 158]. Because global He^+ density is a reliable proxy for total plasma density [36, 37], these improved

methods to estimate density (±10% inversion error) and electric field (±0.2 mV/m) permit an accurate accounting of transport and loss of mass during erosion. The baseline method assumes the EUV-He imager is located outside the plasmapause, but previous work has demonstrated the ability to perform "inside-out" inversion during times when the spacecraft is located within the main torus [164]. Complementary PILOT in situ measurements provide validation of these EUV-He inversions, and firmly anchor the system-level estimates to "ground truth" and microscale physics.

O^+ density structure differs from that of He^+ [34, 37, 125], so IMAGE EUV could not reveal global O^+ behavior. PILOT EUV-O fills this gap by measuring the global morphology and flows of O^+. In-situ O^+ data provide cross check of EUV-O images, and also reveal essential microphysics from density, temperature, and pitch angle distribution structure. PILOT's cross-scale O^+ observing improves system-level constraints on models of O^+ dynamics. Existing forward modeling codes [e.g. 34] are used to create simulated images, enabling iterative comparison with EUV-O images to constrain inversions. Reconstructing O^+ density from EUV images is challenging [159]; thus PILOT needs to mature its inversion/forward modeling algorithms during the mission (as IMAGE did) to account for complexities of interpreting 83.4-nm images such as earthshine, O^{++} ions, and temperature effects [34]. Deconvolving O^+ / O^{++} is aided by PIMS's ability to distinguish O^{++}.

E Technologies and Techniques: Data Accessibility, Constellation Data, and Model-Data Fusion

E.1 Accessibility of Constellation Data

Achieving closure on PILOT science requires combining data from an equatorial network of 30 spacecraft with remote sensing meridional images and data from multiple embedded in-situ probes. It is important to ensure that these data sets are accessible and useful to the Heliophysics community.

Achieving these goals requires an open-source software framework to access, retrieve, and process the data. The framework must be common amongst all PILOT instrument data to facilitate analyses that combine data types. The SPEDAS (IDL-based) and PySPEDAS (Python-based) software packages [165] currently fill this role for many Heliophysics missions, including multi-spacecraft missions like MMS and THEMIS. PILOT-specific modules can be added to the existing SPEDAS framework to enable common data access and processing formats.

E.2 Constellation Data Products

Magnetic field, electron flux, and plasma density data produced by the dozens of PILOT RadioSat spacecraft must be synthesized into data products that simplify their use by the broader Heliophysics community. The 'constellation data products' envisioned include time-dependent two dimensional equatorial maps of total electron density from radio tomographic inversions (§D.1), time-dependent three-dimensional best-fit global magnetic field maps, and time-dependent two dimensional maps of high energy (80 keV - 2 MeV) electrons in the radiation belts. Releasing constellation data products to the community reduces the data processing burden on any one researcher, such that a broad range of scientists can easily use and interpret the data.

Development of similar constellation data products has been achieved by several existing observatories employing broadly distributed arrays of observation points. For example, the AMPERE experiment synthesizes data from 66 spacecraft-based magnetometers into time dependant global and regional maps of ionospheric current systems [166, 167]. Also, United States total electron content (US-TEC) maps are constructed using data assimilated from several dozen GPS stations to produce two dimensional time dependant maps of ionospheric TEC [168, 169].

E.3 Model-Data Fusion

Fusing PILOT data with a modeling framework informs and validates the numerical, analytic, and physical models that codify advances in our physical understanding of mass and energy transport through the magnetosphere of a terrestrial planet. The following sections describe how specific modeling approaches can be applied to the multi-dimensional, multi-spacecraft PILOT data, and how that leads to new scientific understanding.

E.3.1 Empirical Models

The PILOT mission concept provides a data set with unprecedented spatial coverage of the inner magnetosphere. This offers excellent opportunities to apply empirical

modeling techniques to enhance the data quality, reconstruction of the magnetospheric environment, and physical discovery. Traditional empirical modeling relies on researcher-guided examination of spatial and temporal measurements of physical quantities of interest such as hydrogen and helium cold plasma densities and temperatures to search for repeatable patterns. These patterns are used to gain insights into the physical processes taking place. An early combination of regional empirical models into a global empirical model of models was developed [170] to enable a more system-level approach to understanding the magnetosphere.

Other global empirical models have been developed to gain physical insight into plasmaspheric erosion [171], plasmapause location [172], equatorial mass density [173], and electron temperature [174]. These and other advancements using the intuitive empirical modeling approach continue to offer a level of controlled data interrogation not otherwise available for probing the magnetospheric system.

Machine Learning (ML) techniques offer another method of developing empirical models. ML techniques have advanced significantly over the past decade because of three factors: enormously increased volumes of data, improved algorithms, and more powerful computation hardware. ML techniques are effective at dealing with highly complex and nonlinear relationships, which are common in magnetospheric physics.

Using ML, PILOT constellation data can be used to construct a series of models for total density (n_e), ion composition (H^+, He^+, O^+), high energy electron flux, and magnetic fields (B). The completed models return global spatial- and history-dependent values for these quantities as a function of upstream solar wind conditions and geomagnetic indices. Similar models were used to discover previously unknown physics related to erosion and refilling of the plasmasphere and plasmaspheric interaction with the radiation belts [175, 176, 177, 178, 179, 180, 181].

ML models can provide reconstructed distributions not only in the region of space immediately covered by PILOT (§D.1), but also in PILOT's weakly covered regions. Therefore, ML-based models can contribute strongly to achieving PILOT science objectives 1 and 2 (§2.2), focused on global mass and energy transport. Also, ML-based models can be compared to, and act as validation for, physics-based numerical simulations (e.g. IPE model [132]) to identify key physical processes that may be missing from physics-based models.

E.3.2 Super Resolution Imaging

Combining Deep Learning-based Super Resolution (DLSR) techniques with PILOT's unique combination of measurements allows ML empirical modeling of density evolution on scales smaller than the mission concept baseline $\sim 0.5\ R_E$ spatial resolution. DLSR techniques can map PILOT radio tomographic images to higher resolution based on embedded in-situ data or simulation information [182, 183, 184]. The power of DLSR models has been demonstrated in various real-world applications including space physics [185] and cosmology [186] (Figure E.1). DLSR techniques can also be used to generate enhanced resolution maps of other PILOT constellation measurements such as electron fluxes, and magnetic field perturbations. Enhanced-resolution maps help address all three PILOT science objectives.

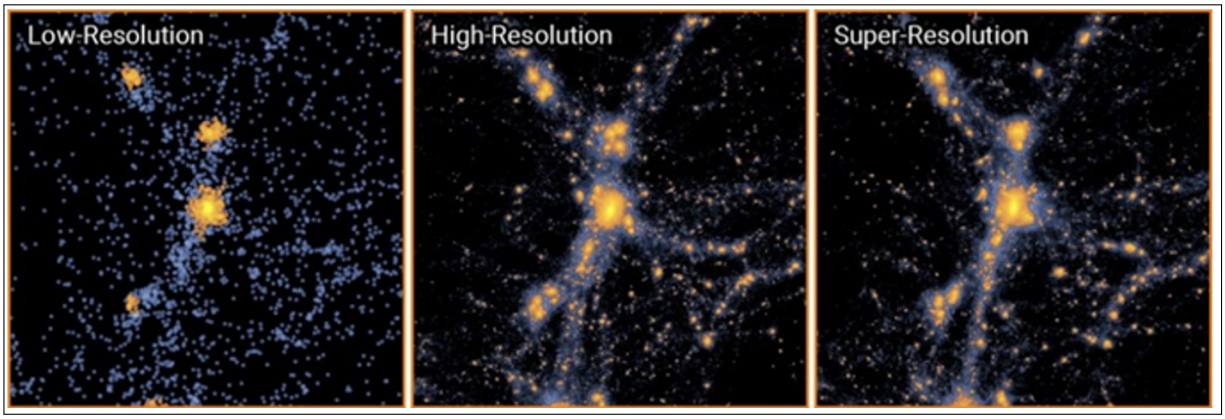

Figure E.1: *Example of using Deep Learning-based Super Resolution to enhance the resolution of a cosmological image [186].*

E.3.3 Stereo EUV Imaging

PILOT EUV imaging provides a meridional view of ions in the plasmasphere. In the past, inversion methods have been used to estimate the helium ion density from the IMAGE/EUV data [187, 188, 189]. More recently, data quality and accuracy of these inversions have been improved by ML-based methods, including Bayesian approaches and Kalman filters [157, 158].

Advanced ML techniques can further improve the interpretation of PILOT EUV images. Image denoising can be easily accomplished with deep-learning-based image denoising [190]. DLSR techniques can boost EUV image resolution enabling the study of fine structures in the meridional plasmasphere. Plasma density obtained from three-dimensional neural-network-based models (DEN2D and DEN3D [178]) can be used to provide a baseline and initial condition for inversion of EUV images. Most importantly, deep learning models can be developed to take raw images from the two outer PILOT PlasmaSat vantage points and use stereoscopic techniques to estimate the 3D distribution of ions in the plasmasphere.

E.3.4 Physics-Based (PB) Modeling

PB modeling uses mathematical models of plasma and fields in the magnetosphere to predict their evolution in time and space in response to solar-wind-magnetosphere interactions. Physics-based (PB) models are important to place PILOT measurements in a global context, achieve new scientific understanding, and maximize scientific return.

For the PILOT mission concept, PB modeling provides context outside the region covered by PILOT measurements at any given time, and enables investigations of causality in mass and energy flow. As one example, comparing PB model-run results, with different physical processes turned on and off, with PILOT observations can diagnose the key magnetosphere-ionosphere coupling processes affected by cold plasma. PB modeling is poised to investigate a range of phenomena targeted by PILOT, such as plasmaspheric refilling (SQ 1a) [28, 191], plasmaspheric erosion (SQ 1b) (e.g. [192]), plasmaspheric wind and interchange instability (SQ 2a) [21], the impact of cold plasma on dayside magnetic reconnection by using multi-fluid MHD models (SQ 2b) (e.g. [193]).

PILOT data can bring closure to outstanding challenges in existing PB models of cold plasma and their coupling to other plasma populations. One current challenge is that current models have inadequate representation of the impact of cold plasma on wave-particle interactions. This physical process is targeted by SQ 3c. Large-scale kinetic models like RAM-SCB (e.g., [194, 195]) can simulate the growth/damping of major plasma waves (e.g., EMIC, whistler-mode waves) in the inner magnetosphere by the anisotropic ring current ion and electron distributions, but model outputs are strongly determined by the distribution of cold plasma, usually simulated with coupled plasmasphere models (e.g. [196]). PILOT provides the necessary measurements of cold plasma and in-situ observations of plasma waves to enable ground-breaking model validation.

An additional major PB challenge is that insufficient data currently exist, for particles in the energy range from 1 eV to 100 eV with accurate mass description (warm plasma cloak, SQ 2a) [197], to enable accurate PB modeling of these populations. PILOT data with sufficient energy and mass coverage can enable the development of entirely new PB large-scale numerical modeling capabilities for particles at these energies.

F Science Question Detail

This appendix provides detailed information on each PILOT science question, including context about the importance of the question, the current state of knowledge surrounding the question, and new physics accessible by PILOT.

Science Question 1a

How is the plasmasphere refilled from ionospheric sources?

Context: When atmospheric gases are ionized, by solar radiation or electron bombardment, electromagnetic interaction with the solar wind magnetic field causes them to flow out of the ionosphere (e.g., [198, 199, 200]). Earth's planetary magnetic field traps much of this plasma in a region known as the plasmasphere, preventing it from escaping directly to the solar wind. During geomagnetic storms, a fraction of the mass held in this reservoir is forced into the solar wind and lost. Ionospheric outflow then refills the plasmaspheric reservoir and the process repeats.

After more than 50 years of research, fundamental questions concerning the physics of plasmaspheric refilling remain unanswered. The observations required to address these questions do not yet exist [29]. In this observational void, gaps in our basic knowledge persist: What causes refilling rates to vary by orders of magnitude? Why is the amount of mass trapped by the magnetosphere only weakly correlated with the polar outflow rates [191]? What fundamental plasma processes are responsible for trapping new ions in the plasmasphere torus [21, 201]?

Current Knowledge: Ionospheric outflow into the inner magnetosphere has been measured from L=1.75 to L=6.6. Generally, refilling rates increase with radius until the outer plasmasphere, then they start to decrease [29]. However, intense variability exists within this general behavior. For $2.5 \leq L \leq 4.5$ refilling rates range from 4 to 800 cm^{-3} day^{-1} [22, 23, 24, 25, 26, 27, 28, 29].

At geosynchronous orbit quiet-time refilling rates range from as little as $\sim$ 0.6 cm^{-3} day^{-1} [202] to as much as 50 cm^{-3} day^{-1} [203], following a two-step refilling process [202, 204, 205]. In stark contrast, long-lived plasmaspheric plumes were discovered during active-time events at geosynchronous orbit that could only persist if fueled by an estimated order of magnitude greater refilling rates of 100 to 500 cm^{-3} day^{-1} [206].

The abundance of He^+ changes during refilling, suggesting that refilling rates may be mass and density dependent [30]. Also, storm-time localized heating in the topside ionosphere may be a significant influence on refilling outflow [207]. Ion heating by low frequency waves near the magnetic equator may also act to isotropize outflowing ionospheric ions [16, 17, 18, 19, 20].

Escape of O^+ and other heavy ions requires heating, via energy inputs from the magnetosphere, in the polar cusp or the nightside auroral zone [31, 32, 33, 34, 35]. Yet, due to a dearth of observations, basic knowledge is lacking about the formation of the dense O^+ torus in the outer plasmasphere and trough. Further, while the oxygen torus was originally identified as originating from the local ionosphere near the magnetic equator, it could be generated in part or in total from high latitude as the low energy portion of the warm

plasma cloak [197].

Physics Discovery Enabled by PILOT: Key refilling questions remain after more than 50 years of research. How does the plasmasphere refill? Where do the ions that participate in refilling come from? How does the dense oxygen torus form? What role does ion mass play in refilling dynamics? What physical processes are involved, when, and where are they most important?

These questions can only be answered with multi-scale measurements such as provided by PILOT (Figure 2.1). In-situ and radio tomographic measurements of plasma density, composition, and magnetic field are essential in the vicinity of the magnetic equator, where field aligned ions are converted into trapped isotropic distributions during the refilling process. H^+, He^+, and O^+ densities, temperatures, and distribution functions must be measured to quantify refilling physics as a function of ion mass. At the same time, global meridional EUV-He measurements quantify the field-aligned distribution and flow of He^+ (which can also act as a proxy for H^+). These distributions and flows are essential to determine whether near-equatorial shocks play a role in early-stage refilling [208].

Observations during at least ten refilling events are required to establish the pattern of physical processes acting from early- to late-time refilling and determine how that pattern changes across L-shells. Measurements must also identify the low energy portion of the warm plasma cloak in the nightside refilling region, and whether this population interacts with the outflowing ionospheric ions to become part of the quiet-time isotropic plasmaspheric population. All in-situ observations must be coupled with EUV global meridional measurements that provide situational context, as well as the quantitative erosion and refilling plasmaspheric state that is required to interpret in-situ measurements.

In-situ O^+ ion observations must occur simultaneously with EUV global meridional imaging of O^+ to determine the extent to which O^+ torus ions are supplied from the ionosphere, by cusp outflow, or directly from the auroral zone [31, 32, 35]. Imaging the O^+ torus enables its basic morphology to be quantified, including its symmetry (or lack thereof) in MLT, its latitudinal extent, and what processes control these attributes [34, 209, 210, 211].

Science Question 1b

By what process(es) and to what extent, does plasmaspheric mass return to the ionosphere or neutral exosphere?

Context: A full accounting of mass flow between the ionosphere and magnetosphere requires determining what processes, and to what extent, plasmaspheric mass returns to the ionosphere or neutral exosphere. In the absence of sunlight, low-altitude recombination reduces ion pressure gradients, which is expected to cause downward transport [29, 38], allowing nightside flux tubes to return plasmaspheric mass to the ionosphere. It is not known when, where, or how this inflow process occurs. It is also not known the extent to which charge exchange with the exosphere has a significant effect on magnetospheric cold plasma populations.

Current Knowledge: The relative mass remaining inside the eroded plasmapause during three moderate erosion events in 2001 was examined using remote IMAGE EUV

observations [29] and compared those to previous in-situ measurements [22, 26, 27, 212, 213, 214, 215, 216]. Plasmaspheric content was lost from well inside the eroded plasmapause for the three events, with interior plasmaspheric mass content reduced to between 55%-75% (Figure F.1). Though loss by erosion of the outer plasmasphere has been widely reported and attributed to convection or centrifugal interchange [201], the mechanism for losses interior to the plasmapause is simply unknown. One hypothesis is that the interior loss is due to downward flow along magnetic field lines, but no measurements exist to definitively prove this.

Physics Discovery Enabled by PILOT: Robust in-situ measurement of ion transport along and transverse to magnetic field lines during plasmasphere erosion events is needed to trace this plasma transport. Simultaneous 2D near-equatorial total plasma density imaging, meridional EUV imaging, and in-situ PILOT measurements can directly quantify the overall loss of inner plasmaspheric plasma inward of the eroded plasmapause boundary. At the same time, quantification of outward transport of plasma outside of the eroded plasmapause (see SQ 2a, 2b), together with any measured outward flux of cold plasma inside of that boundary, can account for excess external escape or erosion of plasma into the plasmaspheric plume [206].

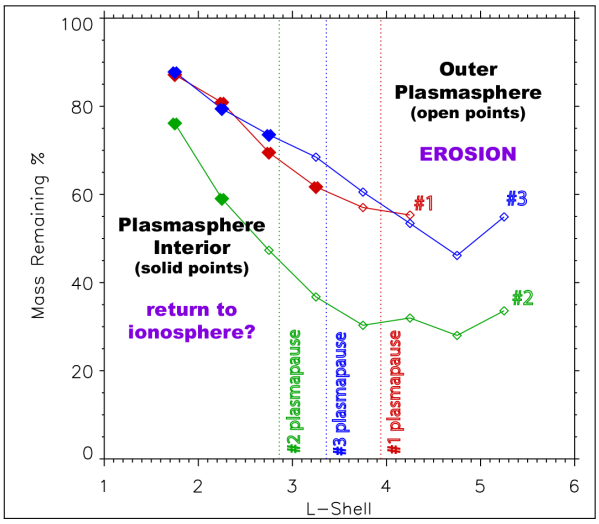

Figure F.1: *Mass loss from the plasmaspheric interior [29]*

At least 10 erosion events are needed, with in-situ measurements at low latitudes at L-shells inside of the eventual eroded plasmapause from a time prior to the onset of erosion to the time of maximum erosion of the plasmapause. The combination of in-situ and remote-sensing measurements identify the transport pathways for this interior plasmaspheric plasma loss, the mechanisms for that loss, and quantity of plasma lost during erosion events as a function of disturbance conditions.

Science Question 2a

What are the key pathways for transport of plasma mass through and out of the inner magnetosphere?

Context: Much of the rich physics in the geospace system lives within the transport, coupling, and feedback between regions. Cross-scale measurements from PILOT enable study of the individual regions as well as the transport of material between them and how they couple together as an interwoven ecosystem.

Current Knowledge: A plasmaspheric plume is a dramatic structure formed by plasma transport, where the density can be 50-100 times greater than adjacent regions. In local time, a plume can spatially span many Earth radii (5 R_E or more) or be narrow

($< 1\ R_E$). Radially, a plume typically detaches from the plasmasphere at a radial distance from Earth of several R_E ($\sim 4-5\ R_E$) and can extend to the dayside magnetopause. This critical region of separation is within the spatial range of the radio tomography and imaging capabilities of PILOT. A plume forms over the course of tens of minutes and evolves over the course of tens of hours, all within the temporal resolution of PILOT. Dense plumes serve as an energy reservoir for local instabilities [217] and plasma waves which couple to the radiation belts [99, 218]. Measurements from PILOT enable understanding in how these waves form, their spatial extent, and their impact on the radiation belts.

Physics Discovery Enabled by PILOT: A very basic understanding of how a plasmaspheric plume forms and maintains itself is lacking. A plume can be short lived (hours) or last for weeks [219, 220]. The physics that drives the necessary refilling to sustain this structure, and quantification of the appropriate refilling rates, both remain poorly determined [44, 221]. Numerical models have supported refilling research but remain poorly constrained due to a lack of simultaneous density measurements over a broad spatial region (several MLT and L-shells). Radio tomography measurements provide the missing information needed to quantify refilling rates and determine the critical spatial and temporal variability.

The warm plasma cloak is a population outside the plasmasphere transported in from the magnetotail, rich with oxygen [197, 222, 223]. Many key questions remain unanswered about the transport and coupling of this population. What mechanism(s) is responsible for heating the cloak plasma [224]? Does the plasma cloak play a dominant role in filling the dayside magnetosphere with mass density [43]? Is the cloak a candidate for nightside plasmasphere refilling [44]? A combination of measurements from PILOT answers these questions. O^+ and He^+ imaging quantify the large-scale distribution and evolution of density and composition with time, which can address questions of relative transport and contribution in different regions of the magnetosphere. Micro- and meso-scale heating mechanisms are evaluated and probed through in-situ measurements.

Flow channels through the subauroral regions or SAPS are paths of transport that can carry significant material and strong local electric fields (several mV/m [225, 226]). Spatially they are latitudinally localized (0.8 to 1.5 R_E in the equatorial plane) and typically located equatorward of $\sim 60^o$ invariant latitude ($L = 4$), and extending from the dusk to early morning MLT sectors during geomagnetically disturbed times [227]. Major gaps remain in understanding how this structure couples to the magnetosphere. How do SAPS contribute to the structuring of the plasmapause or detached structures (50 km - thousands of km in size) [94, 228, 229]? What role do SAPS play in driving erosion? How do SAPS electric fields drive convection in the ionosphere and magnetospheric and how does this impact the magnetosphere?

Science Question 2b

What are the mechanisms of plasma mass transport and their drivers?

Context: Once cold, ionospheric plasma mass reaches the plasmasphere, it is distributed and transported to other magnetospheric regions. It can go sunward to the dayside magnetopause and participate in reconnection, or it can be diverted to the flanks and

travel anti-sunward to load the plasmasheet. What determines where the cold plasma goes? What fundamental processes dictate the plasma mass distribution and drive mass transport? Addressing these questions requires tracking cold plasma bulk motion at convective velocity $(\vec{E} \times \vec{B})/B^2$ across multiple scale sizes, from global to local.

Current state of knowledge: While the geomagnetic field is relatively well-known, the electric (E) field is more elusive. E-fields are central to the coupling between the solar wind, the magnetosphere, and the Ionosphere-Thermosphere (IT) system (including the neutral winds). Thus, they are highly variable, even very close to Earth, and their measurement requires dedicated instruments. This makes their description essential yet uncertain even after decades of studies [109].

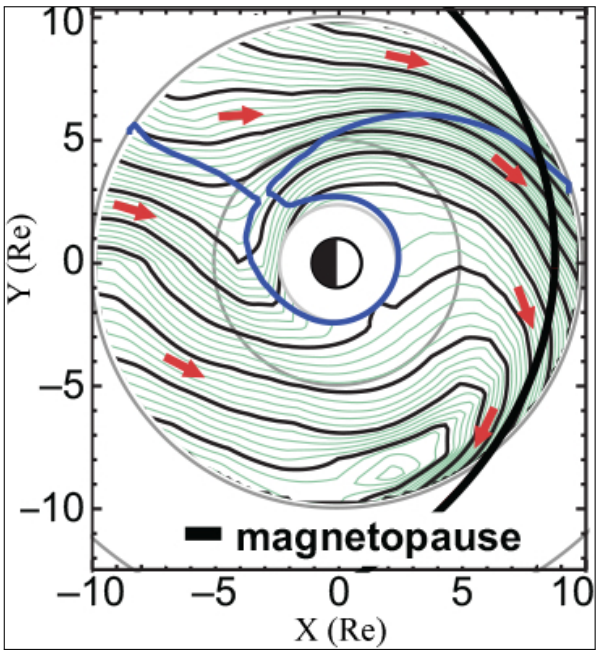

Figure F.2: *Empirically-modeled electrostatic cold plasma pathways in the Earth's corotating frame, from [45].*

Single-point in-situ E-field measurements have been leveraged to create empirical models, i.e. statistical maps. However, the variability of the resulting cold plasma pathways remains to be determined. Indeed, to tackle the uncertainty in the dataset of E-field measurements (due to both measurement uncertainty and natural variability), additional assumptions have been introduced. For example, empirical models usually impose an electrostatic assumption ($\nabla \times E = 0$). Although it facilitates visualization of the convective pathways (Figure F.2), the validity of this assumption is questionable, in particular for $L > 5$. It is also difficult to quantify the extent to which statistical models can accurately describe the dynamic evolution of any given event.

Moreover, statistical data analysis blurs/obscures small scale features and/or highly structured features naturally present in the database. These features include SAPSs and the SAIDs that significantly alter plasma flow paths in the duskside region ([46, 47, 48]. While statistical experimental models for SAPS exist [230], how they connect to the global topology of the electric fields, thus, how they organize plasma mass transport remains unclear. What physical processes determine the characteristics (e.g., strength, location, duration, motion, etc.) of the SAPS and SAIDs is also unclear.

Small-scale features are definitely present in the global electric field topology, but their role in plasma transport remains to be determined. For instance, to what extent is plasmasphere erosion governed by global-scale electric fields vs local dynamics (which may involve local E-field structure and instabilities)? Observations from IMAGE EUV instruments revealed the existence of many small scale structures (including notches, crenulations, fingers and shoulders). The tracking of their time evolution was leveraged to extract info on the average spatial variability of the large-scale DC electric field [231]. Yet, statistical models

for the electric field dynamics have seldom accurately reproduced such features [48].

Physics Discovery Enabled by PILOT: Our current understanding of cold plasma mass transport relies on heavily smoothed statistical maps of electrostatic potentials [45], and ad hoc modular models for SAPS [48, 230]. These models are unsuccessful at reproducing many plasmaspheric structures observed by IMAGE EUV instruments (including notches, crenulations, fingers and shoulders [49], and the pathways of mass transport through the system are very uncertain [50, 51, 52].

PILOT measurements enable definitive cross-scale tracking of cold plasma bulk motion over a broad region of the inner magnetosphere. Radio tomographic total density images in the equatorial plane provide rapidly refreshing observations of the cross-L transport of mesoscale spatial structures. These images cover a region spanning $\sim$ 3 L-shell in radial distance and $\sim$ 3.5 MLT in azimuthal distance. Embedded in this 2D image plane, in-situ point observations of DC-coupled electric and magnetic fields, along with measurements of cold plasma electron, proton, and heavy ion distribution functions, provide ground truth point-sampling of the cold plasma bulk motion and the electric fields that drive it. Simultaneous meridional EUV imaging quantifies transport out of the equatorial plane. This set of measurements directly and unequivocally determines the mechanisms and drivers of cold plasma mass transport.

Science Question 3a

To what degree does the dynamic distribution of plasma mass regulate the expression of Alfvén waves?

Context: The Alfvén speed determines the rate of information transfer via magnetic field between any two points in the magnetosphere. It determines the expression (amplitudes, occurrence, propagating or resonant mode) of ULF waves, which carry the magnetic information that enables magnetosphere-ionosphere coupling [53], magnetosphere-solar wind coupling [54], as well as radiation belt energization, loss, and radial diffusion [55, 56, 57].

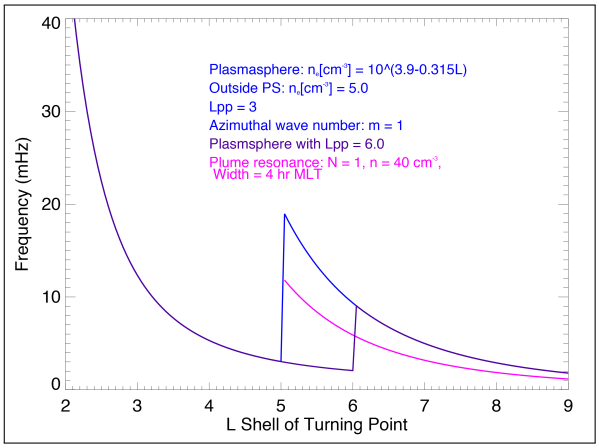

Figure F.3: *Simple analytic model for ULF wave turning points.*

Current Knowledge: The inner magnetosphere supports various ULF modes, including those that carry energy Earthward from the magnetotail and from the solarwind/magnetosphere interface [232]. These energy inputs can either drive propagating waves, or drive field line resonances and cavity modes [233, 234, 235, 236, 237]. Energy flux transport via these modes, and energy exchange between these modes is critically sensitive to the Alfvén speed.

Modeling has shown that the spatial distribution of cold plasma should significantly alter the ULF wave power distribution, both radially and in MLT. It should also determine

the location of the ULF wave radial turning point: the location where the compressional (fast mode) radial wavenumber goes to zero and beyond which the compressional waves transfer energy into the local field line resonance [238].

Figure F.3 shows the radial location of ULF turning points for various wave frequencies, assuming a radial density profile from an analytic model [239], and a dipole magnetic field. For a given turning point profile, higher frequencies reach lower L values than lower frequencies.

Case and statistical studies show that the plasmaspheric plume also strongly shapes the ULF wave power distribution, trapping and ducting ULF waves [240, 241, 242]. Also, the higher plasma density inside the plume allows radially propagating compressive waves to propagate to lower L values.

Physics Discovery Enabled by PILOT: PILOT data enable a direct test of how the the expression of ULF waves responds to evolving cold plasma density conditions. By measuring total plasma mass, composition, and magnetic field across broad swaths of local time and radial distance, PILOT creates a rapidly refreshing image of the magnetospheric Alfvén-speed in the ecliptic plane, with directly measured ULF wave properties superimposed.

Science Question 3b

By what mechanisms and to what extent does the distribution of plasma mass govern the dynamics of meso-scale plasma flows that reach the inner magnetosphere?

Context: The Dungey cycle [63] describes the fundamental flow of magnetic energy and flux through Earth's solar-wind driven magnetosphere. A key portion of the Dungey cycle involves the return flow of magnetic field and plasma Earthward from the magnetotail. Numerous studies have established that these return flows take the form of meso-scale plasma flows, often called Bursty Bulk Flows (BBFs) [58, 59, 60, 61, 62]. BBFs are known to be responsible for much of the energy transport from the Earth's magnetotail into the inner magnetosphere (e.g., [74] and references therein) and known to drive ionospheric energy deposition, as demonstrated by their association with specific auroral forms (e.g., [67, 68, 70, 71]).

Fundamental aspects of the Earthward flow physics cannot be determined using single-point or serendipitous multi-point in-situ measurements. A lack of combined in-situ and meso-scale measurements prevents quantitative evaluation of how the energy and mass carried by these flows is redistributed through the inner magnetosphere as they slow and stop [64, 65, 66]. Evidence from multi-spacecraft case studies [77] supports the long-suspected (e.g., [74, 75] and references therein) connection between BBFs and the particle injections that supply the ring current [243], as well as radiation belt source and seed particles [57]. However, without combined in-situ and spatial plasma density distribution measurements, this connection cannot be definitively validated.

Mounting evidence indicates that the spatial distribution of cold plasma in the inner magnetosphere determines the final deceleration of Earthward plasma flows (e.g., [72, 73, 76, 78]), thereby regulating the deposition of their remaining flow energy into the

inner magnetosphere, and their ability to transport plasma sheet particles into the inner magnetosphere [79]. Further, the Poynting flux generated during BBF breaking is implicated in the energization of ions in the ionosphere and subsequent production of low-energy ion outflow that contributes to re-population of the outer plasmasphere [80].

By combining distributed in-situ measurements with radio tomographic imaging of Earthward plasma flows, the PILOT mission can at last quantify the physical processes underlying this critical mass and energy flow pathway that links magnetotail and inner magnetospheric dynamics.

Current Knowledge: The evolution of BBFs is well understood $>\sim 8R_E$ from Earth. BBFs originate in the magnetotail beyond $\sim 15R_E$, generated by magnetic reconnection events that are localized in the GSM Y (Geocentric Solar Magnetospheric) direction [61, 244, 245]. They are often accompanied by dipolarization of the Earth's magnetic field (e.g. [113]. BBF earthward flow velocities can reach $\sim$ 1000 km/s in the magnetotail, and BBFs carry significant energy flux, both in terms of ram energy and Poynting flux [246].

BBF flow velocities slow to the order of 100 km/s as they travel from $\sim 12R_E$ to $\sim 8R_E$ and the Earth's magnetic field becomes stronger. This region, called the BBF braking region [65], displays strong turbulence, wherein ions and electrons are energized and Alfvén waves are launched toward Earth's ionosphere [247].

The fate of BBFs is not well understood Earthward of $\sim 8R_E$, where their flow speed is dramatically reduced [64, 66]. One of the many unknowns is how BBFs drive injections of energetic particles and heavy ions into the inner magnetosphere [74, 243, 248, 249].

Figure F.4 shows a single-point in-situ measurement of a BBF flow burst that has penetrated to $\sim 9R_E$, observed by the THEMIS A satellite [113]. Panels (a) and (b) show ion and electron flux (respectively) as a function of energy. Panels (c), (d), (e), and (f) show, respectively, magnetic field (B), electric field (E), Poynting flux (S) and ion velocity (V). Figure F.4g indicates disturbed vortex flow, often seen at the leading edge of a BBF. Clear B fluctuations and dipolarization are observed ($|B_x|$ decreases, B_z increases). E fluctuations (Figure F.4d) are intense and may be responsible for accelerated ions (Figure F.4a) and electrons (Figure F.4b). S is primarily field-aligned (Figure F.4e, black trace) and negative, indicating significant energy flow toward Earth [246]. The intense Earthward-directed Poynting flux is in concert with auroral brightening associated with BBFs [70]. Another important BBF characteristic is variation in total plasma density (N_e, not shown) that can be as high as 50%, on spatial scales of an R_E (e.g., [61, 84, 250]). These features are characteristic of BBFs in the braking region [247].

Physics Discovery Enabled by PILOT: A BBF that reaches the inner magnetosphere can be simultaneously measured in-situ and imaged by PILOT radio tomography, due to its associated density structure. By directly imaging the evolving BBF N_e perturbation ($\sim 1R_E$ scale size), PILOT can define the currently missing density spatial distribution context for in-situ observations.

Figure F.4 shows simulated PILOT observations of a decelerated BBF encountering the plasmasphere. The figure incorporates three radio tomography-reconstructed images of a numerically modeled BBF density structure and plasmasphere. The radio tomography reconstruction (§D.1) was determined solely from radio tomography and in-situ N_e measurements from simulated spacecraft in a simulated plasmaspheric density distribution

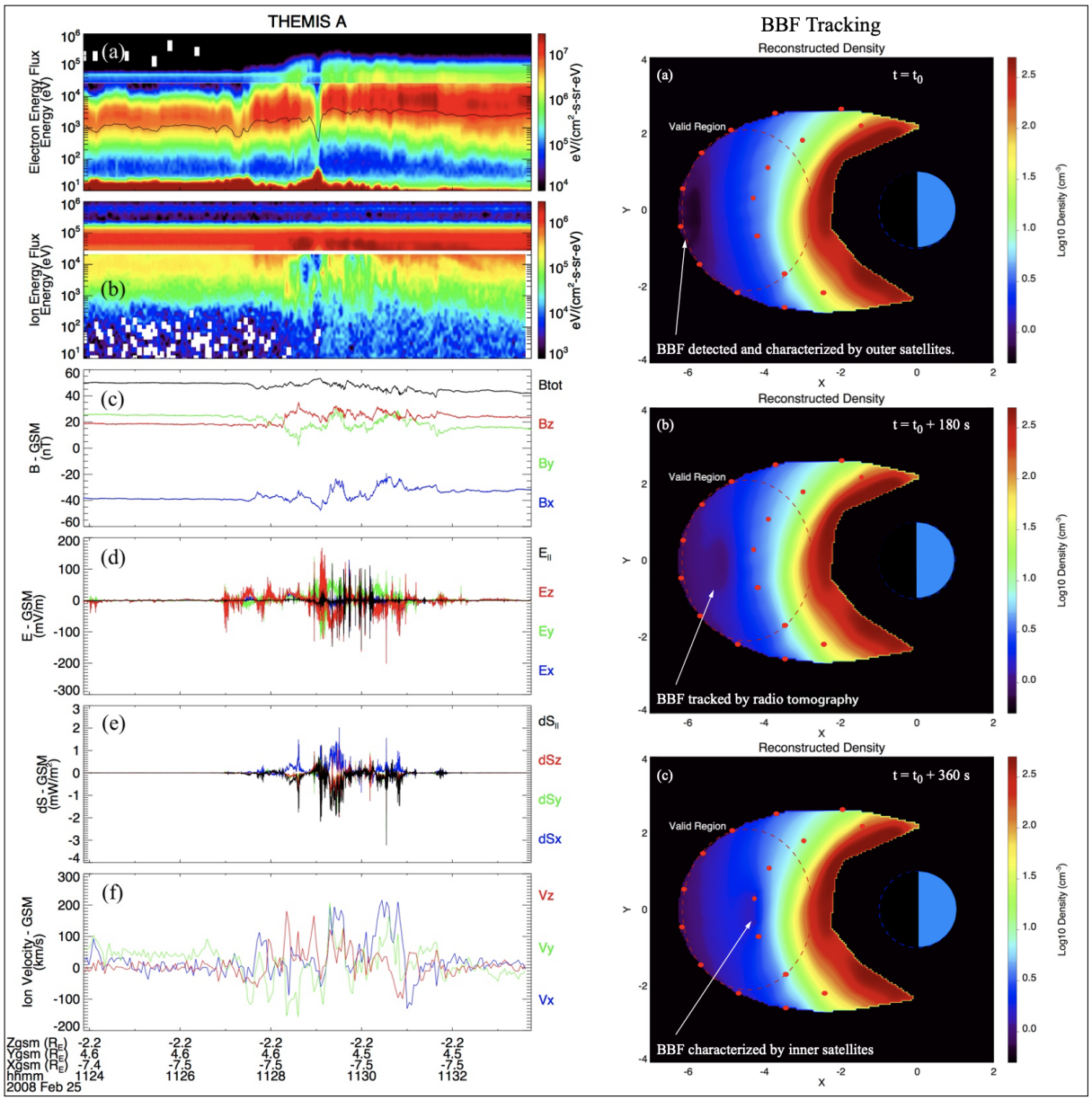

Figure F.4: *(left) In-situ measurement of a BBF flow burst that reached* $\sim 9R_E$*. (right) PILOT can track Earthward plasma flows through the inner magnetosphere.*

(from the IPE model [132]) at the locations indicated by red dots. A $0.5cm^{-3}$ Gaussian N_e depletion is shown (spatial extent $0.5R_E$ radial, $2R_E$ azimuthal), traveling Earthward at 35 km/s, such that it covers the distance from $6.25R_E$ to $4.25R_E$ in $\sim$ 6 minutes. About 36 images can be reconstructed for this event, using 10 s radio tomography image cadence. Figure F.4 shows three radio tomography images, each 3 minutes apart. As the BBF crosses 6.25 RE (Figure F.4a) outer-orbit spacecraft detect, in situ, the N_e depletion, B perturbation, and energetic electron enhancements. PILOT radio tomography imaging tracks the density perturbation to $\sim 4.25R_E$ (Figure F.4b). As the N_e depletion reaches $4.25R_E$ (Figure F.4c) at inner orbit spacecraft detect the same in-situ quantities as the outer-orbit s/c.

Combined in-situ and radio tomographic observations similar to the simulated observations shown can (i) quantify, via Earthward flow deceleration, the transfer of flow energy into the inner magnetosphere across scale sizes, and its regulation by cold plasma, (ii) definitively establish the relationship between meso-scale Earthward plasma flows and particle injections into the inner magnetosphere, and (iii) quantitatively connect Earthward plasma flow breaking with ionospheric outflows as observed by PILOT EUV imaging.

Science Question 3c

To what extent does the dynamic distribution of plasma mass in the magnetosphere determine the expression of wave-particle interactions that energize, de-energize, and precipitate energetic plasma?

Context: Plasma waves are a fundamental mechanism of particle transport (e.g., [251] and references therein) and energy transfer [85, 86] between plasma particle populations in the inner magnetosphere. For example, plasma waves energize particles in the Earth's radiation belts, and scatter them into the atmosphere (e.g., [57, 86] and references therein).

Cold plasma density strongly determines the efficiency of the relevant wave-particle interactions (e.g., [87, 88]), and may control electron acceleration to multi-MeV energies [78]. Our knowledge of meso- and macro-scale extent of these processes in the inner magnetosphere currently relies on an elaborate chain of complex modeling and statistical inference (e.g., [4, 91, 92, 93, 94, 95, 96]). Predictions resulting from this chain often strongly disagree with measurements for any individual geomagnetic driving event [97, 98], blurring our picture of which physical processes are most relevant under which geomagnetic conditions.

PILOT is uniquely capable of placing in-situ measurements of plasma waves and particles into the context of the meso-scale distribution of plasma density (determined by radio tomography) and magnetic field (determined by the array of Radiosats). In this way, PILOT measurements can enable the first quantitative evaluation of whether our current statistical descriptions of wave growth and wave-particle energy transfer in the inner magnetosphere are truly capturing the most relevant wave-particle interaction processes for any given geomagnetic event.

Current Knowledge: Some of the plasma wave modes most effective at sculpting particle populations in the inner magnetosphere are Very Low Frequency (VLF) waves such as chorus and hiss (e.g., [85, 86, 253]), and electromagnetic ion cyclotron (EMIC) waves (e.g., [254, 255, 256]). The contribution of ultra low frequency (ULF) waves is discussed

under the description of SQ 3a.

Ambient plasma density, dominated by cold plasma in the inner magnetosphere, is well known to regulate the expression (growth and damping) of these wave modes (e.g., [87, 257, 258]). Because of this physics, the plasmapause acts as a sharp boundary between hiss (radiation-belt loss) and chorus (radiation-belt energization) [86, 147, 259], making it a critical boundary for radiation belt dynamics [260], auroral precipitation [94] and ionospheric heating [261].

Further, the generation and propagation characteristics of EMIC waves depend strongly on cold plasma density and ion composition [89, 90]. In a multi-component plasma, EMIC waves appear in several frequency bands separated by the cyclotron frequencies of individual ion species (wider gaps are correlated with higher heavy ion densities). Global-scale numerical modeling studies have shown that the source regions of EMIC instability overlap with regions of anisotropic ring current protons and plasmaspheric drainage plumes [262, 263]. Simulated global images of proton precipitation matched well the temporal and spatial evolution of IMAGE observations of subauroral proton arcs, indicating that cyclotron resonant wave-particle interactions are a viable mechanism for their generation [264]. Observationally, however, the dependence of EMIC waves on cold plasma density and/or density gradients is controversial [99, 100, 265].

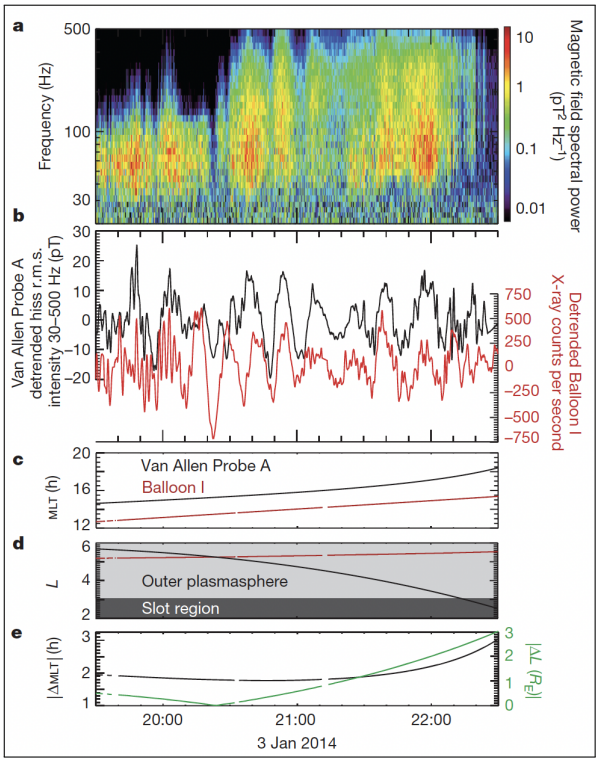

Figure F.5: *Serendipitous observation of meso-scale plasma density variation regulating plasma wave expression and particle precipitation into the ionosphere [252].*

Meso-scale and global scale manifestations of plasma wave regulation by cold plasma have been glimpsed by comparing in-situ observations in the magnetosphere with distributed observations in the stratosphere. It was demonstrated that variation in local magnetospheric cold plasma density near 3 < L-shell < 6 can modulate the amplitude of plasmaspheric hiss plasma waves, which in turn can modulate the precipitation of electrons as observed by an array of balloon-borne x-ray detectors [252]. Figure F.5 (from [252]) shows how the modulation of hiss plasma waves (Figure F.5a,b) corresponds closely with the modulation of x-ray flux from precipitating electrons (Figure F.5b) over a wide range of radial distances (Figure F.5d,e).

Physics Discovery Enabled by PILOT: PILOT's direct and rapid (∼10 s) observations of plasma density by radio tomography, and distributed observations of magnetic field over a broad spatial region of the inner magnetosphere, create meso-scale maps of wave growth conditions.

Detailed in-situ point observations of plasma waves and particles by PILOT PlasmaSats provide anchor points where wave properties and wave-particle interactions, inferred from radio tomographic measurements of the density distribution, can be directly evaluated. By extrapolating observations at these anchor points to the full meso-scale maps, PILOT data can be used to quantitative evaluate the accuracy of our current statistical descriptions of wave growth and wave-particle energy transfer. In this way, PILOT observations access a regime currently available only in simulations [62, 79].

G Mission Overview Detail

G.1 Key Architecture and Mission Trades

There are seven key trades that drive PILOT mission architecture and mission design (Table G.1). PILOT key trades are:

Disposal orbit propulsion type: Because of the delta-V required to dispose of the spacecraft at end-of-mission, propulsion systems with the capability of providing the required delta-V were examined. The primary considerations were an all-hydrazine system, an all-electric propulsion system, or a hybrid hydrazine-electric propulsion system. A solid-propellant rocket system was considered, but ultimately dismissed due to low TRL under long duration (>3 years) radiation exposure of the solid fuel. All-electric propulsion systems have negative impacts during the mission CONOPS most notably regarding vehicle station keeping and the thruster impacts on electric field, magnetic field, and particle measurements. Mission ops would need to accommodate instrument duty cycling during electric propulsive maneuvers. A hybrid (chemical + electric propulsion) solution was considered, with electric propulsion used for orbit insertion and disposal. The complexity of a hybrid solution combined with the low heritage of electric propulsion systems that sit dormant for the full mission life made the hybrid solution less viable. The team selected an all-chemical solution with a high heritage hydrazine propulsion system.

Number of launches: A single launch transporting all spacecraft to both orbits is desired to minimize cost. Per NASA guidance, this study is limited to those LVs currently on the NLS-II contract. After researching the performance capability of the launch vehicles currently in the NLS II, it was determined that two launch vehicles are required (one launch for each orbit – inner/outer). Our analysis was confirmed with direct conversations with SpaceX and Blue Origin. It should be noted that the SpaceX Starship, which is soon to be

Mission Area	Trade	Rationale	Future Considerations
De-orbit propulsion type	All-hydrazine prop system for orbit raising, station keeping and de-orbit vs. SEP for deorbit	Science measurement integrity, high heritage, only carrying one propulsion system	New propellant types with higher Isp
Number of launches	Two launches on NLS II LV with restartable upper stage vs. multiple launches on smaller LVS	Cost, restriction to current NLS contract	On-ramped Starship
Radiation hardening	Parts selection vs. shielding	Cost, heritage	Instrument-level design architecture
RadioSat Bus	Existing microsat capabilities vs. spacecraft advanced development - radiation, spinning, mass production	Cost, schedule, heritage	Microsat constellation new entrants
PlasmaSat Bus	Existing microsat capabilities vs. spacecraft advanced development - radiation, spinning, mass production	Cost, schedule, heritage	Small s/c new entrants
RT instrument phase delay determination	Two transmitters vs. atomic clock	Cost, heritage	Technology advancements in chip scale atomic clocks
Multi-instrument manufacturing	In-house vs. commercially competed	Cost, schedule, mission assurance requirements	NASA acceptance of commercial manufacturing standards

Table G.1: *PILOT Key Trades*

on-ramped to NLS II, would allow the deployment of all PILOT spacecraft in one launch at significantly reduced cost, especially compared to the cost guidance given for NLS-II LVs.

Radiation hardening: PILOT spacecraft and instruments are subjected to elevated radiation exposure due to the orbits required for the mission. Radiation mitigation may include introduction of rad-hardened parts, additional parts screening, or selective shielding. Fortunately, many bus components already support appropriate radiation tolerance and are utilized where possible. Most PILOT instruments were designed for the relevant radiation environment and use shielding to mitigate radiation effects. For mission concept development, it is desirable to preserve instrument heritage at the cost of heavier payloads. Optimization for radiation tolerance provides an opportunity for the PILOT program to reduce mass in the future.

RadioSat Bus: A plethora of microsat (10 – 100 kg) providers with capability to produce constellations has recently emerged. There are 22 commercial microsatellite platforms providers listed in the latest NASA State-of-the-Art Small Spacecraft Technology, NASA/TP-20210021263 ([103] - Table 2-2). To bound current and future capabilities, a cross-section of mini-sat technology providers was selected, including Blue Canyon Technologies (current), Muon Space (future), and LASP (research). This trade concluded that a healthy supply base exists for minisat innovations to support PILOT constellation development.

PlasmaSat Bus: The decision to leverage existing science instruments in their current form factor resulted in less than optimal payload mass, putting the bus requirements in the smallsat range (§4.2.2). The team looked at current providers and focused on existing capabilities from more established manufacturers to provide spinning platforms, operate in the PILOT radiation environment, and produce multiple spacecraft. Ball Aerospace was selected to develop a reference design due to their experience and existing capabilities.

Two transmitter frequencies vs. atomic clock: The baseline PILOT concept for radio tomography requires two transmission frequencies to ensure an accurate scientific measurement. It is also possible to achieve an accurate measurement with one frequency and an accurate atomic clock that would enable measurement of the exact absolute time of pulse transmission by each RadioSat. This would greatly simplify the RT instrument design. This trade determined that current chip scale atomic clocks, unfortunately, do not have the accuracy and stability ($\sim 1 \times 10^{-12}$ s) to support PILOT science. Timing solutions that would enable this solution do exist but are currently too large and costly to practically implement for PILOT and are not currently designed to the PILOT radiation environment.

Multi-instrument manufacturing: PILOT has several instruments, detectors and hardware components that are needed in significant quantities, which traditional research organizations may not be able to produce. This trade focused on utilizing commercial manufacturers who could more easily produce hardware in mass quantities, and assessing advantages and risks this could involve in terms of cost, schedule and mission assurance requirements. Design by universities and research institutes, with commercial manufacturing approaches can be viable for PILOT and compatible with a Class C mission. This approach has been taken previously on the NOAA COSMIC-2 mission, where the IVM payload was designed at the University of Texas at Dallas, but manufactured at Ball Aerospace to ac-

commodate the large quantity required. Tailored mission assurance requirements can be implemented to leverage the ability to produce hardware using commercial manufacturing standards, with I&T performed to Class C S&MA standards. Development and acceptance of such an approach is critical for NASA to undertake missions involving constellations of satellites like PILOT.

G.2 Mission Requirements

The mission requirements are derived from the STM (Table STM-1, STM-2) and the architecture and mission trades. The mission requirements are shown in Table G.2. Key requirements that drive the mission design are the orbit precession and coverage requirements and spacecraft disposal delta-V.

G.3 Mission Design

The PILOT spacecraft are integrated onto two Falcon Heavy LVs, and launched from Cape Canaveral directly into two coplanar, near equatorial orbits: 1.52 x 4.25 R_E (inner) and 1.1 x 6.25 R_E (outer) Launch vehicle capabilities and margins are shown in Table G.3. After being individually deployed by the LV into a string-of-pearls configuration, the spacecraft use on-board propulsion over the course of a month to achieve the mean anomaly spacing required for science operations. The PILOT constellation of 34 spacecraft is distributed between two coplanar, near-equatorial orbits that overlap to form a radio tomographic imaging plane on the apogee side. In each orbit, the spacecraft are spaced in mean anomaly so that they bunch up near apogee to enhance radio tomographic resolution. The orbits are designed to simultaneously optimize radio tomographic imaging, in-situ observations, and photon imaging in the inner magnetosphere. Both the inner and outer orbits have the same orbital precession rates to ensure that the area between the orbits remains fixed. A trade study was performed to determine an optimal mission design.

This broad trade space was narrowed to sixteen options. To be considered a viable option, orbits were required to have more than 1.5 R_E between apogees (per science requirements, STM-2), have an inner orbit with an apogee less than 4.5 R_E (per science requirements, STM-2), have an outer orbit apogee that remained above 5 R_E for more than 60% of the orbit (to optimize EUV imaging duty cycle), and have a perigee above 400 km (to prevent premature deorbit due to atmospheric drag considerations).

The precession rate chosen for this orbit pair is approximately 0.81 degrees per day for argument of perigee (AoP) and -0.41 degrees per day in RAAN, resulting in an overall orbital precession of 0.41 degrees per day. This results in a full orbital precession through all local times in about 1.7 years. This allows for the mission to precess through all local times almost twice in 3 years. The precession of the orbits at launch (a), after 1.5 years (b), and after 3 years (c), is shown in Figure 4.5. The benefit of a higher AoP precession rate is that it lowers the delta-v cost to deorbit the satellites. However, for orbits with sufficiently high AoP precession rates, outer orbit perigee comes within 400 km.

Setting the radius of the outer orbit's apogee to 6.25 R_E ensured that each satellite in the outer orbit would spend over 50% of the mission above 5 R_E. Based on the relationship between the AoP precession rate and the orbit geometry, the radius of perigee can be extracted once the AoP precession rate and apogee radius are set. Thus, the corresponding

	Mission Requirements	Orbit Design Requirements	Spacecraft Requirement	Ground System Requirement	Operations Requirement
RadioSat Measurements	• ≥ 30 identically-instrumented spacecraft • Near-equatorial orbits, coverage near L=4, 6 • ≥ 24 hr MLT precession in mission lifetime • S/C separation for 0.5 R_E resolution	• Two near-equatorial orbits, apogees near 4, 6 R_E • ≤ 20° MLAT from magnetic equator for ≥ 80% of mission • Disposal ≤ 25 years of EOM • Equal precession rates of inner and outer orbits • Near-equal separation along track near apogee	• Deployable stacers • Position knowledge ≤ 0.05 R_E (1-σ) • Attitude knowledge ≤ 0.1° (1-σ) • Electrostatic cleanliness program • Deployable FGM boom • Magnetic cleanliness program	• X-band compatible • 3 passes/day (outer orbit) • 4 passes/day (inner orbit) • Weekly cmd uplink • Downlink ≥ 0.30 Gb/orbit (inner) • Downlink ≥ 0.36 Gb/orbit (outer) • Bit-rate error ≤ 10^{-6} bps • Science and s/c data to MOC	• Support 3 (outer), 4 (inner) X-band contacts/day • Coordinate s/c-ground uplink/downlink • Uplink command sequences • Capability to command at off-nominal times • Monitor instrument and s/c health at perigee • Monitor capability at off-nominal times • Science data to Science Data Center (SDC)
PlasmaSat Measurements	Mission Requirements	Orbit Design Requirements	Spacecraft Requirement	Ground System Requirement	Operations Requirement
	• EUV data from L-shell ≥ 5 for ≥ 50% of mission • Simultaneous in-situ data near L-shell = 4,6 • Near-equatorial orbits, crossings of L = 4,6 • ≥ 24 MLT precession in mission lifetime • In-situ data in EUV FOV for ≥ 50% of mission	• Outer apogee ≥ 6 R_E • ≤ 20° MLAT from magnetic equator for ≥ 80% of mission • Equal precession rates of inner and outer orbits • Two near-equatorial orbits, apogees near 4, 6 R_E	• Spin period ≤ 15 s • Attitude knowledge ≤ 0.1° (1-σ) • S/C panel potential control • Electrostatic cleanliness • Magnetic cleanliness program • Deployable EFI wire booms • Deployable FGM booms • Deployable SCM booms	• X-band compatible • 3 passes/day (outer orbit) • 4 passes/day (inner orbit) • Weekly cmd uplink • Downlink ≥ 1.40 Gb/orbit (inner) • Downlink ≥ 3.86 Gb/orbit (outer) • Bit-rate error ≤ 10^{-6} bps • Science and s/c data to MOC	• Support 3 (outer), 4 (inner) X-band contacts/day • Coordinate s/c-ground uplink/downlink • Uplink command sequences • Capability to command at off-nominal times • Monitor instrument and s/c health at perigee • Monitor capability at off-nominal times • Science data to Science Data Center (SDC)

Table G.2: *Mission Traceability Matrix: Pilot mission requirements flow from the Science Traceability Matrix, detailing the orbits, delta-V, instrument accommodations, and spacecraft bus requirements.*

Parameter	Value	Units
Orbit Parameters (apogee, perigee, inclination, etc.)	Inner: 1.52x4.25 RE, 0° inc. Outer: 1.10x6.25 RE, 0° inc.	
Mission Lifetime	36	mos
Maximum Eclipse Period	125	min
Launch Site	Cape Canaveral, FL	
Launch #1 RadioSat mass with contingency (includes instruments) - inner orbit	1316.8	kg
Launch #1 PlasmaSat mass with contingency (includes instruments) - inner orbit	575.2	kg
Launch #1 Propellant Mass without contingency	116.64	kg
Launch #1 Propellant contingency	25	%
Launch #1 Propellant Mass with contingency	145.8	kg
Launch #1 Launch Adapter Mass with contingency	422	kg
Launch #1 Total Launch Mass	2314	kg
Launch #1 Launch Vehicle	Falcon Heavy	Type
Launch #1 Launch Vehicle Lift Capability	4300	kg
Launch #1 Launch Vehicle Mass Margin	1986	kg
Launch #1 Launch Vehicle Mass Margin (%)	86%	%
Launch #2 RadioSat mass with contingency (includes instruments) - inner orbit	1152.2	kg
Launch #2 PlasmaSat mass with contingency (includes instruments) - inner orbit	653.6	kg
Launch #2 Propellant Mass without contingency	107.36	kg
Launch #2 Propellant contingency	25	%
Launch #2 Propellant Mass with contingency	134.2	kg
Launch #2 Launch Adapter Mass with contingency	422	kg
Launch #2 Total Launch Mass	2227.8	kg
Launch #2 Launch Vehicle	Falcon Heavy	Type
Launch #2 Launch Vehicle Lift Capability	5300	kg
Launch #2 Launch Vehicle Mass Margin	3072.2	kg
Launch #2 Launch Vehicle Mass Margin (%)	138%	%

Table G.3: *PILOT Launch Vehicle Capabilities and Margins*

radius of perigee is about 1.1 R_E. The delta-v required to deorbit these satellites to a 100 km altitude is 57.19 m/s.

To maximize the radio tomographic imaging area, the distance between the apogees of the orbits was to be kept near or above 2 R_E. The radius of apogee chosen for the inner orbit is 4.25 R_E. This results in a difference of 2 R_E between the inner and outer orbit apogees. The corresponding perigee radius is 1.52 R_E. This orbit ensures that each satellite in the inner orbit spends above 60% of the time above 3 R_E. The delta-v required to deorbit the inner satellites to the atmosphere is significantly higher than that required for the outer orbit. Thus, the inner orbit satellites are instead disposed of in a graveyard orbit between LEO and GEO. The delta-v required to achieve this is significantly lower, 40.14 m/s.

G.4 Flight System

G.4.1 RadioSat

A notional PILOT RadioSat spacecraft design is shown in Figure G.1. Details of RadioSat flight system capabilities is shown in G.5. The bus baselined for this study is from Muon Space. Muon Space's modular bus and avionics architecture allows for high-reuse to ensure stable and well tested designs, while maintaining flexibility in allowing for customization of components like the solar arrays, mechanical structures, instrument interfaces, harnessing and payloads, while still limiting the bus to contain only systems necessary for the mission, and therefore minimizing the components that must tolerate the radiation environment.

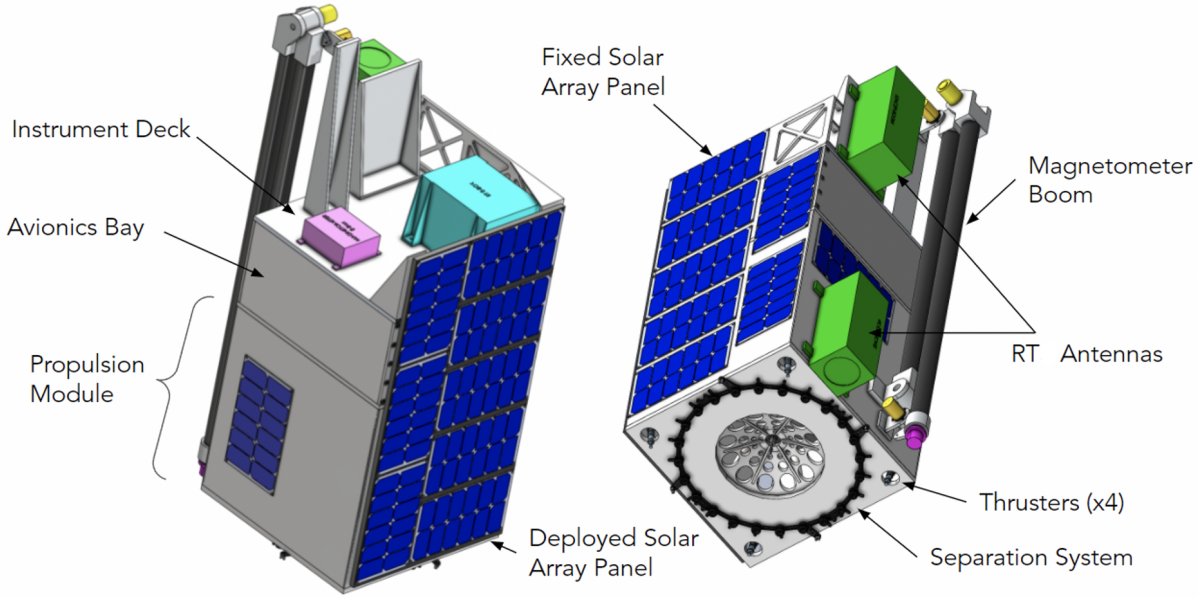

Figure G.1: *The PILOT RadioSat spacecraft design leverages Muon Space's modular bus design to meet mission requirements.*

G.4.1.1 Attitude Control

The attitude determination and control subsystem consists of one electronics board to process sensor data and control actuators, three reaction wheels, six sun sensor and magnetometer assemblies, and an inertial measurement unit. A star tracker is not included, because the attitude knowledge requirement (Table G.2) is met by combining data from the six sun sensors with comparisons between FGM measurements near perigee with geomagnetic field models. This approach was used on prior missions [107, 108] to achieve attitude knowledge that meets PILOT requirements.

G.4.1.2 Command & Data Handling and Telecom

Data is first generated by the instruments. It then flows through an instrument interface board where data is converted from serial data interfaces to ethernet before it flows through

a switch on the Electrical Power System (EPS), then to nonvolatile memory on the flight computer. The flight computer board has a built-in software defined radio to receive commands from the ground over S-band and to send telemetry and instrument data to the ground over X-band. The front-end for the radio is a separate board, and interfaces to either a patch array for mission data or a pair of hemispherical patch antennas for when in safe-mode. Two hemispherical patch antennas are used to receive commands. The link budget closes with more than 3dB of margin for a 200 Mbps mission data rate.

G.4.1.3 Power

The EPS serves as both power distribution and a communication switch/distribution for both ethernet and controller area network (CAN) buses. The EPS is based around a radiation-hard processor so that it ensures system survival in the case of functional upsets in other components. The EPS interfaces to the solar array strings, the 3 or more lithium-based battery packs, and distributes, switches, and monitors power to the rest of the system.

The solar array is a custom design using multi-junction solar cells and is designed to specification for this mission. One deployable panel is needed and deploys opposite the magnetometer boom to help balance torques due to atmospheric drag near perigee (Figure 4.3).

G.4.1.4 Propulsion

The PILOT RadioSats baseline an Aerojet Rocketdyne miniature blow-down hydrazine monopropellant system as a low-risk, low-cost propulsion solution. Each of the 30 RadioSat spacecraft use an identical propulsion module, which incorporates an ExoLaunch CarboNIX separation ring on the outermost face to accommodate mounting of the spacecraft onto the LV ESPA-Grande ring via an ExoPort adapter (Figure 4.2).

Manufactured as an aluminum isogrid, PILOT's propulsion module supports four 1-N thrusters distributed at its corners, with a centerline-mounted diaphragm propellant tank and the remainder of the propulsion components and tubing affixed to its interior surface.

Thrusters are canted inward in opposed pairs to provide roll, pitch, and yaw control. Series redundant latch valves in addition to the single-seat thruster valves provide two-fault leak tolerance for ground operations. Pressure measurement of the tank ullage facilitates approximate monitoring of approximate propellant consumption.

G.4.1.5 Structures & Mechanisms

Bus mechanical components are composed of machined aluminum plates and aluminum brackets held together by fasteners. The primary structure around the bus components is thicker than needed for structural reasons to provide the additional radiation shielding for bus electronic components.

The solar array release and deployment mechanism is composed of off-the-shelf components. Release is handled by two TiNi E250 ejector release mechanisms, and hinges and spring mechanisms are provided by the solar array vendor. The launch vehicle separation mechanism is a 15" diameter CarboNIX provided by ExoLaunch.

The integrated flight system is designed to fit in the volume available for an EXOport 24" to four 15" port adapter as shown in 4.2.

G.4.1.6 Thermal

RadioSats use MLI, temperature sensors, and active heaters together to provide provide thermal stability for subsystems and instruments. Temperature regulation is provided using patch heaters with setpoints controlled through flight software.

G.4.1.7 Instrument Accommodation

The RadioSat spacecraft top panel serves as instrument deck, hosting the RT, EED, and FGM electronics boxes. The bus provides power to the payload using a power and data interface module.

G.4.1.8 Radiation Tolerance and Reliability

For RadioSat spacecraft, PILOT adopts the careful COTS [266] approach that has been successfully implemented by companies such as Skybox and Sinclair Interplanetary. This process involves an understanding of the radiation environment that the parts are to be used in, including the temperature ranges, pressure, loads, and radiation. The PILOT radiation environment was analyzed using the SPENVIS tool and is shown in Table G.4 for a 30-day period. The total mission life is three years, and the dose accumulated in Silicon is shown as a function of aluminum shielding thickness for both the inner and outer orbits.

Total dose accumulation is higher for the inner orbit, while solar protons are higher for the outer orbit. All active electronic parts used by the bus have been tested for Total Ionizing Dose (TID) and Displacement Damage (DD) in a high-energy proton beam facility to a minimum dose of 40 krad(Si) up to 100 krad(Si). Testing includes executing code on applicable devices to ensure the entire device is exercised to find any non-destructive Single Event Effects (SEE), and flight code is used when available. Any destructive SEE observed disqualifies the part from use in flight, and non-destructive SEE are evaluated on a case-by-case basis and may be accepted if the rate is very low or the part is not mission critical.

Achieving a total dose of less than 40 krad(Si) over the three-year mission life requires shielding thickness of at least 10 mm when assuming an aluminum sphere. RadioSat electronics are relatively small, and each board is packaged in its own enclosure that provides 2 mm of shielding on the top and bottom (parallel to the board plane) and 3.5 mm around the perimeter. When the enclosures are stacked, the shielding in the stacked direction is 4 mm between boards. In all directions the spacecraft structure provides an additional 3 mm of shielding. The propulsion module and other components provide additional shielding around the electronics, with a conservative estimate in the minimum direction of an additional 4 mm. This results in a conservative estimate of shielding around electronics housed within the spacecraft structure. An additional 4 mm of shielding is added to the primary electronics housing.

The integrated sun sensor and magnetometer cannot be packaged within the bus structure. The sun sensors are only protected by 3 mm of aluminum, so additional shielding and testing are required.

Al absorber thickness			Total	Trapped electrons	Brems-strahlung	Trapped protons	Solar protons	Tr. electrons+ Bremsstrahlung	Tr. el.+Bremss. +Tr. protons
(mm)	(mils)	(g cm^{-2})							
0.050	1.968	0.014	2.508E+07	1.475E+07	2.847E+04	1.030E+07	1.327E-01	1.477E+07	2.508E+07
0.100	3.937	0.027	1.132E+07	8.630E+06	1.809E+04	2.673E+06	1.327E-01	8.648E+06	1.132E+07
0.200	7.874	0.054	5.003E+06	4.202E+06	1.015E+04	7.909E+05	1.327E-01	4.212E+06	5.003E+06
0.300	11.811	0.081	2.833E+06	2.396E+06	6.611E+03	4.304E+05	1.327E-01	2.403E+06	2.833E+06
0.400	15.748	0.108	1.808E+06	1.521E+06	4.706E+03	2.827E+05	1.327E-01	1.526E+06	1.808E+06
0.500	19.685	0.135	1.249E+06	1.041E+06	3.597E+03	2.041E+05	1.327E-01	1.045E+06	1.249E+06
0.600	23.622	0.162	9.154E+05	7.594E+05	2.901E+03	1.531E+05	1.327E-01	7.623E+05	9.154E+05
0.800	31.496	0.216	5.664E+05	4.733E+05	2.094E+03	9.096E+04	1.328E-01	4.754E+05	5.664E+05
1.000	39.370	0.270	3.959E+05	3.361E+05	1.652E+03	5.812E+04	1.328E-01	3.377E+05	3.959E+05
1.500	59.055	0.405	2.087E+05	1.834E+05	1.090E+03	2.417E+04	1.329E-01	1.845E+05	2.087E+05
2.000	78.740	0.540	1.271E+05	1.135E+05	8.073E+02	1.282E+04	1.330E-01	1.143E+05	1.271E+05
2.500	98.425	0.675	8.100E+04	7.217E+04	6.350E+02	8.192E+03	1.333E-01	7.280E+04	8.099E+04
3.000	118.110	0.810	5.221E+04	4.592E+04	5.228E+02	5.763E+03	1.334E-01	4.644E+04	5.221E+04
4.000	157.480	1.080	2.266E+04	1.897E+04	3.872E+02	3.306E+03	1.338E-01	1.935E+04	2.266E+04
5.000	196.850	1.350	1.017E+04	7.668E+03	3.084E+02	2.190E+03	1.341E-01	7.977E+03	1.017E+04
6.000	236.220	1.620	4.843E+03	2.927E+03	2.581E+02	1.657E+03	1.345E-01	3.185E+03	4.843E+03
7.000	275.590	1.890	2.639E+03	1.066E+03	2.235E+02	1.350E+03	1.349E-01	1.290E+03	2.639E+03
8.000	314.960	2.160	1.718E+03	3.650E+02	1.982E+02	1.155E+03	1.353E-01	5.632E+02	1.718E+03
9.000	354.330	2.430	1.316E+03	1.176E+02	1.796E+02	1.019E+03	1.356E-01	2.972E+02	1.316E+03
10.000	393.700	2.700	1.095E+03	3.603E+01	1.652E+02	8.936E+02	1.359E-01	2.013E+02	1.095E+03
12.000	472.440	3.240	8.612E+02	2.699E+00	1.442E+02	7.141E+02	1.366E-01	1.469E+02	8.610E+02
14.000	551.180	3.780	7.262E+02	8.187E-02	1.296E+02	5.964E+02	1.374E-01	1.297E+02	7.261E+02
16.000	629.920	4.320	6.455E+02	6.265E-04	1.185E+02	5.268E+02	1.382E-01	1.185E+02	6.453E+02
18.000	708.660	4.860	5.914E+02	7.380E-06	1.093E+02	4.820E+02	1.391E-01	1.093E+02	5.913E+02
20.000	787.400	5.400	5.432E+02	0.000E+00	1.015E+02	4.416E+02	1.399E-01	1.015E+02	5.431E+02

Al absorber thickness			Total	Trapped electrons	Brems-strahlung	Trapped protons	Solar protons	Tr. electrons+ Bremsstrahlung	Tr. el.+Bremss. +Tr. protons
(mm)	(mils)	(g cm^{-2})							
0.050	1.968	0.014	1.451E+07	9.803E+06	1.900E+04	4.676E+06	8.787E+03	9.822E+06	1.450E+07
0.100	3.937	0.027	7.063E+06	5.865E+06	1.238E+04	1.180E+06	5.145E+03	5.877E+06	7.058E+06
0.200	7.874	0.054	3.336E+06	2.996E+06	7.242E+03	3.300E+05	2.893E+03	3.003E+06	3.333E+06
0.300	11.811	0.081	1.979E+06	1.800E+06	4.879E+03	1.724E+05	2.008E+03	1.805E+06	1.977E+06
0.400	15.748	0.108	1.314E+06	1.198E+06	3.554E+03	1.108E+05	1.515E+03	1.201E+06	1.312E+06
0.500	19.685	0.135	9.318E+05	8.488E+05	2.755E+03	7.906E+04	1.216E+03	8.515E+05	9.306E+05
0.600	23.622	0.162	6.931E+05	6.311E+05	2.235E+03	5.867E+04	1.022E+03	6.334E+05	6.920E+05
0.800	31.496	0.216	4.283E+05	3.917E+05	1.606E+03	3.422E+04	7.580E+02	3.933E+05	4.275E+05
1.000	39.370	0.270	2.923E+05	2.689E+05	1.247E+03	2.158E+04	5.964E+02	2.702E+05	2.917E+05
1.500	59.055	0.405	1.420E+05	1.319E+05	7.874E+02	8.900E+03	3.864E+02	1.327E+05	1.416E+05
2.000	78.740	0.540	7.934E+04	7.374E+04	5.647E+02	4.753E+03	2.773E+02	7.431E+04	7.906E+04
2.500	98.425	0.675	4.698E+04	4.326E+04	4.358E+02	3.069E+03	2.144E+02	4.369E+04	4.676E+04
3.000	118.110	0.810	2.879E+04	2.608E+04	3.554E+02	2.187E+03	1.726E+02	2.643E+04	2.862E+04
4.000	157.480	1.080	1.161E+04	9.934E+03	2.621E+02	1.292E+03	1.207E+02	1.020E+04	1.149E+04
5.000	196.850	1.350	4.997E+03	3.816E+03	2.095E+02	8.820E+02	9.012E+01	4.025E+03	4.907E+03
6.000	236.220	1.620	2.362E+03	1.430E+03	1.767E+02	6.835E+02	7.213E+01	1.607E+03	2.290E+03
7.000	275.590	1.890	1.294E+03	5.138E+02	1.541E+02	5.674E+02	5.875E+01	6.679E+02	1.235E+03
8.000	314.960	2.160	8.523E+02	1.727E+02	1.375E+02	4.932E+02	4.902E+01	3.101E+02	8.033E+02
9.000	354.330	2.430	6.630E+02	5.421E+01	1.251E+02	4.416E+02	4.202E+01	1.794E+02	6.210E+02
10.000	393.700	2.700	5.615E+02	1.587E+01	1.156E+02	3.940E+02	3.604E+01	1.315E+02	5.255E+02
12.000	472.440	3.240	4.559E+02	1.112E+00	1.013E+02	3.254E+02	2.808E+01	1.024E+02	4.278E+02
14.000	551.180	3.780	3.926E+02	3.367E-02	9.116E+01	2.790E+02	2.235E+01	9.119E+01	3.702E+02
16.000	629.920	4.320	3.525E+02	2.576E-04	8.339E+01	2.507E+02	1.837E+01	8.339E+01	3.341E+02
18.000	708.660	4.860	3.243E+02	3.046E-06	7.680E+01	2.320E+02	1.552E+01	7.680E+01	3.088E+02
20.000	787.400	5.400	2.990E+02	0.000E+00	7.121E+01	2.147E+02	1.313E+01	7.121E+01	2.859E+02

Table G.4: *Radiation total dose in rad (Si) as a function of Al shielding thickness for inner (Top) and outer (Bottom) orbit over 30 days. From SPENVIS, SHIELDOSE-2, v2.10.*

Flight System Element Parameters (as appropriate)	Value/ Summary, units
General	
Design Life, months	36
Structure	
Structures material (aluminum, exotic, composite, etc.)	Aluminum
Number of articulated structures	None
Number of deployed structures	4 (RT stacers, mag boom, solar array)
Aeroshell diameter, m	N/A
Thermal Control	
Type of thermal control used	Passive thermal radiator
Propulsion	
Estimated delta-V budget, m/s	135
Propulsion type(s) and associated propellant(s)/oxidizer(s)	Hydrazine
Number of thrusters and tanks	4 thrusters/1tank
Specific impulse of each propulsion mode, seconds	206
Attitude Control	
Control method (3-axis, spinner, grav-gradient, etc.).	3-axis stabilized
Control reference (solar, inertial, Earth-nadir, Earth-limb, etc.)	Solar
Attitude control capability, degrees	1
Attitude knowledge limit, degrees	1
Agility requirements (maneuvers, scanning, etc.)	None
Articulation/#–axes (solar arrays, antennas, gimbals, etc.)	None
Sensor and actuator information (precision/errors, torque, momentum storage capabilities, etc.)	RWA, IMU, CSS
Command & Data Handling	
Flight Element housekeeping data rate, kbps	4.8
Data storage capacity, Mbits	2048000
Maximum storage record rate, kbps	1.00E+06
Maximum storage playback rate, kbps	2.00E+06
Power	
Type of array structure (rigid, flexible, body mounted, deployed, articulated)	Deployed, fixed
Array size, meters x meters	0.54 m^2
Solar cell type (Si, GaAs, Multi-junction GaAs, concentrators)	Multi-Junction GaAs
Expected power generation at Beginning of Life (BOL) and End of Life (EOL), W	187 W BOL, 157 W EOL
On-orbit average power consumption, W	102
Battery type (NiCd, NiH, Li-ion)	Li-ion
Battery storage capacity, amp-hours	7.2

Table G.5: *RadioSat spacecraft capabilities*

G.4.2 PlasmaSat and PlasmaSatEUV

The spacecraft bus is designed to satisfy all science requirements, utilizing identical baseline bus subsystems and configurations for both PlasmaSat and PlasmaSatEUV, with the addition of accommodation for the EUV cameras on PlasmaSatEUV. The baseline PlasmaSat and PlasmaSatEUV configurations use heritage components, and requirements fall within Ball Aerospace's current capabilities. Therefore, a Ball Aerospace bus is taken as the baseline for this mission concept study. Deployments are required for instrument booms (FGM, SCM, EFI) and a high gain toroidal antenna. Details of flight system elements are shown in Table G.5.

G.4.2.1 Attitude Control

The spin stabilized attitude control system is designed to maximize science coverage. Four 1N thrusters are sized to provide enough thrust to spin up, spin down, and maintain spin rates for the entire duration of the mission. Due to the length of the EFI wire booms, the vehicle needs to be spin stabilized even during safe modes to maintain boom deployment.

Two operational stellar reference units (SRU) and digital sun sensors (DSS) are required to meet pointing knowledge requirements during operation and safe modes.

Coupled with fine balancing of the spacecraft using ballast mass, an onboard nutation dampener helps minimize imbalance during the vehicle's rotation.

G.4.2.2 Command & Data Handling

PILOT uses a single-string avionics chassis containing both C&DH and power distribution boards. The avionics consists of a single board computer (SBC); instrument interface board with error detection and correction (EDAC) memory storage; analog and digital interface board for bus equipment; multiple power switching boards for power distribution and solar array switching. The unit is single event latchup (SEL) immune and designed for single event upset (SEU) mitigation in the PILOT radiation environment.

G.4.2.3 Power

The power subsystem is power positive in all modes at its worst-case $\sim 25.5^o$ solar off-point and requires no solar panel deployments. Only the launch scenario and eclipses require battery operation.

The solar panels provide a total area of 5.6 m^2 providing a maximum orbit average of 290 W. The outer orbit has been used as the bounding case due to the additional EUV camera and maximum eclipse of 125 minutes. Two 22.5 Ahr batteries provide maximum 38% DOD for maximum eclipse duration.

G.4.2.4 Propulsion

The propulsion system is a heritage monopropellant blowdown hydrazine system sized to 200 m/s mission delta-V. This breaks down to 150 m/s for mission needs (orbit maintenance, initial orbit phasing, and attitude control) and 50m/s of mission margin.

Four 1N thrusters are positioned for controlled spin up maneuvers. One 19" propellant tank has ample storage for the propellant for all maneuvers including disposal for both

the PlasmaSat (26 kg propellant) and the PlasmaSatEUV (32 kg propellant), with 50m/s margin for each.

G.4.2.5 Structures & Mechanisms

The structural design is based on Ball's BCP rideshare platform to accommodate PILOT's use of ESPA-Grande Ring Adapters for launch, and is similar to that used on GPIM and STPSat 2/3. Additional mass has been allocated for increased shielding due to the radiation environment. PILOT's bus structure supports the body-fixed solar panels, maximizing power for a spinning spacecraft and taking into account the constraint imposed by the height of ESPA-Grande Ring LV Adapter. The deployed to fixed antenna boom allows for the toroidal antenna to provide a clear FOV without blockage from the spacecraft.

G.4.2.6 Telecom

PILOT transmits directly to Earth during all portions of its mission without interrupting science operations using an X-band omni directional antenna that provides coverage during spacecraft spin. Data rate capability ranges from 250kbps at max range (38,000 km) to max transmitter rate of 1 Mbps at min range (5,000 km) with ranging. A link budget was performed to a 5.4-m AWS ground antenna and a S/C antenna with 9 dBi gain. Two omni patch receive antennas provide commanding at 62bps (38,000 km) to 2kbps (5,000 km).

G.4.2.7 Thermal

The thermal design uses flight-proven, heritage control systems. Radiators, MLI, temperature sensor, and active heaters work together to provide three dedicated temperature zones to accommodate subsystems and instruments. The -Z deck of the spacecraft provides radiating area for bus equipment and a separate temperature zone for the battery. The +Z deck provides a controlled thermal interface for instrument electronics and instruments. Temperature regulation is provided using Kapton heaters with setpoints are controlled through flight software.

G.4.2.8 Instrument Accommodation

The spacecraft bus accommodates two configurations of the instrument suite: PlasmaSat, with SCM & FGM Booms, EFI Booms, PIMS, and EPS sensors, and PlasmatSatEUV: with all PlasmaSat instruments plus 3 EUV cameras. The spacecraft top panel serves as instrument deck, all instrument electronics boxes are mounted inside the spacecraft for radiation shielding. The payload deck is thermally controlled. The bus provides power to the instruments via multiple switched power feeds and resettable overcurrent protection. Each instrument provides RS-422 for command and telemetry and four interfaces (EMF Suite, EPS, PIMS, EUVCS) interface with the spacecraft.

G.5 Concept of Operations

RadioSat spacecraft have two operational modes: Launch & Early Operations and Science. During Launch & Early Operations, all RadioSat spacecraft are checked out.

After spacecraft checkout is complete, all instruments are powered on, the FGM booms are deployed, followed by the RT stacers, and instrument commissioning begins. After the RadioSats achieve their final orbital configuration, science operations begin. The FGM, RT, and EED maintain a 100% duty cycle for the duration of the mission lifetime.

PlasmaSat and PlasmaSatEUVs have three operational modes: Launch & Early Operations, Safe Mode, and Science. During Launch & Early Operations, PlasmaSats and PlasmaSatEUVs fire thrusters to spin the spacecraft. Spacecraft are checked out. After spacecraft checkout, SCM and FGM booms are deployed, then EFI wire boom antennas are deployed over many orbits in a pair-wise fashion. PIMS and EUVCS are powered on and instrument commissioning begins. After the RadioSats achieve their final orbital configuration, science operations begin. All instruments maintain a 100% duty cycle for the duration of the mission lifetime.

After initial deployment and checkout of the RadioSats, the 30 satellites require small correction maneuvers approximately once per month to maintain optimum spacing. These maneuvers are uploaded and autonomously performed by the spacecraft at apoapsis. The routine uplink of commands, the downlink of telemetry and science data is automated using existing MOC software tools. This minimizes the need for operation personnel to support real-time contacts, thus reducing overall operational costs. Daily ground stations contacts are scheduled via Amazon Web Services (AWS) Ground Stations. The contacts are scheduled daily at the spacecraft periapsis. If a contact fails or if the spacecraft indicates an anomalous condition, the operations team is informed via an automated message system.

The two PlasmaSats and two PlasmaSatEUVs have a similar operations concept to the RadioSats. In addition to the standard commanding and telemetry downlink, the MOC is also responsible for uplinking any modification to the instrument operations to accommodate for anomalies or changes in science planning. Contacts with the PlamaSats use the same AWS Ground Stations as the RadioSats.

All spacecraft/instrument telemetry and science data are directly deposited in AWS Cloud for retrieval and subsequent processing by the Mission Operations Center (MOC) or Science Data Center (SDC). The amount of data residing and the time the data remains in the Cloud is minimized. All the Level 0 and processed data are archived with an off-site back up by the MOC and SDC. The notional PILOT ground system design is shown in Figure G.2. PlasmaSat/PlasmaSat spacecraft use X-band for downlink and uplink, and RadioSat spacecraft use X-band for downlink and S-band for uplink. The nominal PILOT link budget is shown in Table G.6.

Mission and Science Operations efforts for PILOT are centrally located at a single institution with the experience and necessary information technology and personnel support in place to support operation of the flight mission. The MOC is responsible for monitoring of the PILOT RadioSats and PlasmaSats health, telemetry and issuing commands to the spacecraft and instruments. The MOC is responsible for coordination and contact with AWS ground stations (Singapore, Bahrain and Hawaii) to communicate with the PILOT spacecraft through an Application Programming Interface (API). The MOC coordinates with the SOC on the necessary commands, configuration and operations of the scientific instruments on the spacecraft to to ensure successful science. The Science Operation Center (SOC) works closely with the MOC and science instrument teams during instrument con-

Down link Information (per spacecraft)	Launch & Early Ops				Science Operations			
	RadioSat Inner	RadioSat Outer	PlasmaSat	PlasmaSat EUV	RadioSat Inner	RadioSat Outer	PlasmaSat	PlasmaSat EUV
Number of Contacts per Week	28	21	18	18	28	21	18	18
Number of Weeks for Mission Phase, weeks	4	4	4	4	4	4	4	4
Downlink Frequency Band, GHz	X-band, 8.4		X-band, 8.4		X-band, 8.4		X-band, 8.4	
Telemetry Data Rate(s), kbps	500	500	500	500	500	500	500	500
Transmitting Antenna Type(s) and Gain(s), dBi	X-band omni, 15	X-band omni, 15	X-band, 9	X-band, 9	X-band omni, 15	X-band omni, 15	X-band, 9	X-band, 9
Transmitter peak power, Watts	5	5	20	20	5	5	20	20
Downlink Receiving Antenna Gain, dBi	55.1	55.1	55.1	55.1	55.1	55.1	55.1	55.1
Transmitting Power Amplifier Output, Watts	--	--	--	--	--	--	--	--
Total Daily Data Volume, (MB/day)	1051	1051	5756	33750	1051	1051	5756	11713.95
Uplink Information								
Number of Uplinks per Day	1	1	1	1	1	1	1	1
Uplink Frequency Band, GHz	2.2, S-band	2.2, S-band	2.2, S-band	2.2, S-band	2.2, S-band	2.2, S-band	2.2, S-band	2.2, S-band
Telecommand Data Rate, kbps	32	32	32	32	32	32	32	32
Receiving Antenna Type(s) and Gain(s), dBi	55.1	55.1	55.1	55.1	55.1	55.1	55.1	55.1

Table G.6: *PILOT link budget*

ditioning and checkout to ensure the instruments are configured to return optimal science. After commissioning the SOC is responsible for verifying the Level 0 data from the PILOT spacecraft as well as processing the data and providing the Level 1 data to the Science Data Center. The MOC and SOC is staffed 24/7 through one month after commissioning of the spacecraft and the start of science operations. Staffing is reduced at this point with automated monitoring enabling unattended operations. Daily summaries are generated by the MOC and SOC on the spacecraft and payload health and status.

A central Science Data Center SDC is established for the PILOT mission. The SDC may or may not be located at the same institution as the MOC and SOC but is required to coordinate and work closely with them to ensure successful scientific operation. The SDC is responsible for processing instrument data to provide Level 2, 3 and ancillary

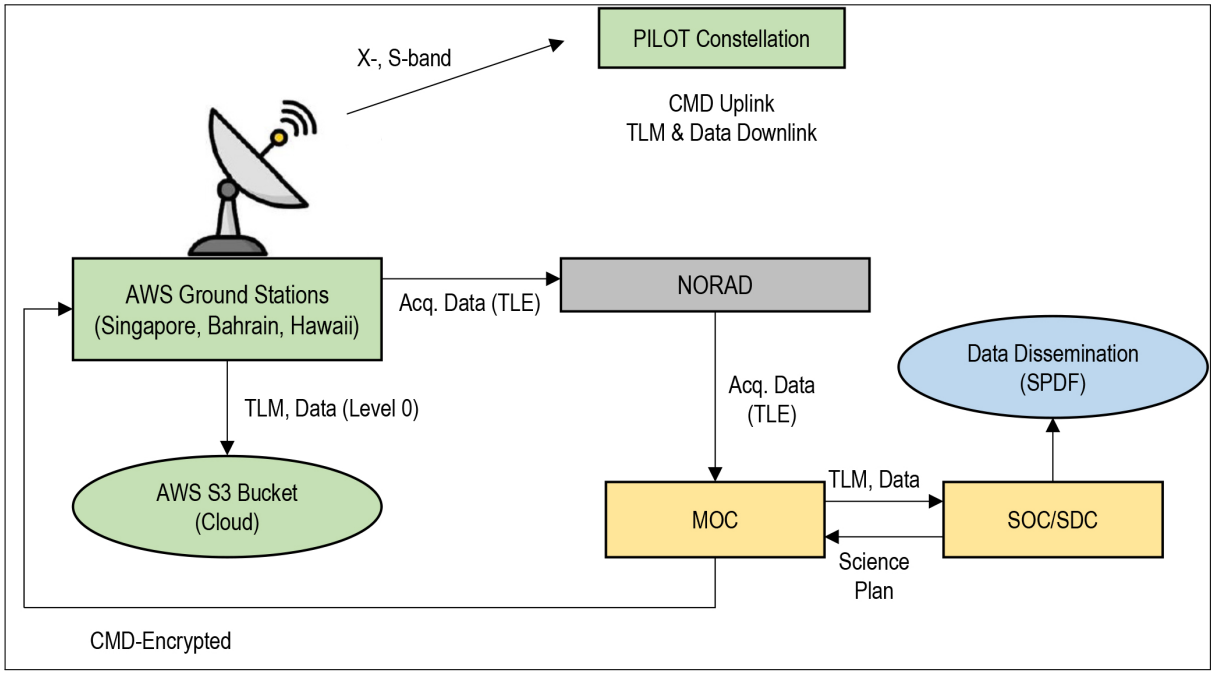

Figure G.2: *PILOT notional ground system*

datasets in close coordination with the science instrument teams. The SDC is responsible for ensuring appropriate public release of data, providing public tools for analyzing the data and ensuring the execution of the PILOT data management plan.

G.6 Technology Maturation Plan

G.6.1 RT RF

To mature the RF instrument technology to TRL 6, a laboratory prototype must be designed and built, then tested in relevant environmental conditions.

The first development milestone is to develop a laboratory prototype for the RF transmitter power bank (described in §C.1.1). One can begin with the capacitor power bank from the MAGCAT proposed design [104]. This development should investigate the use of modern aerogel-based capacitor technologies or Li batteries for the power bank. An prototype RF transmitter board that makes use of the power bank input must be built in parallel. Radio frequency transmitter technology is highly mature and the transmitter board requires no exploratory development.

Both boards must be connected to each other and representative stacer antennas. The full prototype system is life-cycle tested and has its antenna broadcast power efficiency characterized at a RF test facility. This milestone is reached when there is a functional transmitter powered by the power bank delivering an appropriate-power radio pulse at 50 MHz and 150 MHz which can be repeated every 10 s for a large number of cycles ($\geq 500,000$) without significant degradation of or damage to system components.

The second milestone is to develop an isolation system, either using a switch or isolator, to ensure that transmitter pulses do not damage sensitive receiver electronics. Existing commercial designs are likely to work, but may require modification to handle the power,

pulse rate, and number of cycles required for PILOT. This milestone is reached when it can be demonstrated that signals from the transmitter can be sufficiently isolated from a receiver to prevent damage.

The third milestone is to develop a RF receiver that is optimized to receive the transmission pulse from the RF transmitter. The receiver must have sensitivity to the pulse phase to achieve PILOT science objectives and also must be designed to automatically tune based on previous received pulse peaks, entering into a search mode if a pulse is not received as expected. This is necessary due to slight variations in pulse peak expected due to Doppler shift and transmitter signal drift. This primarily requires development of receiver frequency sweep and lock protocols. Radio frequency receiver technology is highly mature and receiver board development should require no exploratory development. This milestone is achieved when bench-top tests demonstrate that PILOT-appropriate variations in phase and frequency can be detected.

	Year 1				Year 2				Year 3			
	Q1	Q2	Q3	Q4	Q1	Q2	Q3	Q4	Q1	Q2	Q3	Q4
Capacitive Power Board, Design, Fabricate, Test												
Transmitter Board, Design, Fabricate, Test												
Power Board and Transmitter Board I&T												
Milestone 1 Achieved												
RF Isolation System Design and Fabricate, Test												
RF Isolation System+Transmitter/Power Board I&T												
RF Receiver Design, Fabrication, Test												
RF Calibration System Design, Fabrication Test												
RF Prototype I&T												
RT Prototype Design												
RT Prototype #1 and #2 Fabrication												
RT Prototype Laboratory Functional Testing												
RT Prototype Vacuum and Long Term Stability Test												

Table G.7: *RT RF technology maturation plan schedule*

The fourth and final milestone is to use the hardware developed in milestones one through three, and fabricate two RT prototype systems consisting of a stacer antennas, transmitter, receiver, and power bank. These prototypes are used to provide a TRL 6 demonstration of the RT instrument. This demonstration is accomplished by placing each set of transmitter and receiver electronics in a thermal vacuum chamber to simulate the space environment, connecting these to an antenna system external to the chamber, and sending pulses between each unit for a long term test (3 month) test. This demonstrates the stability of the transmitter and receiver, the isolation between the two, the reliability of the power bank, and enable characterization of the thermal and electrical behavior of the instrument systems.

Estimated cost for this RT RF technology development activity is given in Table 5.2. Schedule for this RT RF technology development activity is given in Table G.7.

G.6.2 EUVCS

The EUVCS optical/mechanical design is nearly identical to that of IMAGE EUV [125, 127]. A robust and detailed Technology Maturation Plan (TMP) was developed (for the 2019 TREO MIDEX proposal) by SwRI in partnership with Lawrence Livermore National Laboratory (LLNL). The TMP -which is notional, and included here to demonstrate the feasibility and resources necessary for PILOT's use of this technology — builds and tests a TRL 6 prototype in 11 months (Table G.8), for $4M including $1M each for

mirrors/coatings and prototype detector. A single prototype sensor head tests EUV-He or EUV-O performance by swapping full aperture filters and full-scale multilayer (ML) coated spherical mirrors. EUVCS ML coatings are applied using lateral grading [267] to compensate for varying incidence angle vs surface location—the entire mirror is optimized to the same peak wavelength. ML mirror coatings are performed at LLNL. The technology used at LLNL for lateral grading of ML coatings is proven, has excellent stability and repeatability, and has been used for ∼20 years to coat large-area curved optics for a variety of applications including the EUV ML mirrors for the SDO and GOES missions [267, 268, 269, 270, 271, 272, 273]. Al/ Mg/SiC ML coatings, pioneered at LLNL, are highly reflective and corrosion resistant. The two specific Al/Mg/SiC ML coating designs for EUV-A/B have already been demonstrated on flat SiO2 substrates (and aged for 6+ months) [125].

The flight coating fixture hardware is designed and fabricated at LLNL. ML coating on EUVCS's large-radius, steeply curved mirror substrates consists of: (1) optimization of lateral ML thickness profile on flight-identical test mirror substrates, including measurements at flight wavelengths and incidence angles; (2) pre-coating validation of flight mirror surface quality and smoothness via precision surface metrology at LLNL; (3) coating of 1 prototype + 3 flight mirrors for each of the EUV-He and EUV-O validated ML coating formulas. The TMP includes ample resources for curved-mirror ML coating development. The full size annular filters and coated spherical mirrors are tested at [30.4, 58.4, 83.4, 121.6] nm and integrated into the prototype with a full-scale spherically curved MCP detector. End-to-end optical performance tests baseline the required FOV, angular resolution, sensitivity and background rejection. Environmental tests (vibration, acoustic, thermal vacuum) are performed, followed by a second end-to-end test to confirm optical performance, demonstrating TRL 6.

	Month #										
	1	2	3	4	5	6	7	8	9	#	#
Detector Fabrication											
Mirror Substrates											
Filter Fabrication											
Sensor Head Mechanical											
Filter Calibration											
Mirror Calibration											
Integration & Alignment											
Detector Integration											
End-to-End Optical Testing											
Vibration Testing											
Thermal Vacuum Testing											
End-to-End Calibration											
Schedule Reserve											

Table G.8: *EUVCS technology maturation plan schedule*

G.6.3 SPB

PIMS's modular design allows implementation of the Sensor Panel Bias (SPB) system with only very minor changes from the heritage Van Allen Probes HOPE design (Appendix C.6). The PIMS sensor and electronics unit are TRL 7. All parts in the BB and SPB panel are TRL 6 or higher. Though the SPB is structurally and functionally simple (and therefore it does not represent a full-fledged technology gap), its design must still be tested side-by-side with the PIMS instrument. Accordingly, for the 2019 TREO MIDEX proposal a robust, detailed, funded ($250K) Implementation Plan was developed to build an engineering model (EM) of the SPB panel (reduced-area but functionally identical to the flight unit) that is tested with the rest of PIMS.

Task	Duration	Description
Pre-Build Review	1 month	Pre-build review of SPB: a simple machined Al plate (connected to BB, total power & current: <1mW / <1mA; §E.1.2.3), insulated standoffs, & removable panel cover
Fabrication	1 month	Fabricate SPB panel & apply surface finish identical to sensor
Integration	1 month	Integration of simple parts
Test	1 month	Initial testing verifies SPB functionality and electrical isolation from SC bus
Integrate SPB to DTV, test	4 month	Integrate SPB to the Dynamic Test Vehicle (DTV) to validate structural design in launch environment (shock, vibe & acoustic)

Table G.9: *SPB technology maturation plan schedule*

H References

References

[1] Robin Ramstad and Stas Barabash. Do Intrinsic Magnetic Fields Protect Planetary Atmospheres from Stellar Winds? *Space Sci. Rev.*, 217(2):36, March 2021. doi:10.1007/s11214-021-00791-1.

[2] Bruce M. Jakosky. MAVEN Explores the Martian Upper Atmosphere. *Science*, 350(6261):643–643, November 2015. doi:10.1126/science.aad3443.

[3] D. V. Titov, H. Svedhem, D. McCoy, J. P. Lebreton, S. Barabash, J. L. Bertaux, P. Drossart, V. Formisano, B. Haeusler, O. I. Korablev, W. Markiewicz, D. Neveance, M. Petzold, G. Piccioni, T. L. Zhang, F. W. Taylor, E. Lellouch, D. Koschny, O. Witasse, M. Warhaut, A. Acomazzo, J. Rodrigues-Cannabal, J. Fabrega, T. Schirmann, A. Clochet, and M. Coradini. Venus Express: Scientific goals, instrumentation, and scenario of the mission. *Cosmic Research*, 44(4):334–348, July 2006. doi:10.1134/S0010952506040071.

[4] Gian Luca Delzanno, Joseph E. Borovsky, Michael G. Henderson, Pedro Alberto Resendiz Lira, Vadim Roytershteyn, and Dan Welling. The impact of cold electrons and cold ions in magnetospheric physics. *Journal of Atmospheric and Solar-Terrestrial Physics*, page 105599, 2021. URL: https://www.sciencedirect.com/science/article/pii/S1364682621000596, doi:https://doi.org/10.1016/j.jastp.2021.105599.

[5] L. Y. Khoo, X. Li, H. Zhao, S. A. Thaller, and B. Hogan. Multi-Event Studies of Sudden Energetic Electron Enhancements in the Inner Magnetosphere and Its Association With Plasmapause Positions. *Journal of Geophysical Research (Space Physics)*, 126(11):e29769, November 2021. doi:10.1029/2021JA029769.

[6] B. M. Walsh, T. D. Phan, D. G. Sibeck, and V. M. Souza. The plasmaspheric plume and magnetopause reconnection. *Geophys. Res. Lett.*, 41(2):223–228, January 2014. doi:10.1002/2013GL058802.

[7] Kanako Seki, Masafumi Hirahara, Masahiro Hoshino, Toshio Terasawa, Richard C. Elphic, Yoshifumi Saito, Toshifumi Mukai, Hajime Hayakawa, Hirotsugu Kojima, and Hiroshi Matsumoto. Cold ions in the hot plasma sheet of Earth's magnetotail. *Nature*, 422(6932):589–592, April 2003. doi:10.1038/nature01502.

[8] M. André and C. M. Cully. Low-energy ions: A previously hidden solar system particle population. *Geophysical Research Letters*, 39(3):L03101, February 2012. doi:10.1029/2011GL050242.

[9] E. Engwall, A. I. Eriksson, C. M. Cully, M. André, R. Torbert, and H. Vaith. Earth's ionospheric outflow dominated by hidden cold plasma. *Nature Geoscience*, 2(1):24–27, January 2009. doi:10.1038/ngeo387.

[10] E. G. Shelley, R. G. Johnson, and R. D. Sharp. Satellite observations of energetic heavy ions during a geomagnetic storm. *Journal of Geophysical Research*, 77(31):6104, January 1972. doi:10.1029/JA077i031p06104.

[11] M. M. Huddleston, C. R. Chappell, D. C. Delcourt, T. E. Moore, B. L. Giles, and M. O. Chandler. An examination of the process and magnitude of ionospheric plasma supply to the magnetosphere. *Journal of Geophysical Research (Space Physics)*, 110(A12):A12202, December 2005. doi:10.1029/2004JA010401.

[12] W. S. Kurth, S. De Pascuale, J. B. Faden, C. A. Kletzing, G. B. Hospodarsky, S. Thaller, and J. R. Wygant. Electron densities inferred from plasma wave spectra obtained by the Waves instrument on Van Allen Probes. *Journal of Geophysical Research (Space Physics)*, 120:904–914, February 2015. doi:10.1002/2014JA020857.

[13] Maria Andriopoulou, Rumi Nakamura, Simon Wellenzohn, Klaus Torkar, Wolfgang Baumjohann, R. B. Torbert, Per-Arne Lindqvist, Yuri V. Khotyaintsev, John Dorelli, and James L. Burch. Plasma density estimates from spacecraft potential using mms observations in the dayside magnetosphere. *Journal of Geophysical Research: Space Physics*, 123(4):2620–2629, 2018. URL: https://agupubs.onlinelibrary.wiley.com/doi/abs/10.1002/2017JA025086, arXiv:https://agupubs.onlinelibrary.wiley.com/doi/pdf/10.1002/2017JA025086, doi:https://doi.org/10.1002/2017JA025086.

[14] B. R. Sandel, R. A. King, W. T. Forrester, D. L. Gallagher, A. L. Broadfoot, and C. C. Curtis. Initial results from the IMAGE Extreme Ultraviolet Imager. *Geophysical Research Letters*, 28:1439–1442, April 2001. doi:10.1029/2001GL012885.

[15] David Malaspina, Robert Ergun, Jerry Goldstein, Constance Spittler, Laila Andersson, Joseph Borovsky, Xiangning Chu, Lauren De Moudt, Dennis Gallagher, Vania Jordanova, Solène Lejosne, Jason Link, Naomi Maruyama, Jeffery Parker, Scott Thaller, Bryce Unruh, and Brian Walsh. Plasma Imaging, LOcal Measurement, and Tomographic Experiment (PILOT): A Mission Concept for Transformational Multi-Scale Observations of Mass and Energy Flow Dynamics in Earth's Magnetosphere. *Frontiers in Astronomy and Space Sciences*, 9:910730, June 2022. doi:10.3389/fspas.2022.910730.

[16] D. A. Gurnett. Plasma wave interactions with energetic ions near the magnetic equator. *Journal of Geophysical Research*, 81(16):2765, June 1976. doi:10.1029/JA081i016p02765.

[17] R. C. Olsen, S. D. Shawhan, D. L. Gallagher, J. L. Green, C. P. Chappell, and R. R. Anderson. Plasma observations at the earth's magnetic equator. *Journal of Geophysical Research*, 92(A3):2385–2407, March 1987. doi:10.1029/JA092iA03p02385.

[18] Nagendra Singh. Effects of electrostatic ion cyclotron wave instability on plasma flow during early stage plasmaspheric refilling. *Journal of Geophysical Research*, 101(A8):17217–17228, August 1996. doi:10.1029/96JA01008.

[19] S. A. Boardsen, D. L. Gallagher, D. A. Gurnett, W. K. Peterson, and J. L. Green. Funnel-shaped, low-frequency equatorial waves. *Journal of Geophysical Research*, 97(A10):14967–14976, October 1992. doi:10.1029/92JA00827.

[20] Z. Hrbáčková, O. Santolík, F. Němec, E. Macúšová, and N. Cornilleau-Wehrlin. Systematic analysis of occurrence of equatorial noise emissions using 10 years of data from the Cluster mission. *Journal of Geophysical Research (Space Physics)*, 120(2):1007–1021, February 2015. doi:10.1002/2014JA020268.

[21] J. Goldstein, D. L. Gallagher, P. Molyneux, and G. D. Reeves. Core-Plasma Refilling and Erosion: Science Justification. In *Heliophysics 2050 White Papers*, pages MAGNETOSPHERE SCIENCE, #4063. NASA Heliophysics Division, 2021. URL: http://www.hou.usra.edu/meetings/helio2050/pdf/4063.pdf.

[22] C. G. Park. Whistler observations of the depletion of the plasmasphere during a magnetospheric substorm. *Journal of Geophysical Research*, 78(4):672, January 1973. doi:10.1029/JA078i004p00672.

[23] C. G. Park. Some features of plasma distribution in the plasmasphere deduced from Antarctic whistlers. *Journal of Geophysical Research*, 79(1):169–173, January 1974. doi:10.1029/JA079i001p00169.

[24] C. J. Farrugia, D. T. Young, J. Geiss, and H. Balsiger. The composition, temperature, and density structure of cold ions in the quiet terrestrial plasmasphere: GEOS 1 results. *Journal of Geophysical Research*, 94(A9):11865–11891, September 1989. doi:10.1029/JA094iA09p11865.

[25] D. L. Carpenter, B. L. Giles, C. R. Chappell, P. M. E. Décréau, R. R. Anderson, A. M. Persoon, A. J. Smith, Y. Corcuff, and P. Canu. Plasmasphere dynamics in the duskside bulge region: A new look at old topic. *Journal of Geophysical Research*, 98(A11):19,243–19,271, November 1993. doi:10.1029/93JA00922.

[26] B. W. Reinisch, X. Huang, P. Song, J. L. Green, S. F. Fung, V. M. Vasyliunas, D. L. Gallagher, and B. R. Sandel. Plasmaspheric mass loss and refilling as a result of a magnetic storm. *Journal of Geophysical Research (Space Physics)*, 109(A1):A01202, January 2004. doi:10.1029/2003JA009948.

[27] Z. C. Dent, I. R. Mann, J. Goldstein, F. W. Menk, and L. G. Ozeke. Plasmaspheric depletion, refilling, and plasmapause dynamics: A coordinated ground-based and IMAGE satellite study. *Journal of Geophysical Research (Space Physics)*, 111(A3):A03205, March 2006. doi:10.1029/2005JA011046.

[28] Bill R. Sandel and Michael H. Denton. Global view of refilling of the plasmasphere. *Geophysical Research Letters*, 34(17):L17102, September 2007. doi:10.1029/2007GL030669.

[29] D. L. Gallagher, R. H. Comfort, R. M. Katus, B. R. Sandel, S. F. Fung, and M. L. Adrian. The breathing plasmasphere: Erosion and refilling. *Journal of Geophysical Research: Space Physics*, 126(4):e2020JA028727, 2021. e2020JA028727 2020JA028727. URL: https://agupubs.onlinelibrary.wiley.com/doi/abs/10.1029/2020JA028727, arXiv:https://agupubs.onlinelibrary.wiley.com/doi/pdf/10.1029/2020JA028727, doi:https://doi.org/10.1029/2020JA028727.

[30] Bill R. Sandel. Composition of the plasmasphere and implications for refilling. *Geophysical Research Letters*, 38(14):L14104, July 2011. doi:10.1029/2011GL048022.

[31] J. L. Horwitz and M. Lockwood. The cleft ion fountain - A two-dimensional kinetic model. *J. Geophys. Res.*, 90:9749, 1985. doi:10.1029/JA090iA10p09749.

[32] W. T. Roberts, Jr., J. L. Horwitz, R. H. Comfort, C. R. Chappell, J. H. Waite, Jr., and J. L. Green. Heavy ion density enhancements in the outer plasmasphere. *J. Geophys. Res.*, 92:13499, 1987. doi:10.1029/JA092iA12p13499.

[33] L. Andersson, W. K. Peterson, and K. M. McBryde. Estimates of the suprathermal O^+ outflow characteristic energy and relative location in the auroral oval. *Geophys. Res. Lett.*, 32(9):L09104, May 2005. doi:10.1029/2004GL021434.

[34] J. Goldstein, C. R. Chappell, M. W. Davis, M. H. Denton, R. E. Denton, D. L. Gallagher, G. R. Gladstone, M. B. Lecocke, B. R. Sandel, and D. L. Windt. Imaging the Global Distribution of Plasmaspheric Oxygen. *Journal of Geophysical Research (Space Physics)*, 123(3):2078–2103, March 2018. doi:10.1002/2017JA024531.

[35] A. J. Hull, C. C. Chaston, J. W. Bonnell, J. R. Wygant, C. A. Keltzing, G. D. Reeves, and A. Gerrard. Dispersive Alfven wave control of O^+ ion outflow and energy densities in the inner magnetosphere. *Geophys. Res. Lett.*, 46, 2019. doi:10.1002/2019GL083808.

[36] J. Goldstein, M. Spasojević, P. H. Reiff, B. R. Sandel, W. T. Forrester, D. L. Gallagher, and B. W. Reinisch. Identifying the plasmapause in IMAGE EUV data using IMAGE RPI in situ steep density gradients. *Journal of Geophysical Research (Space Physics)*, 108:1147, April 2003. doi:10.1029/2002JA009475.

[37] J. Goldstein, D. Gallagher, P. D. Craven, R. H. Comfort, K. J. Genestreti, C. Mouikis, H. Spence, W. Kurth, J. Wygant, R. M. Skoug, B. A. Larsen, G. D. Reeves, and S. De Pascuale. Temperature Dependence of Plasmaspheric Ion Composition. *Journal of Geophysical Research (Space Physics)*, 124(8):6585–6595, August 2019. doi:10.1029/2019JA026822.

[38] J. F. Lemaire and K. I. Gringauz. *The Earth's Plasmasphere*. Cambridge University Press, Cambridge, 1998. doi:10.1017/CBO9780511600098.

[39] Fabien Darrouzet, Dennis L Gallagher, Nicolas André, Donald L Carpenter, Iannis Dandouras, Pierrette ME Décréau, Johan De Keyser, Richard E Denton, John C Foster, Jerry Goldstein, et al. Plasmaspheric density structures and dynamics: Properties observed by the cluster and image missions. *Space Science Reviews*, 145(1-2):55–106, 2009.

[40] JC Foster, W Rideout, B Sandel, WT Forrester, and FJ Rich. On the relationship of saps to storm-enhanced density. *Journal of Atmospheric and Solar-Terrestrial Physics*, 69(3):303–313, 2007.

[41] PC Anderson, RA Heelis, and WB Hanson. The ionospheric signatures of rapid subauroral ion drifts. *Journal of Geophysical Research: Space Physics*, 96(A4):5785–5792, 1991.

[42] V Pierrard and JF Lemaire. Development of shoulders and plumes in the frame of the interchange instability mechanism for plasmapause formation. *Geophysical research letters*, 31(5), 2004.

[43] Joseph E Borovsky, Michael H Denton, Richard E Denton, Vania K Jordanova, and Jonathan Krall. Estimating the effects of ionospheric plasma on solar wind/magnetosphere coupling via mass loading of dayside reconnection: Ion-plasma-sheet oxygen, plasmaspheric drainage plumes, and the plasma cloak. *Journal of Geophysical Research: Space Physics*, 118(9):5695–5719, 2013.

[44] DL Gallagher and RH Comfort. Unsolved problems in plasmasphere refilling. *Journal of Geophysical Research: Space Physics*, 121(2):1447–1451, 2016.

[45] H. Matsui, R. B. Torbert, H. E. Spence, Yu. V. Khotyaintsev, and P. A. Lindqvist. Revision of empirical electric field modeling in the inner magnetosphere using Cluster data. *Journal of Geophysical Research (Space Physics)*, 118(7):4119–4134, July 2013. doi:10.1002/jgra.50373.

[46] P. C. Anderson, R. A. Heelis, and W. B. Hanson. The ionospheric signatures of rapid subauroral ion drifts. *J. Geophys. Res.*, 96(A4):5785–5792, April 1991. doi:10.1029/90JA02651.

[47] J. C. Foster and W. J. Burke. SAPS: A new categorization for sub-auroral electric fields. *EOS Transactions*, 83(36):393, January 2002. doi:10.1029/2002EO000289.

[48] J. Goldstein and B. R. Sandel. The Global Pattern of Evolution of Plasmaspheric Drainage Plumes. *Washington DC American Geophysical Union Geophysical Monograph Series*, 159:1, 2005.

[49] F. Darrouzet, J. de Keyser, P. M. E. Décréau, F. El Lemdani-Mazouz, and X. Vallières. Statistical analysis of plasmaspheric plumes with Cluster/WHISPER observations. *Annales Geophysicae*, 26(8):2403–2417, August 2008. doi:10.5194/angeo-26-2403-2008.

[50] J. C. Foster, P. J. Erickson, B. M. Walsh, J. R. Wygant, A. J. Coster, and Qing-He Zhang. *Multi-Point Observations of the Geospace Plume*, chapter 14, pages 243–264. American Geophysical Union (AGU), 2020. URL: https://agupubs.onlinelibrary.wiley.com/doi/abs/10.1002/9781119509592.ch14, arXiv:https://agupubs.onlinelibrary.wiley.com/doi/pdf/10.1002/9781119509592.ch14, doi:https://doi.org/10.1002/9781119509592.ch14.

[51] R. C. Elphic, M. F. Thomsen, and J. E. Borovsky. The fate of the outer plasmasphere. *Geophysical Research Letters*, 24(4):365–368, January 1997. doi:10.1029/97GL00141.

[52] Michael W. Liemohn, Aaron J. Ridley, Dennis L. Gallagher, Daniel M. Ober, and Janet U. Kozyra. Dependence of plasmaspheric morphology on the electric field description during the recovery phase of the 17 April 2002 magnetic storm. *Journal of Geophysical Research (Space Physics)*, 109(A3):A03209, March 2004. doi:10.1029/2003JA010304.

[53] Robert L. Lysak. Electrodynamic coupling of the magnetosphere and ionosphere. *Space Sci. Rev.*, 52(1-2):33–87, February 1990. doi:10.1007/BF00704239.

[54] Andrew N. Wright. Transfer of magnetosheath momentum and energy to the ionosphere along open field lines. *Journal of Geophysical Research: Space Physics*, 101(A6):13169–13178, 1996. URL: https://agupubs.onlinelibrary.wiley.com/doi/abs/10.1029/96JA00541, arXiv:https://agupubs.onlinelibrary.wiley.com/doi/pdf/10.1029/96JA00541, doi:https://doi.org/10.1029/96JA00541.

[55] Scot R. Elkington, Mary K. Hudson, and Anthony A. Chan. Resonant acceleration and diffusion of outer zone electrons in an asymmetric geomagnetic field. *Journal of Geophysical Research (Space Physics)*, 108(A3):1116, March 2003. doi:10.1029/2001JA009202.

[56] Drew L. Turner, Yuri Shprits, Michael Hartinger, and Vassilis Angelopoulos. Explaining sudden losses of outer radiation belt electrons during geomagnetic storms. *Nature Physics*, 8(3):208–212, March 2012. doi:10.1038/nphys2185.

[57] A. N. Jaynes, D. N. Baker, H. J. Singer, J. V. Rodriguez, T. M. Loto'aniu, A. F. Ali, S. R. Elkington, X. Li, S. G. Kanekal, J. F. Fennell, W. Li, R. M. Thorne, C. A. Kletzing, H. E. Spence, and G. D. Reeves. Source and seed populations for relativistic electrons: Their roles in radiation belt changes. *Journal of Geophysical Research (Space Physics)*, 120:7240–7254, September 2015. doi:10.1002/2015JA021234.

[58] W. Baumjohann, G. Paschmann, and C. A. Cattell. Average plasma properties in the central plasma sheet. *Journal of Geophysical Research*, 94(A6):6597–6606, June 1989. doi:10.1029/JA094iA06p06597.

[59] V. Angelopoulos, W. Baumjohann, C. F. Kennel, F. V. Coroniti, M. G. Kivelson, R. Pellat, R. J. Walker, H. Luhr, and G. Paschmann. Bursty bulk flows in

the inner central plasma sheet. *Journal of Geophysical Research: Space Physics*, 97(A4):4027–4039, 1992. URL: https://agupubs.onlinelibrary.wiley.com/doi/abs/10.1029/91JA02701, arXiv:https://agupubs.onlinelibrary.wiley.com/doi/pdf/10.1029/91JA02701, doi:https://doi.org/10.1029/91JA02701.

[60] V. Angelopoulos, C. F. Kennel, F. V. Coroniti, R. Pellat, M. G. Kivelson, R. J. Walker, C. T. Russell, W. Baumjohann, W. C. Feldman, and J. T. Gosling. Statistical characteristics of bursty bulk flow events. *Journal of Geophysical Research*, 99(A11):21257–21280, November 1994. doi:10.1029/94JA01263.

[61] A. Runov, V. Angelopoulos, X.-Z. Zhou, X.-J. Zhang, S. Li, F. Plaschke, and J. Bonnell. A THEMIS multicase study of dipolarization fronts in the magnetotail plasma sheet. *Journal of Geophysical Research (Space Physics)*, 116:5216, May 2011. doi:10.1029/2010JA016316.

[62] M. Wiltberger, V. Merkin, J. G. Lyon, and S. Ohtani. High-resolution global magnetohydrodynamic simulation of bursty bulk flows. *Journal of Geophysical Research (Space Physics)*, 120(6):4555–4566, June 2015. doi:10.1002/2015JA021080.

[63] J. W. Dungey. Interplanetary Magnetic Field and the Auroral Zones. *Physical Review Letters*, 6(2):47–48, January 1961. doi:10.1103/PhysRevLett.6.47.

[64] G. D. Reeves, M. G. Henderson, P. S. McLachlan, R. D. Belian, R. H. W. Friedel, and A. Korth. Radial propagation of substorm injections. In E. J. Rolfe and B. Kaldeich, editors, *International Conference on Substorms*, volume 389 of *ESA Special Publication*, page 579, October 1996.

[65] R. L. McPherron, T.-S. Hsu, J. Kissinger, X. Chu, and V. Angelopoulos. Characteristics of plasma flows at the inner edge of the plasma sheet. *Journal of Geophysical Research (Space Physics)*, 116:0, April 2011. doi:10.1029/2010JA015923.

[66] D.M. Malaspina, J.R. Wygant, R.E. Ergun, G.D. Reeves, R.M. Skoug, and B.A. Larsen. Electric field structures and waves at plasma boundaries in the inner magnetosphere. *Journal of Geophysical Research (Space Physics)*, 120, May 2015. doi:10.1002/2015JA021137.

[67] V. A. Sergeev, K. Liou, C. I. Meng, P. T. Newell, M. Brittnacher, G. Parks, and G. D. Reeves. Development of auroral streamers in association with localized impulsive injections to the inner magnetotail. *Geophysical Research Letters*, 26(3):417–420, January 1999. doi:10.1029/1998GL900311.

[68] V. A. Sergeev, J. A. Sauvaud, D. Popescu, R. A. Kovrazhkin, K. Liou, P. T. Newell, M. Brittnacher, G. Parks, R. Nakamura, T. Mukai, and G. D. Reeves. Multiple-spacecraft observation of a narrow transient plasma jet in the Earth's plasma sheet. *Geophysical Research Letters*, 27(6):851–854, March 2000. doi:10.1029/1999GL010729.

[69] J. R. Wygant, A. Keiling, C. A. Cattell, M. Johnson, R. L. Lysak, M. Temerin, F. S. Mozer, C. A. Kletzing, J. D. Scudder, W. Peterson, C. T. Russell, G. Parks, M. Brittnacher, G. Germany, and J. Spann. Polar spacecraft based comparisons of intense electric fields and Poynting flux near and within the plasma sheet-tail lobe boundary to UVI images: An energy source for the aurora. *Journal of Geophysical Research*, 105(A8):18,675–18,692, August 2000. doi:10.1029/1999JA900500.

[70] R. Nakamura, W. Baumjohann, R. Schödel, M. Brittnacher, V. A. Sergeev, M. Kubyshkina, T. Mukai, and K. Liou. Earthward flow bursts, auroral streamers, and small expansions. *Journal of Geophysical Research*, 106(A6):10791–10802, June 2001. doi:10.1029/2000JA000306.

[71] J. E. Stawarz, R. E. Ergun, and K. A. Goodrich. Generation of high-frequency electric field activity by turbulence in the Earth's magnetotail. *Journal of Geophysical Research (Space Physics)*, 120(3):1845–1866, March 2015. doi:10.1002/2014JA020166.

[72] Leng Ying Khoo, Xinlin Li, Hong Zhao, Theodore E. Sarris, Zheng Xiang, Kun Zhang, Adam C. Kellerman, and J. Bernard Blake. On the Initial Enhancement of Energetic Electrons and the Innermost Plasmapause Locations: Coronal Mass Ejection-Driven Storm Periods. *Journal of Geophysical Research (Space Physics)*, 123(11):9252–9264, November 2018. doi:10.1029/2018JA026074.

[73] S. S. Li, V. Angelopoulos, A. Runov, X. Z. Zhou, J. McFadden, D. Larson, J. Bonnell, and U. Auster. On the force balance around dipolarization fronts within bursty bulk flows. *Journal of Geophysical Research (Space Physics)*, 116(A5):A00I35, May 2011. doi:10.1029/2010JA015884.

[74] D. L. Turner, S. G. Claudepierre, J. F. Fennell, T. P. O'Brien, J. B. Blake, C. Lemon, M. Gkioulidou, K. Takahashi, G. D. Reeves, S. Thaller, A. Breneman, J. R. Wygant, W. Li, A. Runov, and V. Angelopoulos. Energetic electron injections deep into the inner magnetosphere associated with substorm activity. *Geophys. Res. Lett.*, 42(7):2079–2087, April 2015. doi:10.1002/2015GL063225.

[75] D. L. Turner, J. F. Fennell, J. B. Blake, S. G. Claudepierre, J. H. Clemmons, A. N. Jaynes, T. Leonard, D. N. Baker, I. J. Cohen, M. Gkioulidou, A. Y. Ukhorskiy, B. H. Mauk, C. Gabrielse, V. Angelopoulos, R. J. Strangeway, C. A. Kletzing, O. Le Contel, H. E. Spence, R. B. Torbert, J. L. Burch, and G. D. Reeves. Multipoint Observations of Energetic Particle Injections and Substorm Activity During a Conjunction Between Magnetospheric Multiscale (MMS) and Van Allen Probes. *Journal of Geophysical Research (Space Physics)*, 122(11):11,481–11,504, November 2017. doi:10.1002/2017JA024554.

[76] A. Glocer, D. Welling, C. R. Chappell, G. Toth, M.-C. Fok, C. Komar, S.-B. Kang, N. Buzulukova, C. Ferradas, S. Bingham, and C. Mouikis. A case study on the origin of near-earth plasma. *Journal of Geophysical Research: Space Physics*, 125(11):e2020JA028205, 2020. e2020JA028205 10.1029/2020JA028205. URL:

https://agupubs.onlinelibrary.wiley.com/doi/abs/10.1029/2020JA028205, arXiv:https://agupubs.onlinelibrary.wiley.com/doi/pdf/10.1029/2020JA028205, doi:https://doi.org/10.1029/2020JA028205.

[77] T. Motoba, S. Ohtani, S. G. Claudepierre, G. D. Reeves, A. Y. Ukhorskiy, and L. J. Lanzerotti. Dynamic Properties of Particle Injections Inside Geosynchronous Orbit: A Multisatellite Case Study. *Journal of Geophysical Research (Space Physics)*, 125(9):e28215, September 2020. doi:10.1029/2020JA028215.

[78] Hayley J. Allison, Yuri Y. Shprits, Irina S. Zhelavskaya, Dedong Wang, and Artem G. Smirnov. Gyroresonant wave-particle interactions with chorus waves during extreme depletions of plasma density in the Van Allen radiation belts. *Science Advances*, 7(5):eabc0380, January 2021. doi:10.1126/sciadv.abc0380.

[79] Kareem A. Sorathia, Aleksandr Y. Ukhorskiy, Viacheslav G. Merkin, Joseph F. Fennell, and Seth G. Claudepierre. Modeling the Depletion and Recovery of the Outer Radiation Belt During a Geomagnetic Storm: Combined MHD and Test Particle Simulations. *Journal of Geophysical Research (Space Physics)*, 123(7):5590–5609, July 2018. doi:10.1029/2018JA025506.

[80] C. C. Chaston, J. W. Bonnell, G. D. Reeves, and R. M. Skoug. Driving ionospheric outflows and magnetospheric O^+ energy density with Alfvén waves. *Geophysical Research Letters*, 43:4825–4833, May 2016. doi:10.1002/2016GL069008.

[81] J. Liu, V. Angelopoulos, X.-J. Zhang, D. L. Turner, C. Gabrielse, A. Runov, J. Li, H. O. Funsten, and H. E. Spence. Dipolarizing flux bundles in the cis-geosynchronous magnetosphere: Relationship between electric fields and energetic particle injections. *Journal of Geophysical Research (Space Physics)*, 121:1362–1376, February 2016. doi:10.1002/2015JA021691.

[82] Jian Yang, Frank R. Toffoletto, and Richard A. Wolf. RCM-E simulation of a thin arc preceded by a north-south-aligned auroral streamer. *Geophysical Research Letters*, 41(8):2695–2701, April 2014. doi:10.1002/2014GL059840.

[83] Jiang Liu, V. Angelopoulos, Xu-Zhi Zhou, Zhong-Hua Yao, and A. Runov. Cross-tail expansion of dipolarizing flux bundles. *Journal of Geophysical Research (Space Physics)*, 120(4):2516–2530, April 2015. doi:10.1002/2015JA020997.

[84] Alex C. Fletcher, Chris Crabtree, Gurudas Ganguli, David Malaspina, Erik Tejero, and Xiangning Chu. Kinetic Equilibrium and Stability Analysis of Dipolarization Fronts. *Journal of Geophysical Research (Space Physics)*, 124(3):2010–2028, March 2019. doi:10.1029/2018JA026433.

[85] R. B. Horne, R. M. Thorne, Y. Y. Shprits, N. P. Meredith, S. A. Glauert, A. J. Smith, S. G. Kanekal, D. N. Baker, M. J. Engebretson, J. L. Posch, M. Spasojevic, U. S. Inan, J. S. Pickett, and P. M. E. Decreau. Wave acceleration of electrons in the Van Allen radiation belts. *Nature*, 437:227–230, September 2005. doi:10.1038/nature03939.

[86] R. M. Thorne. Radiation belt dynamics: The importance of wave-particle interactions. *Geophysical Review Letters*, 37:22107, November 2010. doi:10.1029/2010GL044990.

[87] D. Summers, R. M. Thorne, and F. Xiao. Relativistic theory of wave-particle resonant diffusion with application to electron acceleration in the magnetosphere. *Journal of Geophysical Research*, 103:20487–20500, September 1998. doi:10.1029/98JA01740.

[88] Y. Omura, N. Furuya, and D. Summers. Relativistic turning acceleration of resonant electrons by coherent whistler mode waves in a dipole magnetic field. *Journal of Geophysical Research (Space Physics)*, 112:6236, June 2007. doi:10.1029/2006JA012243.

[89] D. T. Young, S. Perraut, A. Roux, C. de Villedary, R. Gendrin, A. Korth, G. Kremser, and D. Jones. Wave-particle interactions near Ω_{He+} observed in GEOS 1 and 2 1. Propagation of ion cyclotron waves in He^+ -rich plasma. *Journal of Geophysical Research*, 86(A8):6755–6772, August 1981. doi:10.1029/JA086iA08p06755.

[90] J. U. Kozyra, T. E. Cravens, A. F. Nagy, E. G. Fontheim, and R. S. B. Ong. Effects of energetic heavy ions on electromagnetic ion cyclotron wave generation in the plasmapause region. *Journal of Geophysical Research*, 89(A4):2217–2234, April 1984. doi:10.1029/JA089iA04p02217.

[91] B. Ni, W. Li, R. M. Thorne, J. Bortnik, Q. Ma, L. Chen, C. A. Kletzing, W. S. Kurth, G. B. Hospodarsky, G. D. Reeves, H. E. Spence, J. Bernard Blake, J. F. Fennell, and S. G. Claudepierre. Resonant scattering of energetic electrons by unusual low-frequency hiss. *Geophysical Review Letters*, 41:1854–1861, March 2014. doi:10.1002/2014GL059389.

[92] N. P. Meredith, R. B. Horne, T. Kersten, W. Li, J. Bortnik, A. Sicard, and K. H. Yearby. Global Model of Plasmaspheric Hiss From Multiple Satellite Observations. *Journal of Geophysical Research (Space Physics)*, 123:4526–4541, June 2018. doi:10.1029/2018JA025226.

[93] Wenxun Zhang, Song Fu, Xudong Gu, Binbin Ni, Zheng Xiang, Danny Summers, Zhengyang Zou, Xing Cao, Yuequn Lou, and Man Hua. Electron Scattering by Plasmaspheric Hiss in a Nightside Plume. *Geophys. Res. Lett.*, 45(10):4618–4627, May 2018. doi:10.1029/2018GL077212.

[94] Fei He, Rui-Long Guo, William R. Dunn, Zhong-Hua Yao, Hua-Sen Zhang, Yi-Xin Hao, Quan-Qi Shi, Zhao-Jin Rong, Jiang Liu, An-Min Tian, Xiao-Xin Zhang, Yong Wei, Yong-Liang Zhang, Qiu-Gang Zong, Zu-Yin Pu, and Wei-Xing Wan. Plasmapause surface wave oscillates the magnetosphere and diffuse aurora. *Nature Communications*, 11:1668, April 2020. doi:10.1038/s41467-020-15506-3.

[95] David M. Malaspina, Hui Zhu, and Alexander Y. Drozdov. A Wave Model and Diffusion Coefficients for Plasmaspheric Hiss Parameterized by Plasmapause Location. *Journal of Geophysical Research (Space Physics)*, 125(2):e27415, February 2020. doi:10.1029/2019JA027415.

[96] Nigel P. Meredith, Richard B. Horne, Xiao-Chen Shen, Wen Li, and Jacob Bortnik. Global Model of Whistler Mode Chorus in the Near-Equatorial Region (—λ_m—¡ 18°). *Geophysical Research Letters*, 47(11):e87311, May 2020. doi:10.1029/2020GL087311.

[97] A. N. Jaynes, A. F. Ali, S. R. Elkington, D. M. Malaspina, D. N. Baker, X. Li, S. G. Kanekal, M. G. Henderson, C. A. Kletzing, and J. R. Wygant. Fast Diffusion of Ultrarelativistic Electrons in the Outer Radiation Belt: 17 March 2015 Storm Event. *Geophys. Res. Lett.*, 45(20):10,874–10,882, October 2018. doi:10.1029/2018GL079786.

[98] C. E. J. Watt, H. J. Allison, N. P. Meredith, R. L. Thompson, S. N. Bentley, I. J. Rae, S. A. Glauert, and R. B. Horne. Variability of Quasilinear Diffusion Coefficients for Plasmaspheric Hiss. *Journal of Geophysical Research (Space Physics)*, 124(11):8488–8506, November 2019. doi:10.1029/2018JA026401.

[99] A. J. Halford, B. J. Fraser, and S. K. Morley. EMIC waves and plasmaspheric and plume density: CRRES results. *Journal of Geophysical Research (Space Physics)*, 120(3):1974–1992, March 2015. doi:10.1002/2014JA020338.

[100] M. J. Engebretson, J. L. Posch, J. R. Wygant, C. A. Kletzing, M. R. Lessard, C. L. Huang, H. E. Spence, C. W. Smith, H. J. Singer, Y. Omura, R. B. Horne, G. D. Reeves, D. N. Baker, M. Gkioulidou, K. Oksavik, I. R. Mann, T. Raita, and K. Shiokawa. Van Allen probes, NOAA, GOES, and ground observations of an intense EMIC wave event extending over 12 h in magnetic local time. *Journal of Geophysical Research (Space Physics)*, 120(7):5465–5488, July 2015. doi:10.1002/2015JA021227.

[101] D. M. Malaspina, A. N. Jaynes, G. Hospodarsky, J. Bortnik, R. E. Ergun, and J. Wygant. Statistical properties of low-frequency plasmaspheric hiss. *Journal of Geophysical Research (Space Physics)*, 122:8340–8352, August 2017. doi:10.1002/2017JA024328.

[102] National Aeronautics and Space Administration. Science 2020-2024: A vision for scientific excellence. Technical report, NASA, Washington DC, 2020.

[103] Small Spacecraft Systems Virtual Institute. State-of-the-art small spacecraft technology, NASA TP 2020 5008734. Technical report, Ames Research Center, Moffett Field, California, 2020.

[104] R. E. Ergun, D. E. Larson, T. Phan, D. Taylor, S. Bale, C. W. Carlson, I. Roth, V. Angelopoulos, J. Raeder, T. Bell, U. S. Inan, J. L. Bougeret, and R. Manning. Feasibility

of a multisatellite investigation of the Earth's magnetosphere with radio tomography. *J. Geophys. Res.*, 105(A1):361–374, January 2000. doi:10.1029/1999JA900170.

[105] J. G. Trotignon, P. M. E. Décréau, J. L. Rauch, E. Le Guirriec, P. Canu, and F. Darrouzet. The Whisper Relaxation Sounder Onboard Cluster: A Powerful Tool for Space Plasma Diagnosis around the Earth. *Cosmic Research*, 41:345–348, July 2003.

[106] L. Andersson, T. D. Weber, D. Malaspina, F. Crary, R. E. Ergun, G. T. Delory, C. M. Fowler, M. W. Morooka, T. McEnulty, A. I. Eriksson, D. J. Andrews, M. Horanyi, A. Collette, R. Yelle, and B. M. Jakosky. Dust observations at orbital altitudes surrounding Mars. *Science*, 350(6261):0398, Nov 2015. doi:10.1126/science.aad0398.

[107] R. C. Elphic, J. D. Means, R. C. Snare, R. J. Strangeway, L. Kepko, and R. E. Ergun. Magnetic Field Instruments for the Fast Auroral Snapshot Explorer. *Space Science Reviews*, 98:151–168, August 2001. doi:10.1023/A:1013153623344.

[108] Nils Olsen, Giuseppe Albini, Jerome Bouffard, Tommaso Parrinello, and Lars Tøffner-Clausen. Magnetic observations from CryoSat-2: calibration and processing of satellite platform magnetometer data. *Earth, Planets and Space*, 72(1):48, April 2020. doi:10.1186/s40623-020-01171-9.

[109] F. S. Mozer. DC and low-frequency double probe electric field measurements in space. *Journal of Geophysical Research (Space Physics)*, 121(11):10,942–10,953, November 2016. doi:10.1002/2016JA022952.

[110] B. H. Mauk, N. J. Fox, S. G. Kanekal, R. L. Kessel, D. G. Sibeck, and A. Ukhorskiy. Science Objectives and Rationale for the Radiation Belt Storm Probes Mission. *Space Science Reviews*, 179:3–27, November 2013. doi:10.1007/s11214-012-9908-y.

[111] J. R. Wygant, J. W. Bonnell, K. Goetz, R. E. Ergun, F. S. Mozer, S. D. Bale, M. Ludlam, P. Turin, P. R. Harvey, R. Hochmann, K. Harps, G. Dalton, J. McCauley, W. Rachelson, D. Gordon, B. Donakowski, C. Shultz, C. Smith, M. Diaz-Aguado, J. Fischer, S. Heavner, P. Berg, D. M. Malsapina, M. K. Bolton, M. Hudson, R. J. Strangeway, D. N. Baker, X. Li, J. Albert, J. C. Foster, C. C. Chaston, I. Mann, E. Donovan, C. M. Cully, C. A. Cattell, V. Krasnoselskikh, K. Kersten, A. Breneman, and J. B. Tao. The Electric Field and Waves Instruments on the Radiation Belt Storm Probes Mission. *Space Science Reviews*, 179:183–220, November 2013. doi:10.1007/s11214-013-0013-7.

[112] C. A. Kletzing, W. S. Kurth, M. Acuna, R. J. MacDowall, R. B. Torbert, T. Averkamp, D. Bodet, S. R. Bounds, M. Chutter, J. Connerney, D. Crawford, J. S. Dolan, R. Dvorsky, G. B. Hospodarsky, J. Howard, V. Jordanova, R. A. Johnson, D. L. Kirchner, B. Mokrzycki, G. Needell, J. Odom, D. Mark, R. Pfaff, J. R. Phillips, C. W. Piker, S. L. Remington, D. Rowland, O. Santolik, R. Schnurr, D. Sheppard, C. W. Smith, R. M. Thorne, and J. Tyler. The Electric and Magnetic Field Instrument Suite and Integrated Science (EMFISIS) on RBSP. *Space Science Reviews*, 179:127–181, November 2013. doi:10.1007/s11214-013-9993-6.

[113] V. Angelopoulos. The THEMIS Mission. *Space Science Reviews*, 141:5–34, December 2008. doi:10.1007/s11214-008-9336-1.

[114] J. W. Bonnell, F. S. Mozer, G. T. Delory, A. J. Hull, R. E. Ergun, C. M. Cully, V. Angelopoulos, and P. R. Harvey. The Electric Field Instrument (EFI) for THEMIS. *Space Science Reviews*, 141:303–341, December 2008. doi:10.1007/s11214-008-9469-2.

[115] J. L. Burch, T. E. Moore, R. B. Torbert, and B. L. Giles. Magnetospheric Multiscale Overview and Science Objectives. *Space Science Reviews*, May 2015. doi:10.1007/s11214-015-0164-9.

[116] R. B. Torbert, C. T. Russell, W. Magnes, R. E. Ergun, P. A. Lindqvist, O. Le Contel, H. Vaith, J. Macri, S. Myers, D. Rau, J. Needell, B. King, M. Granoff, M. Chutter, I. Dors, G. Olsson, Y. V. Khotyaintsev, A. Eriksson, C. A. Kletzing, S. Bounds, B. Anderson, W. Baumjohann, M. Steller, K. Bromund, Guan Le, R. Nakamura, R. J. Strangeway, H. K. Leinweber, S. Tucker, J. Westfall, D. Fischer, F. Plaschke, J. Porter, and K. Lappalainen. The FIELDS Instrument Suite on MMS: Scientific Objectives, Measurements, and Data Products. *Space Science Reviews*, 199(1-4):105–135, March 2016. doi:10.1007/s11214-014-0109-8.

[117] J. G. Trotignon, P. M. E. Décréau, J. L. Rauch, X. Vallières, A. Rochel, S. Kougblénou, G. Lointier, G. Facskó, P. Canu, F. Darrouzet, and A. Masson. The WHISPER Relaxation Sounder and the CLUSTER Active Archive. In *The Cluster Active Archive*, volume 11 of *Astrophysics and Space Science Proceedings*, pages 185–208, January 2010. doi:10.1007/978-90-481-3499-1_12.

[118] H. O. Funsten, R. M. Skoug, A. A. Guthrie, E. A. MacDonald, J. R. Baldonado, R. W. Harper, K. C. Henderson, K. H. Kihara, J. E. Lake, B. A. Larsen, A. D. Puckett, V. J. Vigil, R. H. Friedel, M. G. Henderson, J. T. Niehof, G. D. Reeves, M. F. Thomsen, J. J. Hanley, D. E. George, J.-M. Jahn, S. Cortinas, A. De Los Santos, G. Dunn, E. Edlund, M. Ferris, M. Freeman, M. Maple, C. Nunez, T. Taylor, W. Toczynski, C. Urdiales, H. E. Spence, J. A. Cravens, L. L. Suther, and J. Chen. Helium, Oxygen, Proton, and Electron (HOPE) Mass Spectrometer for the Radiation Belt Storm Probes Mission. *Space Science Reviews*, 179:423–484, November 2013. doi:10.1007/s11214-013-9968-7.

[119] C. R. Chappell, S. A. Fields, C. R. Baugher, J. H. Hoffman, W. B. Hanson, W. W. Wright, H. D. Hammack, G. R. Carignan, and A. F. Nagy. The Retarding Ion Mass Spectrometer on Dynamics Explorer-A. *Space Science Instrumentation*, 5:477–491, December 1981.

[120] B. L. Giles, C. R. Chappell, T. E. Moore, R. H. Comfort, and Jr. Waite, J. H. Statistical survey of pitch angle distributions in core (0-50 eV) ions from Dynamics Explorer 1: Outflow in the auroral zone, polar cap, and cusp. *Journal of Geophysical Research*, 99(A9):17483–17502, September 1994. doi:10.1029/94JA00864.

[121] B. A. Whalen, D. J. Knudsen, A. W. Yau, A. M. Pilon, T. A. Cameron, J. F. Sebesta, D. J. McEwen, J. A. Koehler, N. D. Lloyd, G. Pocobelli, J. G. Laframboise, W. Li, R. Lundin, L. Eliasson, S. Watanabe, and G. S. Campbell. The Freja F3C Cold Plasma Analyzer. *Space Science Reviews*, 70(3-4):541–561, November 1994. doi:10.1007/BF00756885.

[122] D. J. Knudsen, J. K. Burchill, T. G. Cameron, G. A. Enno, A. Howarth, and A. W. Yau. The CASSIOPE/e-POP Suprathermal Electron Imager (SEI). *Space Science Reviews*, 189(1-4):65–78, June 2015. doi:10.1007/s11214-015-0151-1.

[123] L. W. Blum, L. Kepko, D. Turner, C. Gabrielse, A. Jaynes, S. Kanekal, Q. Schiller, J. Espley, D. Sheppard, L. Santos, J. Lucas, and S. West. The GTOSat CubeSat: scientific objectives and instrumentation. In Thomas George and M. Saif Islam, editors, *Micro- and Nanotechnology Sensors, Systems, and Applications XII*, volume 11389, pages 62 – 71. International Society for Optics and Photonics, SPIE, 2020. doi:10.1117/12.2556268.

[124] J. B. Blake, P. A. Carranza, S. G. Claudepierre, J. H. Clemmons, W. R. Crain, Y. Dotan, J. F. Fennell, F. H. Fuentes, R. M. Galvan, J. S. George, M. G. Henderson, M. Lalic, A. Y. Lin, M. D. Looper, D. J. Mabry, J. E. Mazur, B. McCarthy, C. Q. Nguyen, T. P. O'Brien, M. A. Perez, M. T. Redding, J. L. Roeder, D. J. Salvaggio, G. A. Sorensen, H. E. Spence, S. Yi, and M. P. Zakrzewski. The Magnetic Electron Ion Spectrometer (MagEIS) Instruments Aboard the Radiation Belt Storm Probes (RBSP) Spacecraft. *Space Science Reviews*, 179:383–421, November 2013. doi:10.1007/s11214-013-9991-8.

[125] J. Goldstein, D.L. Gallagher, B.R. Sandel, M. Davis, P. Molyneux, T. Veach, G. Fletcher, E. Gullikson, D. Windt, D.D. Allred, and R.S. Turley. Chapter 6 - the future of plasmaspheric extreme ultraviolet (euv) imaging. In Yaireska Colado-Vega, Dennis Gallagher, Harald Frey, and Simon Wing, editors, *Understanding the Space Environment through Global Measurements*, pages 231–286. Elsevier, 2022. URL: https://www.sciencedirect.com/science/article/pii/B9780128206300000106, doi:https://doi.org/10.1016/B978-0-12-820630-0.00010-6.

[126] B. R. Sandel, A. L. Broadfoot, C. C. Curtis, R. A. King, T. C. Stone, R. H. Hill, J. Chen, O. H. W. Siegmund, R. Raffanti, DAVID D. Allred, R. STEVEN Turley, and D. L. Gallagher. The Extreme Ultraviolet Imager Investigation for the IMAGE Mission. *Space Sci. Rev.*, 91:197–242, January 2000. doi:10.1023/A:1005263510820.

[127] Michael W. Davis, G. Randall Gladstone, Jerry Goldstein, Bill R. Sandel, Thomas K. Greathouse, Kurt D. Retherford, and Gregory S. Winters. An improved wide-field camera for imaging Earth's plasmasphere at 30.4 nm. In Oswald H. Siegmund, editor, *UV, X-Ray, and Gamma-Ray Space Instrumentation for Astronomy XVIII*, volume 8859, pages 227 – 235. International Society for Optics and Photonics, SPIE, 2013. doi:10.1117/12.2024440.

[128] Michael David, J. J. Sojka, R. W. Schunk, and A. J. Coster. Polar cap patches and the tongue of ionization: A survey of gps tec maps from 2009 to 2015. *Geophysical Research Letters*, 43(6):2422–2428, 2016. URL: https://agupubs.onlinelibrary.wiley.com/doi/abs/10.1002/2016GL068136, arXiv:https://agupubs.onlinelibrary.wiley.com/doi/pdf/10.1002/2016GL068136, doi:https://doi.org/10.1002/2016GL068136.

[129] G. Chisham, M. Lester, S. E. Milan, M. P. Freeman, W. A. Bristow, A. Grocott, K. A. McWilliams, J. M. Ruohoniemi, T. K. Yeoman, P. L. Dyson, R. A. Greenwald, T. Kikuchi, M. Pinnock, J. P. S. Rash, N. Sato, G. J. Sofko, J. P. Villain, and A. D. M. Walker. A decade of the Super Dual Auroral Radar Network (SuperDARN): scientific achievements, new techniques and future directions. *Surveys in Geophysics*, 28(1):33–109, January 2007. doi:10.1007/s10712-007-9017-8.

[130] J. W. Gjerloev. The SuperMAG data processing technique. *Journal of Geophysical Research (Space Physics)*, 117(A9):A09213, September 2012. doi:10.1029/2012JA017683.

[131] S. D. Bale, R. Ullrich, K. Goetz, N. Alster, B. Cecconi, M. Dekkali, N. R. Lingner, W. Macher, R. E. Manning, J. McCauley, S. J. Monson, T. H. Oswald, and M. Pulupa. The Electric Antennas for the STEREO/WAVES Experiment. *Space Science Reviews*, 136:529–547, April 2008. doi:10.1007/s11214-007-9251-x.

[132] Naomi Maruyama, Yang-Yi Sun, Phillip G. Richards, Jacques Middlecoff, Tzu-Wei Fang, Timothy J. Fuller-Rowell, Rashid A. Akmaev, Jaun-Yeng Liu, and Cesar E. Valladares. A new source of the midlatitude ionospheric peak density structure revealed by a new Ionosphere-Plasmasphere model. *Geophysical Review Letters*, 43(6):2429–2435, March 2016. doi:10.1002/2015GL067312.

[133] J. G. Trotignon, P. M. E. Décréau, J. L. Rauch, O. Randriamboarison, V. Krasnoselskikh, P. Canu, H. Alleyne, K. Yearby, E. Le Guirriec, H. C. Séran, F. X. Sené, Ph. Martin, M. Lévêque, and P. Fergeau. How to determine the thermal electron density and the magnetic field strength from the Cluster/Whisper observations around the Earth. *Annales Geophysicae*, 19(10):1711–1720, October 2001. doi:10.5194/angeo-19-1711-2001.

[134] J. A. Slavin, G. Le, R. J. Strangeway, Y. Wang, S. A. Boardsen, M. B. Moldwin, and H. E. Spence. Space technology 5 multi-point measurements of near-earth magnetic fields: Initial results. *Geophysical Research Letters*, 35(2), 2008. URL: https://agupubs.onlinelibrary.wiley.com/doi/abs/10.1029/2007GL031728, arXiv:https://agupubs.onlinelibrary.wiley.com/doi/pdf/10.1029/2007GL031728, doi:https://doi.org/10.1029/2007GL031728.

[135] V. Angelopoulos, J. P. McFadden, D. Larson, C. W. Carlson, S. B. Mende, H. Frey, T. Phan, D. G. Sibeck, K.-H. Glassmeier, U. Auster, E. Donovan, I. R. Mann, I. J. Rae, C. T. Russell, A. Runov, X.-Z. Zhou, and L. Kepko. Tail Reconnection Triggering Substorm Onset. *Science*, 321:931–, August 2008. doi:10.1126/science.1160495.

[136] C. T. Russell, B. J. Anderson, W. Baumjohann, K. R. Bromund, D. Dearborn, D. Fischer, G. Le, H. K. Leinweber, D. Leneman, W. Magnes, J. D. Means, M. B. Moldwin, R. Nakamura, D. Pierce, F. Plaschke, K. M. Rowe, J. A. Slavin, R. J. Strangeway, R. Torbert, C. Hagen, I. Jernej, A. Valavanoglou, and I. Richter. The Magnetospheric Multiscale Magnetometers. *Space Science Reviews*, 199(1-4):189–256, March 2016. doi:10.1007/s11214-014-0057-3.

[137] Norman F. Ness, Kenneth W. Behannon, Ronald P. Lepping, and Kenneth H. Schatten. Use of two magnetometers for magnetic field measurements on a spacecraft. *Journal of Geophysical Research*, 76(16):3564, January 1971. doi:10.1029/JA076i016p03564.

[138] R. M. Millan, M. P. McCarthy, J. G. Sample, D. M. Smith, L. D. Thompson, D. G. McGaw, L. A. Woodger, J. G. Hewitt, M. D. Comess, K. B. Yando, A. X. Liang, B. A. Anderson, N. R. Knezek, W. Z. Rexroad, J. M. Scheiman, G. S. Bowers, A. J. Halford, A. B. Collier, M. A. Clilverd, R. P. Lin, and M. K. Hudson. The Balloon Array for RBSP Relativistic Electron Losses (BARREL). *Space Science Reviews*, 179(1-4):503–530, November 2013. doi:10.1007/s11214-013-9971-z.

[139] H. U. Auster, K. H. Glassmeier, W. Magnes, O. Aydogar, W. Baumjohann, D. Constantinescu, D. Fischer, K. H. Fornacon, E. Georgescu, P. Harvey, O. Hillenmaier, R. Kroth, M. Ludlam, Y. Narita, R. Nakamura, K. Okrafka, F. Plaschke, I. Richter, H. Schwarzl, B. Stoll, A. Valavanoglou, and M. Wiedemann. The THEMIS Fluxgate Magnetometer. *Space Science Reviews*, 141:235–264, December 2008. doi:10.1007/s11214-008-9365-9.

[140] S. D. Bale, K. Goetz, P. R. Harvey, P. Turin, J. W. Bonnell, T. Dudok de Wit, R. E. Ergun, R. J. MacDowall, M. Pulupa, M. Andre, M. Bolton, J. L. Bougeret, T. A. Bowen, D. Burgess, C. A. Cattell, B. D. G. Chandran, C. C. Chaston, C. H. K. Chen, M. K. Choi, J. E. Connerney, S. Cranmer, M. Diaz-Aguado, W. Donakowski, J. F. Drake, W. M. Farrell, P. Fergeau, J. Fermin, J. Fischer, N. Fox, D. Glaser, M. Goldstein, D. Gordon, E. Hanson, S. E. Harris, L. M. Hayes, J. J. Hinze, J. V. Hollweg, T. S. Horbury, R. A. Howard, V. Hoxie, G. Jannet, M. Karlsson, J. C. Kasper, P. J. Kellogg, M. Kien, J. A. Klimchuk, V. V. Krasnoselskikh, S. Krucker, J. J. Lynch, M. Maksimovic, D. M. Malaspina, S. Marker, P. Martin, J. Martinez-Oliveros, J. McCauley, D. J. McComas, T. McDonald, N. Meyer-Vernet, M. Moncuquet, S. J. Monson, F. S. Mozer, S. D. Murphy, J. Odom, R. Oliverson, J. Olson, E. N. Parker, D. Pankow, T. Phan, E. Quataert, T. Quinn, S. W. Ruplin, C. Salem, D. Seitz, D. A. Sheppard, A. Siy, K. Stevens, D. Summers, A. Szabo, M. Timofeeva, A. Vaivads, M. Velli, A. Yehle, D. Werthimer, and J. R. Wygant. The FIELDS Instrument Suite for Solar Probe Plus. Measuring the Coronal Plasma and Magnetic Field, Plasma Waves and Turbulence, and Radio Signatures of Solar Transients. *Space Science Reviews*, 204(1-4):49–82, December 2016. doi:10.1007/s11214-016-0244-5.

[141] M. I. Sitnov, N. A. Tsyganenko, A. Y. Ukhorskiy, and P. C. Brandt. Dynamical data-based modeling of the storm-time geomagnetic field with enhanced spatial resolution.

Journal of Geophysical Research (Space Physics), 113(A7):A07218, July 2008. doi:10.1029/2007JA013003.

[142] Justin H. Lee, Colin J. Mann, Don Walker, Drew L. Turner, J. Bernard Blake, William R. Crain, David A. Hinkley, Michael Mellick, Brian S. Hardy, and Simon H. Liu. Ground testing and instrument development for the aerocube-10 space solar cell experiment. In *2018 IEEE 7th World Conference on Photovoltaic Energy Conversion (WCPEC) (A Joint Conference of 45th IEEE PVSC, 28th PVSEC 34th EU PVSEC)*, pages 3364–3366, 2018. doi:10.1109/PVSC.2018.8547816.

[143] D. L. Turner, J. H. Lee, C. Q. Nguyen, Jr. Crain, W. R., A. L. Berman, and J. B. Blake. The micro-Charged Particle Telescope (µCPT) for the AeroCube-10 mission. In *AGU Fall Meeting Abstracts*, volume 2018, pages SH41D–3669, December 2018.

[144] Justin H. Lee, Simon H. Liu, Colin J. Mann, John C. Nocerino, Don Walker, J. Bernard Blake, William R. Crain, Ariel L. Berman, Garrett Kinum, Victor L. Chin, Mark D. Looper, Michael Mellick, Jacqueline A. Tardif, Christopher M. Coffman, Brian S. Hardy, and David A. Hinkley. First on-orbit results from the aerocube-10 space solar cell experiment. In *2020 47th IEEE Photovoltaic Specialists Conference (PVSC)*, pages 1738–1741, 2020. doi:10.1109/PVSC45281.2020.9300417.

[145] J. B. Blake, B. H. Mauk, D. N. Baker, P. Carranza, J. H. Clemmons, J. Craft, W. R. Crain, A. Crew, Y. Dotan, J. F. Fennell, R. H. Friedel, L. M. Friesen, F. Fuentes, R. Galvan, C. Ibscher, A. Jaynes, N. Katz, M. Lalic, A. Y. Lin, D. M. Mabry, T. Nguyen, C. Pancratz, M. Redding, G. D. Reeves, S. Smith, H. E. Spence, and J. Westlake. The Fly's Eye Energetic Particle Spectrometer (FEEPS) Sensors for the Magnetospheric Multiscale (MMS) Mission. *Space Science Reviews*, 199(1-4):309–329, March 2016. doi:10.1007/s11214-015-0163-x.

[146] G. B. Hospodarsky. Spaced-based search coil magnetometers. *Journal of Geophysical Research (Space Physics)*, 121(A10):12, December 2016. doi:10.1002/2016JA022565.

[147] D. M. Malaspina, A. N. Jaynes, C. Boulé, J. Bortnik, S. A. Thaller, R. E. Ergun, C. A. Kletzing, and J. R. Wygant. The distribution of plasmaspheric hiss wave power with respect to plasmapause location. *Geophysical Review Letters*, 43:7878–7886, August 2016. doi:10.1002/2016GL069982.

[148] Solène Lejosne, John W. Bonnell, John R. Wygant, and Forrest S. Mozer. Maximizing the Accuracy of Double Probe Electric Field Measurements Near Perigee: The Case of the Van Allen Probes Instruments. *Journal of Geophysical Research (Space Physics)*, 127(1):e30099, January 2022. doi:10.1029/2021JA030099.

[149] D. P. Hartley, C. A. Kletzing, W. S. Kurth, S. R. Bounds, T. F. Averkamp, G. B. Hospodarsky, J. R. Wygant, J. W. Bonnell, O. Santolík, and C. E. J. Watt. Using the cold plasma dispersion relation and whistler mode waves to quantify the antenna

sheath impedance of the Van Allen Probes EFW instrument. *Journal of Geophysical Research (Space Physics)*, 121:4590–4606, May 2016. doi:10.1002/2016JA022501.

[150] D. M. Malaspina, S. G. Claudepierre, K. Takahashi, A. N. Jaynes, S. R. Elkington, R. E. Ergun, J. R. Wygant, G. D. Reeves, and C. A. Kletzing. Kinetic Alfvén waves and particle response associated with a shock-induced, global ULF perturbation of the terrestrial magnetosphere. *Geophysical Research Letters*, 42:9203–9212, November 2015. doi:10.1002/2015GL065935.

[151] W. Li, R. M. Thorne, J. Bortnik, G. D. Reeves, C. A. Kletzing, W. S. Kurth, G. B. Hospodarsky, H. E. Spence, J. B. Blake, J. F. Fennell, S. G. Claudepierre, J. R. Wygant, and S. A. Thaller. An unusual enhancement of low-frequency plasmaspheric hiss in the outer plasmasphere associated with substorm-injected electrons. *Geophysical Review Letters*, 40:3798–3803, August 2013. doi:10.1002/grl.50787.

[152] G. Randall Gladstone, Steven C. Persyn, John S. Eterno, Brandon C. Walther, David C. Slater, Michael W. Davis, Maarten H. Versteeg, Kristian B. Persson, Michael K. Young, Gregory J. Dirks, Anthony O. Sawka, Jessica Tumlinson, Henry Sykes, John Beshears, Cherie L. Rhoad, James P. Cravens, Gregory S. Winters, Robert A. Klar, Walter Lockhart, Benjamin M. Piepgrass, Thomas K. Greathouse, Bradley J. Trantham, Philip M. Wilcox, Matthew W. Jackson, Oswald H. W. Siegmund, John V. Vallerga, Rick Raffanti, Adrian Martin, J. C. Gérard, Denis C. Grodent, Bertrand Bonfond, Benoit Marquet, and François Denis. The Ultraviolet Spectrograph on NASA's Juno Mission. *Space Science Reviews*, 213(1-4):447–473, November 2017. doi:10.1007/s11214-014-0040-z.

[153] S. Alan Stern, David C. Slater, John Scherrer, John Stone, Greg Dirks, Maarten Versteeg, Michael Davis, G. Randall Gladstone, Joel W. Parker, Leslie A. Young, and Oswald H. W. Siegmund. *ALICE: The Ultraviolet Imaging Spectrograph Aboard the New Horizons Pluto–Kuiper Belt Mission*, pages 155–187. Springer New York, New York, NY, 2009. doi:10.1007/978-0-387-89518-5_8.

[154] J. Goldstein, R. A. Wolf, B. R. Sandel, and P. H. Reiff. Electric fields deduced from plasmapause motion in IMAGE EUV images. *Geophysical Research Letters*, 31(1):L01801, January 2004. doi:10.1029/2003GL018797.

[155] R. E. Denton, J. Goldstein, D. H. Lee, R. A. King, Z. C. Dent, D. L. Gallagher, D. Berube, K. Takahashi, M. Nose, D. Milling, and F. Honary. Realistic magnetospheric density model for 29 August 2000. *Journal of Atmospheric and Solar-Terrestrial Physics*, 68(6):615–628, March 2006. doi:10.1016/j.jastp.2005.11.009.

[156] D. L. Gallagher and Mark L. Adrian. Two-dimensional drift velocities from the IMAGE EUV plasmaspheric imager. *Journal of Atmospheric and Solar-Terrestrial Physics*, 69(3):341–350, March 2007. doi:10.1016/j.jastp.2006.05.028.

[157] S. Nakano, M. C. Fok, P. C. Brandt, and T. Higuchi. Estimation of the helium ion density distribution in the plasmasphere based on a single IMAGE/EUV image. *Journal of Geophysical Research (Space Physics)*, 119(5):3724–3740, May 2014. doi:10.1002/2013JA019733.

[158] S. Nakano, M. C. Fok, P. C. Brandt, and T. Higuchi. Estimation of temporal evolution of the helium plasmasphere based on a sequence of IMAGE/EUV images. *Journal of Geophysical Research (Space Physics)*, 119(5):3708–3723, May 2014. doi:10.1002/2013JA019734.

[159] Edmond C. Roelof, Barry H. Mauk, and Robert R. Meier. Instrument requirements for imaging the magnetosphere in extreme ultraviolet and energetic neutral atoms derived from computer-simulated images. In Supriya Chakrabarti, editor, *Instrumentation for Magnetospheric Imagery*, volume 1744 of *Society of Photo-Optical Instrumentation Engineers (SPIE) Conference Series*, pages 19–30, June 1992. doi:10.1117/12.60576.

[160] R. Leitinger, H. P. Ladreiter, and G. Kirchengast. Ionosphere tomography with data from satellite reception of Global Navigation Satellite System signals and ground reception of Navy Navigation Satellite System signals. *Radio Science*, 32(4):1657–1669, July 1997. doi:10.1029/97RS01027.

[161] L. M. Celnikier, C. C. Harvey, R. Jegou, P. Moricet, and M. Kemp. A determination of the electron density fluctuation spectrum in the solar wind, using the ISEE propagation experiment. *Astronomy and Astrophysics*, 126(2):293–298, October 1983.

[162] Y. Jade Morton, Zhe Yang, Brian Breitsch, Harrison Bourne, and Charles Rino. *Ionospheric Effects, Monitoring, and Mitigation Techniques*, chapter 31, pages 879–937. John Wiley and Sons, Ltd, 2020. URL: https://onlinelibrary.wiley.com/doi/abs/10.1002/9781119458449.ch31, arXiv:https://onlinelibrary.wiley.com/doi/pdf/10.1002/9781119458449.ch31, doi:https://doi.org/10.1002/9781119458449.ch31.

[163] Paul A. Bernhardt, R. P. McCoy, K. F. Dymond, J. M. Picone, R. R. Meier, F. Kamalabadi, D. M. Cotton, S. Charkrabarti, T. A. Cook, J. S. Vickers, A. W. Stephan, L. Kersley, S. E. Pryse, I. K. Walker, C. N. Mitchell, P. R. Straus, Helen Na, C. Biswas, G. S. Bust, G. R. Kronschnabl, and T. D. Raymund. Two-dimensional mapping of the plasma density in the upper atmosphere with computerized ionospheric tomography (CIT). *Physics of Plasmas*, 5(5):2010–2021, May 1998. doi:10.1063/1.872872.

[164] R. R. Meier, A. C. Nicholas, J. M. Picone, D. J. Melendez-Alvira, G. I. Ganguli, M. A. Reynolds, and E. C. Roelof. Inversion of plasmaspheric EUV remote sensing data from the STP 72-1 satellite. *Journal of Geophysical Research*, 103(A8):17505–17518, August 1998. doi:10.1029/98JA01175.

[165] V. Angelopoulos, P. Cruce, A. Drozdov, E. W. Grimes, N. Hatzigeorgiu, D. A. King, D. Larson, J. W. Lewis, J. M. McTiernan, and D. A. Roberts. The Space Physics Environment Data Analysis System (SPEDAS). *Space Science Reviews*, 215(1):9, Jan 2019. doi:10.1007/s11214-018-0576-4.

[166] John C. Coxon, Stephen E. Milan, and Brian J. Anderson. A Review of Birkeland Current Research Using AMPERE. In Andreas Keiling, Octav Marghitu, and Michael Wheatland, editors, *Electric Currents in Geospace and Beyond*, volume 235, pages 257–278, March 2018. doi:10.1002/9781119324522.ch16.

[167] Colin L. Waters, B. J. Anderson, D. L. Green, H. Korth, R. J. Barnes, and Heikki Vanhamäki. Science Data Products for AMPERE. In Malcolm Wray Dunlop and Hermann Lühr, editors, *Ionospheric Multi-Spacecraft Analysis Tools: Approaches for Deriving Ionospheric Parameters*, volume 17, page 141. Springer, 2020. doi:10.1007/978-3-030-26732-2_7.

[168] Tim Fuller-Rowell, Eduardo Araujo-Pradere, Cliff Minter, Mihail Codrescu, Paul Spencer, Doug Robertson, and Abram R. Jacobson. Us-tec: A new data assimilation product from the space environment center characterizing the ionospheric total electron content using real-time gps data. *Radio Science*, 41(6), 2006. URL: https://agupubs.onlinelibrary.wiley.com/doi/abs/10.1029/2005RS003393, arXiv:https://agupubs.onlinelibrary.wiley.com/doi/pdf/10.1029/2005RS003393, doi:https://doi.org/10.1029/2005RS003393.

[169] E. A. Araujo-Pradere, T. J. Fuller-Rowell, P. S. J. Spencer, and C. F. Minter. Differential validation of the us-tec model. *Radio Science*, 42(3), 2007. URL: https://agupubs.onlinelibrary.wiley.com/doi/abs/10.1029/2006RS003459, arXiv:https://agupubs.onlinelibrary.wiley.com/doi/pdf/10.1029/2006RS003459, doi:https://doi.org/10.1029/2006RS003459.

[170] D. L. Gallagher, P. D. Craven, and R. H. Comfort. Global core plasma model. *Journal of Geophysical Research*, 105(A8):18,819–18,833, August 2000. doi:10.1029/1999JA000241.

[171] T. P. O'Brien and M. B. Moldwin. Empirical plasmapause models from magnetic indices. *Geophysical Review Letters*, 30:1–1, February 2003. doi:10.1029/2002GL016007.

[172] B. A. Larsen, D. M. Klumpar, and C. Gurgiolo. Correlation between plasmapause position and solar wind parameters. *Journal of Atmospheric and Solar-Terrestrial Physics*, 69(3):334–340, March 2007. doi:10.1016/j.jastp.2006.06.017.

[173] D. Berube, M. B. Moldwin, S. F. Fung, and J. L. Green. A plasmaspheric mass density model and constraints on its heavy ion concentration. *Journal of Geophysical Research (Space Physics)*, 110(A4):A04212, April 2005. doi:10.1029/2004JA010684.

[174] I. Kutiev, K. I. Oyama, T. Abe, and P. Marinov. Plasmasphere electron temperature model based on Akebono data. *Advances in Space Research*, 33(6):975–979, January 2004. doi:10.1016/j.asr.2003.06.011.

[175] J. Bortnik, W. Li, R. M. Thorne, C. Yue, X. Chu, V. Angelopoulos, L. W. Blum, Q. Ma, C. Kletzing, G. D. Reeves, and H. E. Spence. A Neural Network Reconstruction of the Coupled Inner Magnetospheric Environment. In *AGU Fall Meeting Abstracts*, volume 2015, pages SM23D–08, December 2015.

[176] Jacob Bortnik, Xiangning Chu, Qianli Ma, Wen Li, Xiaojia Zhang, Richard M. Thorne, Vassilis Angelopoulos, Richard E. Denton, Craig A. Kletzing, George B. Hospodarsky, Harlan E. Spence, Geoffrey D. Reeves, Shrikanth G. Kanekal, and Daniel N. Baker. Chapter 11 - artificial neural networks for determining magnetospheric conditions. In Enrico Camporeale, Simon Wing, and Jay R. Johnson, editors, *Machine Learning Techniques for Space Weather*, pages 279–300. Elsevier, 2018. URL: https://www.sciencedirect.com/science/article/pii/B9780128117880000111, doi:https://doi.org/10.1016/B978-0-12-811788-0.00011-1.

[177] X. Chu, J. Bortnik, W. Li, Q. Ma, R. Denton, C. Yue, V. Angelopoulos, R. M. Thorne, F. Darrouzet, P. Ozhogin, C. A. Kletzing, Y. Wang, and J. Menietti. A neural network model of three-dimensional dynamic electron density in the inner magnetosphere. *Journal of Geophysical Research (Space Physics)*, 122(9):9183–9197, September 2017. doi:10.1002/2017JA024464.

[178] X. N. Chu, J. Bortnik, W. Li, Q. Ma, V. Angelopoulos, and R. M. Thorne. Erosion and refilling of the plasmasphere during a geomagnetic storm modeled by a neural network. *Journal of Geophysical Research (Space Physics)*, 122(7):7118–7129, July 2017. doi:10.1002/2017JA023948.

[179] Xiangning Chu, Donglai Ma, Jacob Bortnik, W. Kent Tobiska, Alfredo Cruz, S. Dave Bouwer, Hong Zhao, Qianli Ma, Kun Zhang, Daniel N. Baker, Xinlin Li, Harlan Spence, and Geoff Reeves. Relativistic Electron Model in the Outer Radiation Belt Using a Neural Network Approach. *Space Weather*, 19(12):e02808, December 2021. arXiv:2109.10532, doi:10.1029/2021SW002808.

[180] Donglai Ma, Xiangning Chu, Jacob Bortnik, Seth G. Claudepierre, W. Kent Tobiska, Alfredo Cruz, S. Dave Bouwer, J. F. Fennell, and J. B. Blake. Modeling the dynamic variability of sub-relativistic outer radiation belt electron fluxes using machine learning. *arXiv e-prints*, page arXiv:2109.08647, September 2021. arXiv:2109.08647.

[181] Irina S. Zhelavskaya, Yuri Y. Shprits, and Maria Spasojević. Empirical Modeling of the Plasmasphere Dynamics Using Neural Networks. *Journal of Geophysical Research (Space Physics)*, 122(11):11,227–11,244, November 2017. doi:10.1002/2017JA024406.

[182] Ian Goodfellow, Yoshua Bengio, and Aaron Courville. *Deep Learning*. MIT Press, 2016.

[183] Chao Dong, Chen Change Loy, Kaiming He, and Xiaoou Tang. Image super-resolution using deep convolutional networks. *IEEE Transactions on Pattern Analysis and Machine Intelligence*, 38(2):295–307, 2016. doi:10.1109/TPAMI.2015.2439281.

[184] Wenzhe Shi, Jose Caballero, Ferenc Huszár, Johannes Totz, Andrew P. Aitken, Rob Bishop, Daniel Rueckert, and Zehan Wang. Real-time single image and video super-resolution using an efficient sub-pixel convolutional neural network. In *2016 IEEE Conference on Computer Vision and Pattern Recognition (CVPR)*, pages 1874–1883, 2016. doi:10.1109/CVPR.2016.207.

[185] Díaz Baso, C. J. and Asensio Ramos, A. Enhancing sdo/hmi images using deep learning. *Astronomy and Astrophysics*, 614:A5, 2018. doi:10.1051/0004-6361/201731344.

[186] Yin Li, Yueying Ni, Rupert A. C. Croft, Tiziana Di Matteo, Simeon Bird, and Yu Feng. AI-assisted superresolution cosmological simulations. *Proceedings of the National Academy of Science*, 118(19):2022038118, May 2021. arXiv:2010.06608, doi:10.1073/pnas.2022038118.

[187] D. L. Gallagher, M. L. Adrian, and M. W. Liemohn. Origin and evolution of deep plasmaspheric notches. *Journal of Geophysical Research (Space Physics)*, 110(A9):A09201, September 2005. doi:10.1029/2004JA010906.

[188] C. Gurgiolo, B. R. Sandel, J. D. Perez, D. G. Mitchell, C. J. Pollock, and B. A. Larsen. Overlap of the plasmasphere and ring current: Relation to subauroral ionospheric heating. *Journal of Geophysical Research (Space Physics)*, 110(A12):A12217, December 2005. doi:10.1029/2004JA010986.

[189] HE Fei, ZHANG Xiao-Xin, CHEN Bo, and FOK Mei-Ching. Inversion of the earth's plasmaspheric density distribution from euv images with genetic algorithm. *Chinese Journal of Geophysics (in Chinese)*, 55(1):29–35, 2012. URL: http://www.geophy.cn//article/id/cjg_8374, doi:10.6038/j.issn.0001-5733.2012.01.003.

[190] Chunwei Tian, Lunke Fei, Wenxian Zheng, Yong Xu, Wangmeng Zuo, and Chia-Wen Lin. Deep learning on image denoising: An overview, 2020. arXiv:1912.13171.

[191] R. E. Denton, Y. Wang, P. A. Webb, P. M. Tengdin, J. Goldstein, J. A. Redfern, and B. W. Reinisch. Magnetospheric electron density long-term (>1 day) refilling rates inferred from passive radio emissions measured by IMAGE RPI during geomagnetically quiet times. *J. Geophys. Res.*, 117(A3):A03221, March 2012. doi:10.1029/2011JA017274.

[192] Yuki Obana, Naomi Maruyama, Atsuki Shinbori, Kumiko K. Hashimoto, Mariangel Fedrizzi, Masahito Nosé, Yuichi Otsuka, Nozomu Nishitani, Tomoaki Hori, Atsushi Kumamoto, Fuminori Tsuchiya, Shoya Matsuda, Ayako Matsuoka, Yoshiya

Kasahara, Akimasa Yoshikawa, Yoshizumi Miyoshi, and Iku Shinohara. Response of the Ionosphere-Plasmasphere Coupling to the September 2017 Storm: What Erodes the Plasmasphere so Severely? *Space Weather*, 17(6):861–876, June 2019. doi:10.1029/2019SW002168.

[193] Joseph E. Borovsky, Michael Hesse, Joachim Birn, and Maria M. Kuznetsova. What determines the reconnection rate at the dayside magnetosphere? *Journal of Geophysical Research: Space Physics*, 113(A7), 2008. URL: https://agupubs.onlinelibrary.wiley.com/doi/abs/10.1029/2007JA012645, arXiv:https://agupubs.onlinelibrary.wiley.com/doi/pdf/10.1029/2007JA012645, doi:https://doi.org/10.1029/2007JA012645.

[194] V. K. Jordanova, D. T. Welling, S. G. Zaharia, L. Chen, and R. M. Thorne. Modeling ring current ion and electron dynamics and plasma instabilities during a high-speed stream driven storm. *Journal of Geophysical Research (Space Physics)*, 117:A00L08, May 2012. doi:10.1029/2011JA017433.

[195] V. K. Jordanova, Y. Yu, J. T. Niehof, R. M. Skoug, G. D. Reeves, C. A. Kletzing, J. F. Fennell, and H. E. Spence. Simulations of inner magnetosphere dynamics with an expanded RAM-SCB model and comparisons with Van Allen Probes observations. *Geophys. Res. Lett.*, 41(8):2687–2694, April 2014. doi:10.1002/2014GL059533.

[196] Craig E. Rasmussen, Steven M. Guiter, and Steven G. Thomas. A two-dimensional model of the plasmasphere: refilling time constants. *Planetary and Space Science*, 41(1):35–43, January 1993. doi:10.1016/0032-0633(93)90015-T.

[197] C. R. Chappell, M. M. Huddleston, T. E. Moore, B. L. Giles, and D. C. Delcourt. Observations of the warm plasma cloak and an explanation of its formation in the magnetosphere. *Journal of Geophysical Research: Space Physics*, 113(A9), 2008. URL: https://agupubs.onlinelibrary.wiley.com/doi/abs/10.1029/2007JA012945, arXiv:https://agupubs.onlinelibrary.wiley.com/doi/pdf/10.1029/2007JA012945, doi:https://doi.org/10.1029/2007JA012945.

[198] Peter M. Banks. Hydrogen ion velocity distributions in the ionosphere. *Planet. Space Sci.*, 16(6):759–773, June 1968. doi:10.1016/0032-0633(68)90080-9.

[199] P. M. Banks. The thermal structure of the ionosphere. *IEEE Proceedings*, 57:258–281, January 1969.

[200] N. Singh and J. L. Horwitz. Plasmasphere refilling: Recent observations and modeling. *J. Geophys. Res.*, 97:1049, February 1992. doi:10.1029/91JA02602.

[201] J. Goldstein, D. L. Gallagher, B. R. Sandel, M. Davis, P. Molyneux, T. Veach, G. Fletcher, E. Gullikson, D. Windt, D. D. Allred, and R. S. Turley. The Future of Plasmaspheric Extreme Ultraviolet (EUV) Imaging. In *Magnetospheric Imaging*, pages Chapter 6, p 231. Elsevier, 2020. doi:10.1016/B978-0-12-820630-0.00010-6.

[202] D. J. Lawrence, M. F. Thomsen, J. E. Borovsky, R. C. Elphic, and D. J. McComas. Measurements of early and late time plasmaspheric refilling as observed from geosynchronous orbit. *J. Geophys. Res.*, 104:14691, 1999. doi:10.1029/1998JA900087.

[203] J. J. Sojka, C. E. Rasmussen, and R. W. Schunk. An interplanetary magnetic field dependent model of the ionospheric convection electric field. *J. Geophys. Res.*, 91(A10):11281–11290, October 1986. doi:10.1029/JA091iA10p11281.

[204] D. L. Gallagher and R. H. Comfort. Unsolved problems in plasmasphere refilling. *J. Geophys. Res.*, 121:1447, 2016. doi:10.1002/2015JA022279.

[205] Y.-J. Su, M. F. Thomsen, J. E. Borovsky, and J. C. Foster. A linkage between polar patches and plasmaspheric drainage plumes. *Geophys. Res. Lett.*, 28:111, 2001. doi:10.1029/2000GL012042.

[206] Joseph E. Borovsky, Daniel T. Welling, Michelle F. Thomsen, and Michael H. Denton. Long-lived plasmaspheric drainage plumes: Where does the plasma come from? *Journal of Geophysical Research (Space Physics)*, 119(8):6496–6520, August 2014. doi:10.1002/2014JA020228.

[207] M. W. Liemohn, J. U. Kozyra, P. G. Richards, G. V. Khazanov, M. J. Buonsanto, and V. K. Jordanova. Ring current heating of the thermal electrons at solar maximum. *Journal of Geophysical Research*, 105(A12):27767–27776, December 2000. doi:10.1029/2000JA000088.

[208] Nagendra Singh and W. C. Leung. Numerical simulation of filling a magnetic flux tube with a cold plasma: Anomalous plasma effects. *Journal of Geophysical Research*, 100(A3):3585–3600, March 1995. doi:10.1029/94JA02812.

[209] M. Nosé, K. Takahashi, R. R. Anderson, and H. J. Singer. Oxygen torus in the deep inner magnetosphere and its contribution to recurrent process of O^+-rich ring current formation. *J. Geophys. Res.*, 116:A10224, 2011. doi:10.1029/2011JA016651.

[210] M. Nosé, S. Oimatsu, K. Keika, C. A. Kletzing, W. S. Kurth, S. de Pascuale, C. W. Smith, R. J. MacDowall, S. Nakano, G. D. Reeves, H. E. Spence, and B. A. Larsen. Formation of the oxygen torus in the inner magnetosphere: Van Allen Probes observations. *J. Geophys. Res.*, 120:1182, February 2015. doi:10.1002/2014JA020593.

[211] M. Nosé, A. Matsuoka, A. Kumamoto, Y. Kasahara, J. Goldstein, M. Teramoto, F. Tsuchiya, S. Matsuda, M. Shoji, S. Imajo, S. Oimatsu, K. Yamamoto, Y. Obana, R. Nomura, A. Fujimoto, I. Shinohara, Y. Miyoshi, W. Kurth, C. Kletzing, C. Smith, and R. MacDowall. Longitudinal structure of oxygen torus in the inner magnetosphere: Simultaneous observations by Arase and Van Allen Probe A. *Geophys. Res. Lett.*, 45, 2018. doi:10.1002/2018GL080122.

[212] D. L. Carpenter. New Experimental Evidence of the Effect of Magnetic Storms on the Magnetosphere. *Journal of Geophysical Research*, 67(1):135–145, January 1962. doi:10.1029/JZ067i001p00135.

[213] D. L. Carpenter. Earth's plasmasphere awaits rediscovery. *EOS Transactions*, 76(9):89–92, January 1995. doi:10.1029/95EO00041.

[214] P. J. Chi, C. T. Russell, S. Musman, W. K. Peterson, G. Le, V. Angelopoulos, G. D. Reeves, M. B. Moldwin, and F. K. Chun. Plasmaspheric depletion and refilling associated with the September 25, 1998 magnetic storm observed by ground magnetometers at L = 2. *Geophysical Research Letters*, 27(5):633–636, March 2000. doi:10.1029/1999GL010722.

[215] Mark A. Clilverd, Barbara Jenkins, and Neil R. Thomson. Plasmaspheric storm time erosion. *Journal of Geophysical Research: Space Physics*, 105(A6):12997–13008, 2000. URL: https://agupubs.onlinelibrary.wiley.com/doi/abs/10.1029/1999JA900497, arXiv:https://agupubs.onlinelibrary.wiley.com/doi/pdf/10.1029/1999JA900497, doi:https://doi.org/10.1029/1999JA900497.

[216] Chi Wang, Qingmei Zhang, P. J. Chi, and Chuanqi Li. Simultaneous observations of plasmaspheric and ionospheric variations during magnetic storms in 2011: First result from Chinese Meridian Project. *Journal of Geophysical Research (Space Physics)*, 118(1):99–104, January 2013. doi:10.1029/2012JA017967.

[217] Joseph E Borovsky and Michael H Denton. A statistical look at plasmaspheric drainage plumes. *Journal of Geophysical Research: Space Physics*, 113(A9), 2008.

[218] W Li, X-C Shen, Q Ma, L Capannolo, R Shi, RJ Redmon, JV Rodriguez, GD Reeves, CA Kletzing, WS Kurth, et al. Quantification of energetic electron precipitation driven by plume whistler mode waves, plasmaspheric hiss, and exohiss. *Geophysical Research Letters*, 46(7):3615–3624, 2019.

[219] Joseph E Borovsky, Daniel T Welling, Michelle F Thomsen, and Michael H Denton. Long-lived plasmaspheric drainage plumes: Where does the plasma come from? *Journal of Geophysical Research: Space Physics*, 119(8):6496–6520, 2014.

[220] Jonathan Krall, Joseph D Huba, and JE Borovsky. Sami3 simulations of a persistent plasmasphere plume. *Geophysical Research Letters*, 45(8):3374–3381, 2018.

[221] MH Denton and JE Borovsky. Observations and modeling of magnetic flux tube refilling of the plasmasphere at geosynchronous orbit. *Journal of Geophysical Research: Space Physics*, 119(11):9246–9255, 2014.

[222] Masahito Nose, S Oimatsu, K Keika, CA Kletzing, WS Kurth, S De Pascuale, Charles W Smith, RJ MacDowall, S Nakano, GD Reeves, et al. Formation of the oxygen torus in the inner magnetosphere: Van allen probes observations. *Journal of Geophysical Research: Space Physics*, 120(2):1182–1196, 2015.

[223] J-M Jahn, Jerry Goldstein, Geoffrey D Reeves, Philip A Fernandes, Ruth M Skoug, Brian Arthur Larsen, and Harlan E Spence. The warm plasma composition in the inner magnetosphere during 2012–2015. *Journal of Geophysical Research: Space Physics*, 122(11):11–018, 2017.

[224] S Hill, N Buzulukova, S Boardsen, and M-C Fok. Local heating of oxygen ions in the presence of magnetosonic waves: Possible source for the warm plasma cloak? *Journal of Geophysical Research: Space Physics*, 125(8):e2019JA027210, 2020.

[225] JC Foster, PJ Erickson, AJ Coster, S Thaller, J Tao, John R Wygant, and JW Bonnell. Storm time observations of plasmasphere erosion flux in the magnetosphere and ionosphere. *Geophysical Research Letters*, 41(3):762–768, 2014.

[226] S De Pascuale, VK Jordanova, J Goldstein, CA Kletzing, WS Kurth, SA Thaller, and JR Wygant. Simulations of van allen probes plasmaspheric electron density observations. *Journal of Geophysical Research: Space Physics*, 123(11):9453–9475, 2018.

[227] JC Foster and HB Vo. Average characteristics and activity dependence of the subauroral polarization stream. *Journal of Geophysical Research: Space Physics*, 107(A12):SIA–16, 2002.

[228] Michael G Henderson, Eric F Donovan, John C Foster, Ian R Mann, Thomas J Immel, Stephen B Mende, and John B Sigwarth. Start-to-end global imaging of a sunward propagating, saps-associated giant undulation event. *Journal of Geophysical Research: Space Physics*, 115(A4), 2010.

[229] Michael G Henderson, SK Morley, and LE Kepko. Saps-associated explosive brightening on the duskside: A new type of onset-like disturbance. *Journal of Geophysical Research: Space Physics*, 123(1):197–210, 2018.

[230] B. S. R. Kunduri, J. B. H. Baker, J. M. Ruohoniemi, N. Nishitani, K. Oksavik, P. J. Erickson, A. J. Coster, S. G. Shepherd, W. A. Bristow, and E. S. Miller. A New Empirical Model of the Subauroral Polarization Stream. *Journal of Geophysical Research (Space Physics)*, 123(9):7342–7357, September 2018. doi:10.1029/2018JA025690.

[231] David A. Galvan, Mark B. Moldwin, Bill R. Sandel, and Geoff Crowley. On the causes of plasmaspheric rotation variability: IMAGE EUV observations. *Journal of Geophysical Research (Space Physics)*, 115(A1):A01214, January 2010. doi:10.1029/2009JA014321.

[232] K. Takahashi, R. E. Denton, W. Kurth, C. Kletzing, J. Wygant, J. Bonnell, L. Dai, K. Min, C. W. Smith, and R. MacDowall. Externally driven plasmaspheric ULF waves observed by the Van Allen Probes. *Journal of Geophysical Research (Space Physics)*, 120:526–552, January 2015. doi:10.1002/2014JA020373.

[233] J. W. Dungey. Electrodynamics of the Outer Atmosphere. In *Physics of the Ionosphere*, page 229, January 1955.

[234] Dong-Hun Lee and Robert L. Lysak. Magnetospheric ULF wave coupling in the dipole model: the impulsive excitation. *Journal of Geophysical Research*, 94(A12):17097–17103, December 1989. doi:10.1029/JA094iA12p17097.

[235] John C. Samson and Gordon Rostoker. Latitude-dependent characteristics of high-latitude Pc 4 and Pc 5 micropulsations. *Journal of Geophysical Research*, 77(31):6133–6144, November 1972. doi:10.1029/JA077i031p06133.

[236] M. G. Kivelson and D. J. Southwood. Resonant ULF waves: A new interpretation. *Geophysical Research Letters*, 12(1):49–52, January 1985. doi:10.1029/GL012i001p00049.

[237] J. C. Samson, B. G. Harrold, J. M. Ruohoniemi, R. A. Greenwald, and A. D. M. Walker. Field line resonances associated with MHD waveguides in the magnetosphere. *Geophysical Research Letters*, 19(5):441–444, March 1992. doi:10.1029/92GL00116.

[238] S. G. Claudepierre, F. R. Toffoletto, and M. Wiltberger. Global MHD modeling of resonant ULF waves: Simulations with and without a plasmasphere. *Journal of Geophysical Research (Space Physics)*, 121(1):227–244, January 2016. doi:10.1002/2015JA022048.

[239] D. L. Carpenter and R. R. Anderson. An ISEE/Whistler model of equatorial electron density in the magnetosphere. *Journal of Geophysical Research (Space Physics)*, 97:1097–1108, February 1992. doi:10.1029/91JA01548.

[240] A. W. Degeling, I. J. Rae, C. E. J. Watt, Q. Q. Shi, R. Rankin, and Q. G. Zong. Control of ULF Wave Accessibility to the Inner Magnetosphere by the Convection of Plasma Density. *Journal of Geophysical Research (Space Physics)*, 123(2):1086–1099, February 2018. doi:10.1002/2017JA024874.

[241] Jie Ren, Q. G. Zong, Y. Miyoshi, R. Rankin, H. E. Spence, H. O. Funsten, J. R. Wygant, and C. A. Kletzing. A Comparative Study of ULF Waves' Role in the Dynamics of Charged Particles in the Plasmasphere: Van Allen Probes Observation. *Journal of Geophysical Research (Space Physics)*, 123(7):5334–5343, July 2018. doi:10.1029/2018JA025255.

[242] J. K. Sandhu, I. J. Rae, F. A. Staples, D. P. Hartley, M. T. Walach, T. Elsden, and K. R. Murphy. The Roles of the Magnetopause and Plasmapause in Storm-Time ULF Wave Power Enhancements. *Journal of Geophysical Research (Space Physics)*, 126(7):e29337, July 2021. doi:10.1029/2021JA029337.

[243] Matina Gkioulidou, A. Y. Ukhorskiy, D. G. Mitchell, T. Sotirelis, B. H. Mauk, and L. J. Lanzerotti. The role of small-scale ion injections in the buildup of Earth's ring current pressure: Van Allen Probes observations of the 17 March 2013 storm. *Journal of Geophysical Research (Space Physics)*, 119(9):7327–7342, September 2014. doi:10.1002/2014JA020096.

[244] S. Ohtani, H. J. Singer, and T. Mukai. Effects of the fast plasma sheet flow on the geosynchronous magnetic configuration: Geotail and GOES coordinated study. *Journal of Geophysical Research (Space Physics)*, 111(A1):A01204, January 2006. doi:10.1029/2005JA011383.

[245] M. I. Sitnov, M. Swisdak, and A. V. Divin. Dipolarization fronts as a signature of transient reconnection in the magnetotail. *Journal of Geophysical Research (Space Physics)*, 114(A4):A04202, April 2009. doi:10.1029/2008JA013980.

[246] J. E. Stawarz, S. Eriksson, F. D. Wilder, R. E. Ergun, S. J. Schwartz, A. Pouquet, J. L. Burch, B. L. Giles, Y. Khotyaintsev, O. Le Contel, P. A. Lindqvist, W. Magnes, C. J. Pollock, C. T. Russell, R. J. Strangeway, R. B. Torbert, L. A. Avanov, J. C. Dorelli, J. P. Eastwood, D. J. Gershman, K. A. Goodrich, D. M. Malaspina, G. T. Marklund, L. Mirioni, and A. P. Sturner. Observations of turbulence in a Kelvin-Helmholtz event on 8 September 2015 by the Magnetospheric Multiscale mission. *Journal of Geophysical Research (Space Physics)*, 121(11):11,021–11,034, November 2016. doi:10.1002/2016JA023458.

[247] R. E. Ergun, K. A. Goodrich, J. E. Stawarz, L. Andersson, and V. Angelopoulos. Large-amplitude electric fields associated with bursty bulk flow braking in the Earth's plasma sheet. *Journal of Geophysical Research (Space Physics)*, 120(3):1832–1844, March 2015. doi:10.1002/2014JA020165.

[248] T. Takada, R. Nakamura, W. Baumjohann, Y. Asano, M. Volwerk, T. L. Zhang, B. Klecker, H. Rème, E. A. Lucek, and C. Carr. Do BBFs contribute to inner magnetosphere dipolarizations: Concurrent Cluster and Double Star observations. *Geophysical Research Letters*, 33(21):L21109, November 2006. doi:10.1029/2006GL027440.

[249] S. Dubyagin, V. Sergeev, S. Apatenkov, V. Angelopoulos, A. Runov, R. Nakamura, W. Baumjohann, J. McFadden, and D. Larson. Can flow bursts penetrate into the inner magnetosphere? *Geophysical Research Letters*, 38(8):L08102, April 2011. doi:10.1029/2011GL047016.

[250] J. Birn, M. F. Thomsen, J. E. Borovsky, G. D. Reeves, D. J. McComas, and R. D. Belian. Characteristic plasma properties during dispersionless substorm injections at geosynchronous orbit. *Journal of Geophysical Reserach*, 102:2309–2324, February 1997. doi:10.1029/96JA02870.

[251] Ashar F. Ali, David M. Malaspina, Scot R. Elkington, Allison N. Jaynes, Anthony A. Chan, John Wygant, and Craig A. Kletzing. Electric and magnetic radial diffusion coefficients using the Van Allen probes data. *Journal of Geophysical Research (Space Physics)*, 121(10):9586–9607, October 2016. doi:10.1002/2016JA023002.

[252] A. W. Breneman, A. Halford, R. Millan, M. McCarthy, J. Fennell, J. Sample, L. Woodger, G. Hospodarsky, J. R. Wygant, C. A. Cattell, J. Goldstein, D. Malaspina, and C. A. Kletzing. Global-scale coherence modulation of radiation-belt electron loss from plasmaspheric hiss. *Nature*, 523:193–195, July 2015. doi:10.1038/nature14515.

[253] J.-F. Ripoll, J. M. Albert, and G. S. Cunningham. Electron lifetimes from narrowband wave-particle interactions within the plasmasphere. *Journal of Geophysical Research (Space Physics)*, 119:8858–8880, November 2014. doi:10.1002/2014JA020217.

[254] M. Sandanger, F. Søraas, K. Aarsnes, K. Oksavik, and D. S. Evans. Loss of relativistic electrons: Evidence for pitch angle scattering by electromagnetic ion cyclotron waves excited by unstable ring current protons. *Journal of Geophysical Research (Space Physics)*, 112(A12):A12213, December 2007. doi:10.1029/2006JA012138.

[255] M. E. Usanova, A. Drozdov, K. Orlova, I. R. Mann, Y. Shprits, M. T. Robertson, D. L. Turner, D. K. Milling, A. Kale, D. N. Baker, S. A. Thaller, G. D. Reeves, H. E. Spence, C. Kletzing, and J. Wygant. Effect of EMIC waves on relativistic and ultrarelativistic electron populations: Ground-based and Van Allen Probes observations. *Geophys. Res. Lett.*, 41(5):1375–1381, March 2014. doi:10.1002/2013GL059024.

[256] Yuri Y. Shprits, Alexander Y. Drozdov, Maria Spasojevic, Adam C. Kellerman, Maria E. Usanova, Mark J. Engebretson, Oleksiy V. Agapitov, Irina S. Zhelavskaya, Tero J. Raita, Harlan E. Spence, Daniel N. Baker, Hui Zhu, and Nikita A. Aseev. Wave-induced loss of ultra-relativistic electrons in the Van Allen radiation belts. *Nature Communications*, 7:12883, September 2016. doi:10.1038/ncomms12883.

[257] Dwight R. Nicholson. *Introduction to Plasma Theory*. John Wiley and Sons, New York, 1983.

[258] O. Agapitov, D. Mourenas, A. Artemyev, G. Hospodarsky, and J. W. Bonnell. Time Scales for Electron Quasi-linear Diffusion by Lower-Band Chorus Waves: The Effects of ω_{pe}/Ω_{ce} Dependence on Geomagnetic Activity. *Geophysical Research Letters*, 46(12):6178–6187, June 2019. doi:10.1029/2019GL083446.

[259] D. M. Malaspina, J.-F. Ripoll, X. Chu, G. Hospodarsky, and J. Wygant. Variation in Plasmaspheric Hiss Wave Power With Plasma Density. *Geophysical Research Letters*, 45:9417–9426, September 2018. doi:10.1029/2018GL078564.

[260] D. N. Baker, S. G. Kanekal, V. C. Hoxie, S. Batiste, M. Bolton, X. Li, S. R. Elkington, S. Monk, R. Reukauf, S. Steg, J. Westfall, C. Belting, B. Bolton, D. Braun, B. Cervelli, K. Hubbell, M. Kien, S. Knappmiller, S. Wade, B. Lamprecht, K. Stevens, J. Wallace, A. Yehle, H. E. Spence, and R. Friedel. The Relativistic Electron-Proton Telescope (REPT) Instrument on Board the Radiation Belt Storm Probes (RBSP) Spacecraft: Characterization of Earth's Radiation Belt High-Energy Particle Populations. *Space Science Reviews*, 179:337–381, November 2013. doi:10.1007/s11214-012-9950-9.

[261] Jun Liang, E. Donovan, A. Reimer, D. Hampton, S. Zou, and R. Varney. Ionospheric electron heating associated with pulsating auroras: Joint optical and pfisr observations. *Journal of Geophysical Research: Space Physics*, 123(5):4430–4456, 2018. URL: https://agupubs.onlinelibrary.wiley.com/doi/abs/10.1029/2017JA025138, arXiv:https://agupubs.onlinelibrary.wiley.com/doi/pdf/10.1029/2017JA025138, doi:https://doi.org/10.1029/2017JA025138.

[262] V. K. Jordanova, C. J. Farrugia, R. M. Thorne, G. V. Khazanov, G. D. Reeves, and M. F. Thomsen. Modeling ring current proton precipitation by electromagnetic ion

cyclotron waves during the May 14-16, 1997, storm. *Journal of Geophysical Research*, 106(A1):7–22, January 2001. doi:10.1029/2000JA002008.

[263] Lunjin Chen, Richard M. Thorne, Vania K. Jordanova, Chih-Ping Wang, Matina Gkioulidou, Larry Lyons, and Richard B. Horne. Global simulation of EMIC wave excitation during the 21 April 2001 storm from coupled RCM-RAM-HOTRAY modeling. *Journal of Geophysical Research (Space Physics)*, 115(A7):A07209, July 2010. doi:10.1029/2009JA015075.

[264] V. K. Jordanova, M. Spasojevic, and M. F. Thomsen. Modeling the electromagnetic ion cyclotron wave-induced formation of detached subauroral proton arcs. *Journal of Geophysical Research (Space Physics)*, 112(A8):A08209, August 2007. doi:10.1029/2006JA012215.

[265] M. E. Usanova, F. Darrouzet, I. R. Mann, and J. Bortnik. Statistical analysis of EMIC waves in plasmaspheric plumes from Cluster observations. *Journal of Geophysical Research (Space Physics)*, 118(8):4946–4951, August 2013. doi:10.1002/jgra.50464.

[266] D. Sinclair and J. Dyer. Radiation effects and COTS parts in SmallSats. In *27th Annual AIAA/USU Conference on Small Satellites*, 2013.

[267] Regina Soufli, Russell M. Hudyma, Eberhard Spiller, Eric M. Gullikson, Mark A. Schmidt, Jeff C. Robinson, Sherry L. Baker, Christopher C. Walton, and John S. Taylor. Sub-diffraction-limited multilayer coatings for the 0.3 numerical aperture micro-exposure tool for extreme ultraviolet lithography. *Applied Optics*, 46(18):3736–3746, June 2007. doi:10.1364/AO.46.003736.

[268] Regina Soufli, David L. Windt, Jeff C. Robinson, Sherry L. Baker, Eberhard Spiller, Franklin J. Dollar, Andrew L. Aquila, Eric M. Gullikson, Benjawan Kjornrattanawanich, John F. Seely, and Leon Golub. Development and testing of EUV multilayer coatings for the atmospheric imaging assembly instrument aboard the Solar Dynamics Observatory. In Silvano Fineschi and Rodney A. Viereck, editors, *Solar Physics and Space Weather Instrumentation*, volume 5901 of *Society of Photo-Optical Instrumentation Engineers (SPIE) Conference Series*, pages 173–183, August 2005. doi:10.1117/12.617370.

[269] Regina Soufli, Sherry L. Baker, David L. Windt, Eric M. Gullikson, Jeff C. Robinson, William A. Podgorski, and Leon Golub. Atomic force microscopy characterization of Zerodur mirror substrates for the extreme ultraviolet telescopes aboard NASA's Solar Dynamics Observatory. *Applied Optics*, 46(16):3156–3163, June 2007. doi:10.1364/AO.46.003156.

[270] Regina Soufli, Mónica Fernández-Perea, Sherry L. Baker, Jeff C. Robinson, Jennifer Alameda, and Christopher C. Walton. Spontaneously intermixed Al-Mg barriers enable corrosion-resistant Mg/SiC multilayer coatings. *Applied Physics Letters*, 101(4):043111, July 2012. doi:10.1063/1.4737649.

[271] Paul Boerner, Christopher Edwards, James Lemen, Adam Rausch, Carolus Schrijver, Richard Shine, Lawrence Shing, Robert Stern, Theodore Tarbell, Alan Title, C. Jacob Wolfson, Regina Soufli, Eberhard Spiller, Eric Gullikson, David McKenzie, David Windt, Leon Golub, William Podgorski, Paola Testa, and Mark Weber. Initial Calibration of the Atmospheric Imaging Assembly (AIA) on the Solar Dynamics Observatory (SDO). *Solar Physics*, 275(1-2):41–66, January 2012. doi:10.1007/s11207-011-9804-8.

[272] James R. Lemen, Alan M. Title, David J. Akin, Paul F. Boerner, Catherine Chou, Jerry F. Drake, Dexter W. Duncan, Christopher G. Edwards, Frank M. Friedlaender, Gary F. Heyman, Neal E. Hurlburt, Noah L. Katz, Gary D. Kushner, Michael Levay, Russell W. Lindgren, Dnyanesh P. Mathur, Edward L. McFeaters, Sarah Mitchell, Roger A. Rehse, Carolus J. Schrijver, Larry A. Springer, Robert A. Stern, Theodore D. Tarbell, Jean-Pierre Wuelser, C. Jacob Wolfson, Carl Yanari, Jay A. Bookbinder, Peter N. Cheimets, David Caldwell, Edward E. Deluca, Richard Gates, Leon Golub, Sang Park, William A. Podgorski, Rock I. Bush, Philip H. Scherrer, Mark A. Gummin, Peter Smith, Gary Auker, Paul Jerram, Peter Pool, Regina Soufli, David L. Windt, Sarah Beardsley, Matthew Clapp, James Lang, and Nicholas Waltham. The Atmospheric Imaging Assembly (AIA) on the Solar Dynamics Observatory (SDO). *Solar Physics*, 275(1-2):17–40, January 2012. doi:10.1007/s11207-011-9776-8.

[273] Dennis Martínez-Galarce, Regina Soufli, David L. Windt, Marilyn Bruner, Eric Gullikson, Shayna Khatri, Eberhard Spiller, Jeff C. Robinson, Sherry Baker, and Evan Prast. Multisegmented, multilayer-coated mirrors for the Solar Ultraviolet Imager. *Optical Engineering*, 52:095102, September 2013. doi:10.1117/1.OE.52.9.095102.